Department of Precision and Microsystems Engineering

Design and experimental validation of low stiffness aerostatic thrust bearings

R.P. Hoogeboom

Report no : MSD 2016.021
Coach : Dr.ir. R.A.J. van Ostayen
Professor : Prof.dr.ir. J.L. Herder
Specialisation : Mechatronic System Design
Type of report : Master Thesis
Date : 27-06-2016

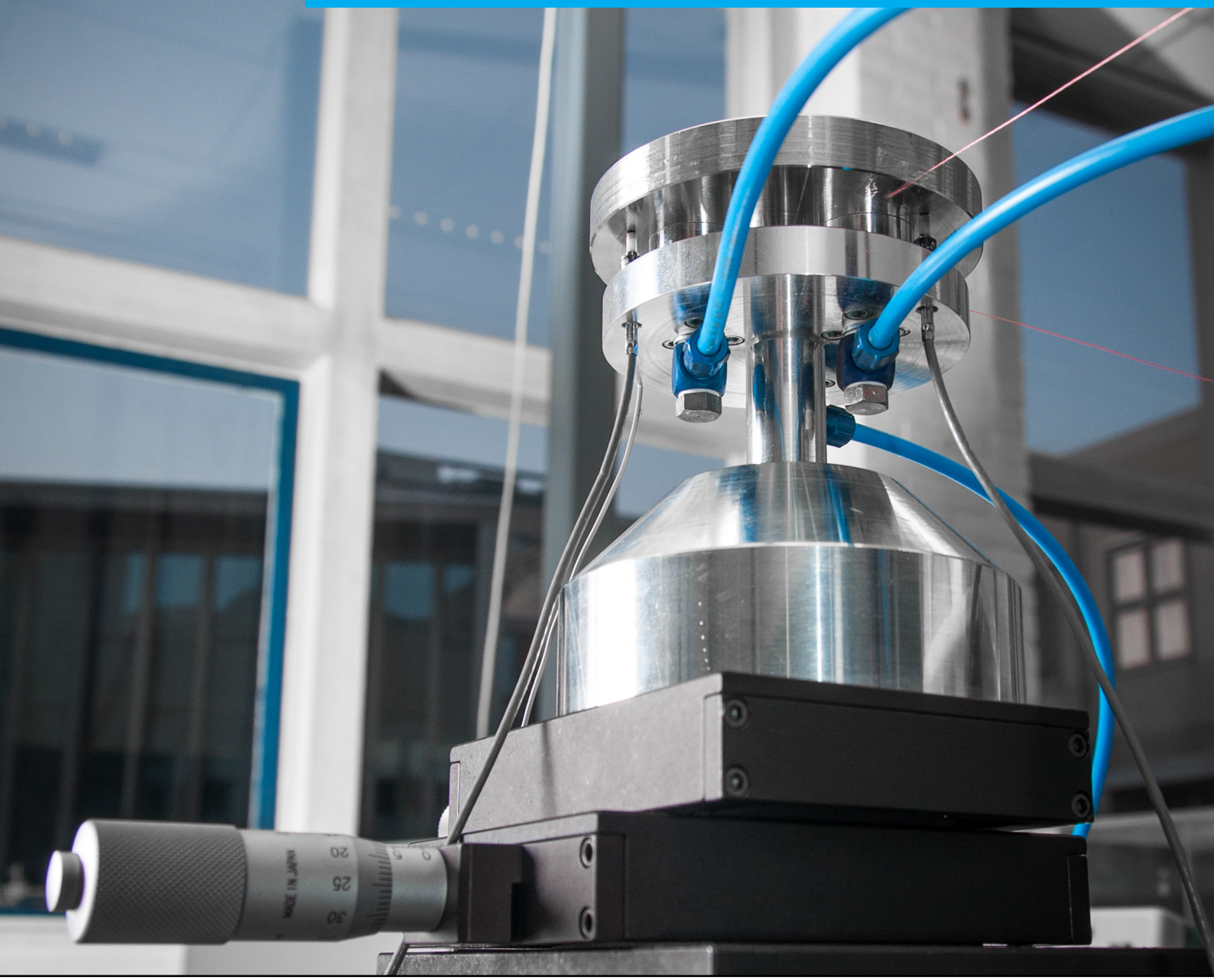

TU Delft Delft University of Technology

Challenge the future

Design and experimental validation of low stiffness aerostatic thrust bearings

by

R.P. Hoogeboom

in partial fulfillment of the requirements for the degree of

Master of Science

in Mechanical Engineering

at the Delft University of Technology,

to be defended publicly on June 27, 2016

Student number:	1369490	
Supervisor:	Dr.ir. R.A.J. van Ostayen,	TU Delft
Thesis committee:	Prof.dr.ir. J.L. Herder,	TU Delft
	Dr.ir. M. Tichem,	TU Delft
	Dr.ir. D.H. Plettenburg,	TU Delft

TU Delft Delft University of Technology

Abstract

Linear aerostatic bearings are frequently used in high precision stages for their advantageous bearing properties, with low friction and absence of stick-slip being most notable. To improve relatively low out-of-plane stiffness of air bearings, pre-loading is applied. A common method of pre-loading is by utilizing vacuum, where a constant vacuum force decreases film height resulting in increased stiffness. Other methods for increasing stiffness are available, which is an active field of research.

However, high stiffness results in strong coupling between bearing and running surface, transferring unwanted external vibrations. The amount of vibration transfer is quantified as transmissibility, which is the ratio of displacements between coupled surfaces. This property is frequency dependent. To reduce disturbance from external vibrations, this research focusses on reducing air bearing stiffness by combining pressurized and vacuum bearing pads, which to the knowledge of the author has not yet been researched.

To analyse stiffness behaviour, air bearings have been modelled based on Reynolds equation. The effect of a vibrating running surface is modelled by linear perturbation of Reynolds equation. Resulting equations have been solved with a self developed finite volume method code, resulting in air film stiffness and damping as a function of frequency in an computationally efficient manner.

Two combinations of thrust and vacuum bearings with a stable low stiffness operating point have been designed with the developed models. By offsetting vacuum and thrust surfaces or by using a micrometer pocket in the thrust bearing surface, vacuum and thrust stiffness cancel out, creating a range of low stiffness between regions with higher stiffness.

To validate the models, air bearings have been manufactured. Measurements on restrictor properties have shown the literature model to be invalid for realistic pressure drops. Without taking the measured restrictor behaviour into account, model and measurement will not match.

Also shown is that controlling surfaces flatness is essential for predictable bearing behaviour. Performance of available production methods is thoroughly researched. Model and measurement correspondence can only be achieved by taking surface properties into account.

Also, the low tip-tilt stiffness of a single air bearing has been found to negatively effect measurements on film height. By using three bearings in the measurement set-up, tip-tilt stiffness has been significantly increased. This reduces measurement uncertainty.

By taking these findings into account, excellent agreement between measurements and model has been achieved. This clears the way for development of a low stiffness prototype, combining thrust and vacuum bearings. Ideas on model improvement and prototype development are shared in the recommendations.

Preface and acknowledgements

This report is the result of my thesis study, which is the final stage of my master Mechanical Engineering, track Precision and Microsystems engineering at the Delft University of Technology. After following courses on mechatronics and dynamics, I decided to take on a research project on the subject of air bearings. This work covers modelling and optimization, to which I am familiar after following courses, but also more practical parts such as design, manufacturing and testing. These were subjects that I wanted to improve my knowledge on before finishing my study. This combination of theoretical and practical work made for an interesting final project.

I would like to thank Ron for his coaching and technical guidance during my research. From patiently explaining mathematics, discussing design concepts or even checking code to interpreting strange measurement results, you have been of great help during all aspects of this research. Although, looking back at it, we may sometimes amplify each other's curiosity and drive to get to the bottom of all interesting phenomena encountered, leading to a somewhat longer graduation project than average, I am proud of the result and thankful for our cooperation.

Also, I would like to thank the guys at the faculty workshop for patiently helping me with manufacturing. Simon and Hans never have gotten tired of me asking and have taught me a lot on practical matters. Furthermore, I cannot thank Reinier enough for his help in consulting me on manufacturing, checking designs and drawings, explaining techniques and of course our Friday afternoon project of lathing a micrometer pocket, against better judgement.

Finally, I would like to thank my family, friends and fellow students for their support and helping me put things in perspective.

Ruud Hoogeboom
Delft, June 2016

Table of Contents

1

Introduction

In 1886, Osborne Reynolds submitted a paper to the Royal Society of London with the title: "On the Theory of Lubrication and Its Application to *Mr. Beauchamp Tower's* Experiments, Including an Experimental Determination of the Viscosity of Olive Oil" [1]. Mr. Beauchamp Tower, a railway engineer, was measuring friction in journal bearings trying to find 'any regularity' under ordinary lubrication conditions. Somewhat by chance he included the unusual circumstances of completely immersing surfaces in oil. While looking at the experimental results, Reynolds realised that the surfaces might be completely and continuously separated by a film of oil, in which case the results would be deducible from the equations of hydrodynamics.

In his paper, Reynolds develops an equation which will later become known as Reynolds equation, describing the pressure distribution of thin viscous fluid films and laying the foundation for the study of full film lubrication.

1-1 Research context

Reynolds' discovery has lead to a wide range of full film lubricated bearings, with an equally wide range of applications. Full film lubricated bearings can for example be found in extreme high speed turbochargers [2], machining equipment [3], hard disk drives [4], dental equipment [5] and high precision stages [6], [7], [8]. This last example will be the focus of this study.

Full film bearings can be characterized on different criteria. Considering guidance type, bearings can provide linear, cylindrical or spherical guidance. A second distinction is lubricant phase, which can either be liquid or gas. Commonly used liquids are oil or water. Bearings using liquid lubricant are noted with the prefix hydro-. Gas lubricated bearings mostly use air, resulting in the prefix aero-, but other gasses are used for specific applications. A final distinction is the method of pressure generation. Pressure is either generated by relative movement of bearing surfaces, with suffix -dynamic, or is inserted externally, with suffix -static.

This study focuses on linear aerostatic bearings with high precision stages as application. Air bearings have distinct advantages over alternative bearing concepts, extreme low friction and absence of stick-slip being among the most important. Stick-slip limits achievable position resolution of motion stages [9]. By eliminating stick-slip, higher resolutions can be achieved.

Extremely low friction between surfaces allows for high speeds and accelerations, also very beneficial for motion stages. Since operation is contact-free, air bearings do hardly wear and have long life spans if operated correctly. In contrast to oil, air is a clean lubricant and does not need seals [10].

A disadvantage of air bearings is the high geometrical accuracies required on both bearing and running surface. Furthermore, they require constant power in the form of clean, pressurized air which increases operating costs. Without air, contact occurs which may damage bearing or running surface. Also, aerostatic bearings can be sensitive to a dynamic instability known as pneumatic hammer, depending on the design.

Another disadvantage is the relative low stiffness of air bearings compared to rolling-element or hydrostatic bearings. Stiffness can significantly be increased by pre-loading the bearing. Well known methods for applying pre-load are adding mass, using magnets, using vacuum or by mounting two air bearings on opposite sides. Vacuum pre-loading is commonly used because it is a compact solution, does not add significant extra mass, and requires only one running surface. In vacuum pre-loading, a constant pulling force between bearing and running surface is created by enclosing a vacuum chamber inside of the pressurized part, sealing in the vacuum. This results in decreased fly height and increased stiffness [11].

Other methods are available for increasing bearing stiffness, which is an active field of research. These methods include using convergent gap geometry [12], adding X-shaped grooves [13], passive gap shape variation using membranes [14], active gap variation using a PZT actuator [15] and active restrictor compensation using a variety of actuators [16], [17], [18].

These studies have in common that they optimize for high stiffness, resulting in a strong coupling between running surface and bearing. The amount of movement transfer caused by this coupling is called transmissibility and is frequency dependent.

In high precision applications, isolation from environmental vibrations is critical for assuring adequate performance [19]. High stiffness connections have high transmissibility, resulting in a significant transfer of environmental vibrations. Low stiffness connections can be used to decrease transmissibility. Design of low stiffness bearings will be the focus of this research.

As shown, air bearings have beneficial properties for precision stages and are often optimised for high stiffness. However, no research into reducing air bearing stiffness has been found. This could provide an interesting opportunity in integrating vibration isolation in a bearing system. Therefore this research focusses on the design and development of low stiffness air bearings, by combining pressurized bearings with vacuum bearings. This should allow the combination of beneficial properties of linear aerostatic bearings in two in-plane directions with vibration isolating properties in the out-of-plane direction.

1-2 Research goals

The goal of this research is to design a combination of pressurized and vacuum bearings that have a stable, low stiffness behaviour with vibration isolation as application. Because vibration isolation is a dynamic property, the dynamics of a vibrating thin film are included into the study. To bridge the gap between reality and theory, a design is to be realised for validation of theory.

1-3 Project outline

This thesis starts with a short chapter on Reynolds equation. To determine this equation's use and limits, assumptions will be stated and Reynolds equation will be derived. This will be used to develop models on the static behaviour of aerostatic bearings and gain insight into the working principle of air bearings in a following chapter. Next, linear perturbation techniques will be applied to Reynolds equation to find dynamic thin film stiffness and damping. The resulting equations will be solved with the finite volume method.

Both static and dynamic models will be used to find multiple low stiffness designs. To validate theory and gain insight in realisation of the designs, a test set-up will be built for static and dynamic validation.

1-4 Reader's manual

This thesis is written to be comprehensible for a MSc student in precision engineering, without prior knowledge on Reynolds equation or air bearings, to allow successors to continue with this research. Knowledgeable readers might therefore find the pace of the first chapters slow. Each chapter starts and concludes with a summary, which should suffice for chapter 2 to chapter 4. Knowledgeable readers should start reading in detail at chapter 5 and further.

2

Reynolds equation

The motion of viscous fluid can be described by the Navier-Stokes equations. These equations include terms dependent on inertia, body forces, pressures and viscous forces. Solving these equations including all terms is complex. Because in some cases terms have negligible magnitude compared to others, they can be dropped, allowing Navier-Stokes equations to be simplified.

In lubrication theory, a significant disparity in length scale is assumed. This theory describes the flow of fluids in a geometry in which one dimension is significantly smaller than others. This type of flow is therefore called thin film flow. The pressure distribution in thin film flow is governed by Reynolds equation.

In this chapter, assumptions made to derive Reynolds equation are discussed. The full derivation of Reynolds equation can be found in Appendix A. The resulting partial differential equation and the physical interpretation of terms are treated in this chapter.

2-1 Derivation of the Reynolds equation

There are multiple ways to derive Reynolds equation. Two common derivations are from simplification of the Navier-Stokes equation, or by looking at a small fluid element in equilibrium. In this section the latter options is chosen. First, the assumptions needed for the derivation will be briefly discussed in subsection 2-1-1. The equilibrium of pressure and shear stress and a mass balance can be found in Appendix A. The resulting equation and the physical interpretation will be discussed.

2-1-1 Assumptions for derivation of Reynolds equation

To attain a mathematically solvable equation, some simplifying assumptions have been made. These assumptions are chosen such that the equation becomes easier to solve while the accuracy of the physics that the equation tries to capture does not suffer. Some assumptions are done at a specific point in the derivation in the appendix and will be referenced there. Others are of a more general nature, and will not be referenced at a specific equation. Equations applied in this section are derived from [20], [21] and [10]. The assumptions are the following:

1. Body forces, which act on the whole system, are neglected. Body forces include gravity, inertial accelerations or electric field accelerations.

2. Constant pressure is assumed throughout the film height. Since, for thin film flow, film height is significantly smaller than film length, difference of pressure in film height is neglected.

3. No slip at the boundaries is assumed. Fluid and surface have the same velocity at the interface.

4. The lubricant behaves like a Newtonian fluid. Shear stress is linear proportional with the velocity derivative scaled with viscosity: $\tau = \eta \frac{du}{dy}$. Air and most lubrication oils behave like a Newtonian fluid.

5. Laminar flow is assumed.

6. Fluid inertia is neglected. This assumption can be tested with Reynolds number. This is discussed in subsection 4-2-5.

7. The film is assumed to be isothermal.

8. Lubricant viscosity is considered constant. In literature, this is called the isoviscous approximation. For oils, viscosity is highly dependent on temperature, but for gasses this effect is smaller. Since the previous assumption states isothermal operation, this temperature dependency is neglected. Pressure increase will also have negligible effect on viscosity.

2-1-2 Reynolds equation

Taking all assumptions into account, Reynolds equation can be derived. This is described in Appendix A. The resulting equation can be written as:

$$\begin{aligned} \frac{\partial}{\partial x}\left(\frac{\rho\, h^3}{12\,\eta}\frac{\partial p}{\partial x}\right) + \frac{\partial}{\partial y}\left(\frac{\rho\, h^3}{12\,\eta}\frac{\partial p}{\partial y}\right) - \frac{\partial}{\partial x}\left(\frac{\rho\, h\,(u_1+u_2)}{2}\right) - \frac{\partial}{\partial y}\left(\frac{\rho\, h\,(v_1+v_2)}{2}\right) \\ = \rho\,(w_2 - w_1) - \rho\, u_2 \frac{\partial h}{\partial x} - \rho\, v_2 \frac{\partial h}{\partial y} + h\,\frac{\partial p}{\partial t} \end{aligned} \tag{2-1}$$

where ρ is lubricant density, h is film height, p is film pressure, η is lubricant viscosity, t is time and u, v and w are velocities in x, y and z direction, as drawn in Figure 2-1.

2-1-3 Physical interpretation of terms in Reynolds equation

To understand how pressure can be build up in a thin film, and thus be able to carry load, different terms and their physical interpretation in the Reynolds equation are explored in this section. Reynolds equation, as derived in Equation 2-1, can be simplified by considering a one dimensional system, neglecting side flow. Time dependent terms, on the right hand side of

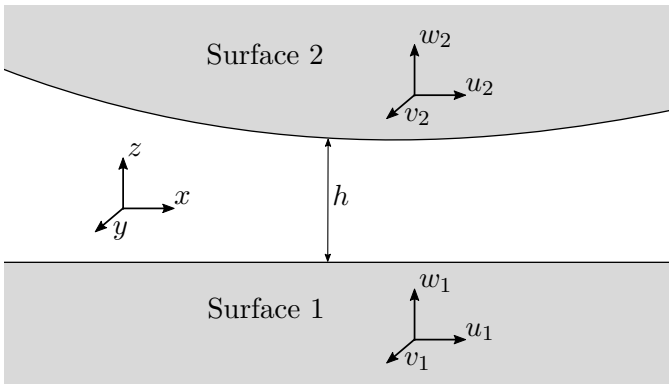

Figure 2-1: Thin film of fluid between two surfaces, moving with velocities u, v and w.

(2-1), are written in one partial differential. This gives the following equation, consisting of three parts:

$$\underbrace{\frac{\partial}{\partial x}\left(\frac{\rho\, h^3}{12\,\eta}\frac{\partial p}{\partial x}\right)}_{\text{Poiseuille flow}} - \underbrace{\frac{\partial}{\partial x}\left(\frac{\rho\, h\,(u_1+u_2)}{2}\right)}_{\text{Couette flow}} = \underbrace{\frac{\partial}{\partial t}(\rho\, h)}_{\text{Dynamic effects}} \tag{2-2}$$

Poiseuille flow describes the flow due to pressure gradients in the fluid.

Couette flow describes the flow due to surface velocities and can be split up into three parts by expanding the partial derivative to x:

$$\frac{\partial}{\partial x}\left(\frac{\rho\, h\,(u_1+u_2)}{2}\right) = \underbrace{\frac{h\,(u_1+u_2)}{2}\frac{\partial \rho}{\partial x}}_{\text{Density wedge}} + \underbrace{\frac{\rho\,(u_1+u_2)}{2}\frac{\partial h}{\partial x}}_{\text{Physical wedge}} + \underbrace{\frac{\rho\, h}{2}\frac{\partial}{\partial x}(u_1+u_2)}_{\text{Stretch}} \tag{2-3}$$

The *density wedge* describes a flow caused by a change in lubricant density. This could for example be caused by a temperature change in the lubricant.

The *physical wedge* describes how a change in height causes a flow. To satisfy continuity, this flow must be balanced with a Poiseuille flow. This pressure generating mechanism is often used in journal and sliding thrust bearings to carry a load. To generate a positive load carrying pressure, a decrease of fly height in the sliding direction is needed.

Stretch describes a flow caused by a change in surface velocity in the sliding direction. This can be caused by having the surfaces deform. This effect is not encountered in conventional bearings.

Dynamic effects can be split up into two parts:

$$\frac{\partial}{\partial t}(\rho\, h) = \underbrace{\rho\,(w_2 - w_1) - \rho\, u_2 \frac{\partial h}{\partial x}}_{\text{Squeeze}} + \underbrace{h\frac{\partial \rho}{\partial t}}_{\text{Local expansion}} \tag{2-4}$$

Squeeze terms generate a flow by direct up or down movement of the surfaces, or by sideways movement of non parallel surfaces.

Local expansion terms generate a flow by varying density in time. This could for example be caused by heating of the lubricant.

2-2 Reynolds equation for compressible lubricants

In (2-2), fluid density is present in all three parts of the equation, and is a function of both space and time. To allow an easier solution of the equation, density is sometimes assumed constant, so it no longer is a function of space and time. Thus, it can be removed from both sides of the equation, providing that thermal effects are not abound. This assumption is considered valid for liquid lubricants, since density of a liquid varies insignificantly with pressure, and is only dependent on temperature. Therefore, fluids are called incompressible, and the resulting equation is called the incompressible Reynolds equation.

However, when gas is used as lubricant, quite the opposite is true: because gas is compressible, density is highly dependent on pressure. Lubricant density can not be considered constant in this case . To find a solution to (2-2), density is substituted with pressure via the ideal gas law:

$$\rho = \frac{p}{R_s\, T} \tag{2-5}$$

where ρ is fluid density in $\mathrm{kg/m^3}$, p is pressure in Pa, R_s is specific gas constant in $\mathrm{m^2/s^2K}$ and T is temperature in K. To plug this equation into Reynolds equation, constant temperature is assumed, as in assumption 7. Combining (2-5) with the 1-D Reynolds equation (2-2) gives:

$$\frac{\partial}{\partial x}\left(\frac{p\, h^3}{12\, \eta\, R_s\, T}\frac{\partial p}{\partial x}\right) - \frac{\partial}{\partial x}\left(\frac{p\, h\, (u_1 + u_2)}{2\, R_s\, T}\right) = \frac{\partial}{\partial t}\left(\frac{p\, h}{R_s\, T}\right) \tag{2-6}$$

By taking note that, at this point, viscosity, specific gas constant and temperature are all constants, and assuming that only surface 2 is moving and not deforming, this equation can be simplified to:

$$\frac{\partial}{\partial x}\left(p\, h^3 \frac{\partial p}{\partial x}\right) - 6\, u_2\, \eta\, \frac{\partial}{\partial x}\left(p\, h\right) = 12\, \eta\, \frac{\partial}{\partial t}\left(p\, h\right) \tag{2-7}$$

2-3 Reynolds equation in polar coordinates

When modelling circular bearings, a polar coordinate system is more suitable . Therefore, Reynolds equation is also derived in a polar coordinate system in Appendix A. Assuming axial symmetry, neglecting Couette flow and substituting the ideal gas law, the resulting equation is:

$$\frac{1}{r}\frac{\partial}{\partial r}\left(\frac{r\, p\, h^3}{12\, \eta\, R_s\, T}\frac{\partial p}{\partial r}\right) = \frac{\partial}{\partial t}\left(\frac{p\, h}{R_s\, T}\right) \tag{2-8}$$

2-4 Conclusions and outlook

The flow and pressure build up of a thin film can be modelled with Reynolds equation. The most important assumptions are that flow is laminar, and that lubricant is Newtonian and of constant viscosity. The physical interpretation of the terms in the equation have been discussed. Reynolds equation can be modified to deal with compressibility of gas lubricant via the ideal gas law. Two coordinate systems are treated: Cartesian and polar. In the next chapter, Reynolds equation will be used to model a circular air bearing. Different techniques of solving Reynolds equation will be compared.

3

Static air bearing modelling

In the previous chapter, Reynolds equation has been derived. This equation describes the pressure distribution in a thin viscous fluid, as found in fluid film bearings. The equation has been expanded for compressible lubricants like air, and derived both in Cartesian and polar coordinate systems.

In this chapter, the static modelling of externally pressurized circular air bearings is explored. First, the system of restrictor and thin film is investigated, explaining how an air bearing achieves stiffness. Then, a model for the restrictor will be introduced and an analytical solution of Reynolds equation will be used as a model for the thin film. Finally, multiple alternative solving methods for Reynolds equation will be explored and compared, leading to an efficient model for circular aerostatic bearings.

3-1 General working principle

In Figure 3-1, a schematic cross section of a circular air bearing is drawn. The bearing is fed with a source pressure P_s, into the middle of the thin film with fly height h. This causes a flow to the outside of the film, gradually decreasing the pressure to the ambient pressure P_a, at the sides of the bearing.

Underneath the schematic cross section, the pressure profile in the thin film is shown. Because pressure in the film is higher than ambient pressure, a net force acts upwards on the bearing surface, determined by the integral of the pressure over the bearing surface. This force gives the bearing the capacity to carry a load, and therefore this force is called the load capacity W.

In order for the bearing to be stable, the load capacity and thus the pressure profile should be able to change for different loads. This means the bearing should have stiffness.

Bearing stiffness

A thrust bearing achieves stiffness by adding a restrictor in the flow path from source to ambient. This can be understood by comparing the system with restrictor and thin film in series as an electrical circuit. Pressure can be seen as voltage, lubricant flow as current. The

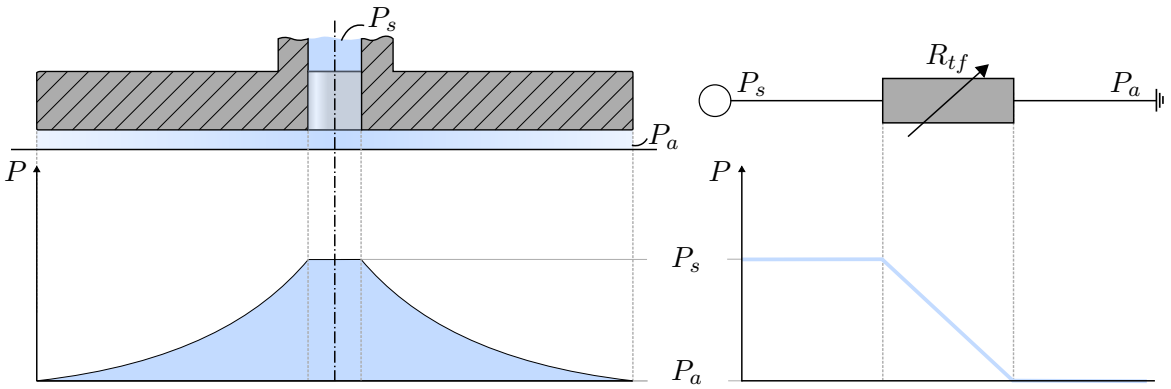

Figure 3-1: Schematic view of circular air bearing without restrictor, with pressure distribution in the thin film drawn underneath. The air feed diameter is such that it has no significant influence on the thin film pressure. On the right side, the electrical equivalent circuit is drawn.

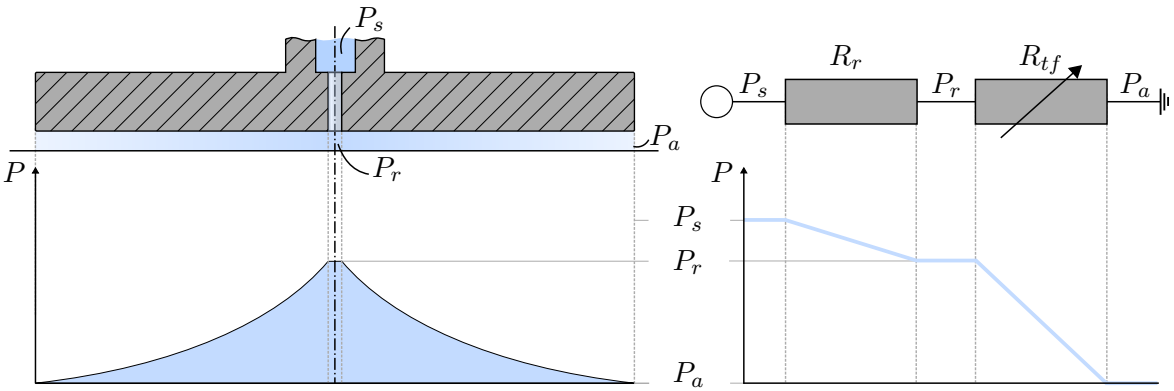

Figure 3-2: Schematic view of circular air bearing with restrictor and electrical equivalent. The air feed diameter is small and has a significant resistance on the flow. Therefore it is called a restrictor. It reduces the pressure from the source pressure to the restrictor pressure entering the middle of the film.

source pressure can be seen as a voltage source, the ambient pressure as ground. Both the restrictor and thin film are resistors. The restrictor has constant resistance. Resistance of the thin film depends on the film height.

First, a system without restrictor is analysed, as drawn in Figure 3-1. The electrical equivalent is drawn on the right side. Only the thin film resistance causes a significant pressure drop. Since load capacity is given by the pressure drop over the thin film, a change in pressure drop causes a change in load capacity. However, the pressure drop in this system is constant, independent on the thin film resistance and therefore height of the thin film. Because the film height is uniform, the distribution of pressure is also constant with film height. There is no mechanism that changes the pressure distribution as function of the film height. Therefore, load capacity is independent on film height and this system has no stiffness.

For the bearing to have stiffness, load capacity should be dependent on film height. This can be achieved by adding a second resistor in the circuit, called the restrictor, as drawn in figure Figure 3-2. The restrictor has a constant resistance. The pressure at the middle

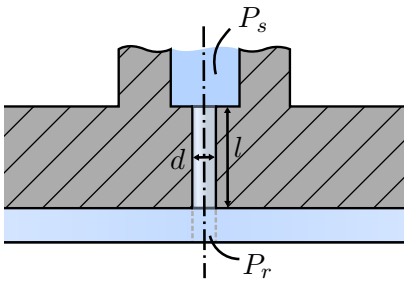

Figure 3-3: Schematic view of capillary restrictor. Pressure drops from P_s to P_r through a restrictor with length l and diameter d.

of the thin film controls the load capacity and is called restrictor pressure P_r. A change in thin film resistance will effect the ratio of resistances R_r and R_{tf} and therefore change the restrictor pressure. This makes the load capacity dependent on the fly height, giving the bearing stiffness.

To model bearing stiffness and see how it can be influenced, equations will be derived for both the restrictor and thin film in the following sections.

3-2 Restrictor model

There are different methods to restrict flow. Most common are orifice restrictors, a porous medium or capillary restrictors. In contrast to orifice restrictors, capillary restrictors are assumed to promote laminar flow into the thin film. For high precision applications, as treated in this thesis, a steady laminar flow is considered to give the best results and therefore capillary restrictors will be used.

A capillary restrictor is sketched in Figure 3-3. It is a long thin hole through which the pressure is reduced. According to Poiseuille's law for laminar flow [22, (6.12)] through a long cylindrical pipe, the volume flow is:

$$\phi = \frac{\pi\, d^4}{128\, \eta\, l} \left(P_s - P_r\right) \tag{3-1}$$

For Poiseuille's law to be valid, the tube must be long ($l/d > 20$) and the flow must be laminar ($Re < 1000$). The mass flow can be computed by multiplying volume flow with fluid density, which has to be approximated since gas is compressible. The density is computed with the ideal gas law, averaging the pressure over the restrictor. The ideal gas law as stated in Equation 2-5 now gives:

$$\rho = \frac{P_s + P_r}{2} \frac{1}{R_s\, T} \tag{3-2}$$

Multiplying the volume flow with the density gives:

$$\dot{m} = \frac{\pi\, d^4}{256\, l} \frac{1}{\eta\, R_s\, T} \left(P_s^2 - P_r^2\right) \tag{3-3}$$

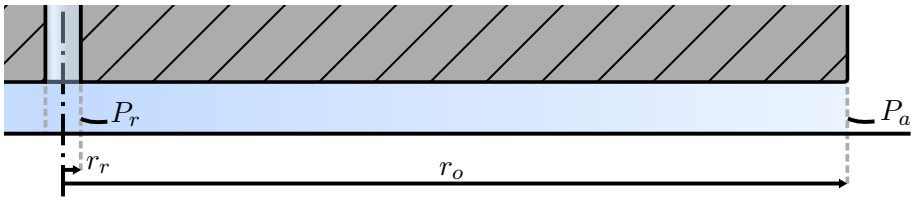

Figure 3-4: Schematic view of thin film. Pressure $p(r)$ drops from $P_r\,(r_r)$ to $P_a\,(r_o)$.

This is the same equation as stated in [10, (12.3)]. To simplify equations further, the resistor conductivity G_r is introduced, relating squared pressure difference with mass flow:

$$G_r = \frac{\pi\, d^4}{256\, l}\frac{1}{\eta\, R_s\, T}, \quad \dot{m} = G_r\left(P_s^2 - P_r^2\right) \tag{3-4}$$

3-3 Thin film model

In this section, an analytical solution for the resistance and mass flow of an axisymmetric thin film is developed. Starting with the axisymmetric Reynolds equation as stated in (2-8) and assuming steady state removes the time derivatives from the right hand side, changing the right hand side to zero. Also, the surfaces are assumed parallel, meaning that h is constant. Lastly, since the right hand side is zero, constants can be left out, giving the following equation as shown in [23, (2.139)]:

$$\frac{\partial}{\partial r}\left(r\, p\frac{\partial p}{\partial r}\right) = 0 \tag{3-5}$$

With boundary conditions for $p(r)$ as drawn in Figure 3-4:

$$p\,(r_r) = P_r, \quad p\,(r_o) = P_a \tag{3-6}$$

the mass flow can be shown to be [23, 2.162]:

$$\dot{m} = \frac{\pi\, h^3}{12\,\eta\, R_s\, T}\frac{P_r^2 - P_a^2}{\ln\left(r_o/r_r\right)} \tag{3-7}$$

Defining the thin film conductivity as G_{tf}:

$$G_{tf} = \frac{\pi\, h^3}{12\,\eta\, R_s\, T}\frac{1}{\ln\left(r_o/r_r\right)}, \quad \dot{m} = G_{tf}\left(P_r^2 - P_a^2\right) \tag{3-8}$$

3-4 Modelling the air bearing system

With equations derived for mass flow through both thin film and restrictor, different techniques for setting up and solving the system of equations will be discussed in this section. The goal is to find the load capacity for a given fly height. First, the bearing geometry will be defined. After that, the multiple resistance method is discussed. Next, a finite volume approach is used, which is the basis for a dynamic model discussed in the next chapter. The last method that will be treated is using the finite element method as implement by COMSOL. All three methods will be compared in the last subsection.

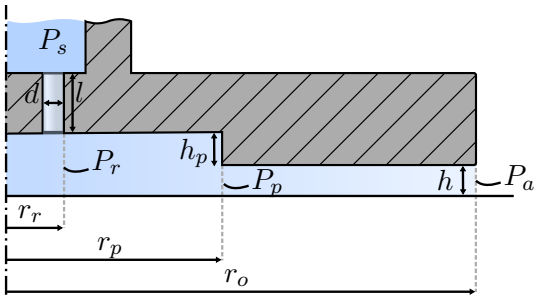

Figure 3-5: Declaration of geometry variables and pressures for the air bearing model, drawn in axisymmetric view. The restrictor is put off centre, at radius r_r. This bearing also has a pocket, a step in the bearing surface, with height h_p.

3-4-1 Bearing geometry

Geometry of the modelled bearing is drawn in Figure 3-5. The restrictor can be put of centre at radius r_r. Because of axial symmetry, pressure for radii smaller than the restrictor radius are constant and equal to the restrictor pressure P_r. A step in film height, called a pocket, has radius r_p and height h_p.

3-4-2 Multiple resistance method

To find the load capacity for a given fly height with the multiple resistance method, first P_r and P_p are computed. By noting that the mass flow through the system must be constant, a system of equations can be set up.

By using the equations for mass flow through the restrictor (3-4) and thin film (3-8), the following system of equations can be derived:

$$\dot{m} = G_r \left(P_s^2 - P_r^2\right) = G_p \left(P_r^2 - P_p^2\right) = G_e \left(P_p^2 - P_a^2\right) \tag{3-9}$$

where G_r is the restrictor conductivity and G_p and G_e the conductivity of the pocket and edge. Unknowns are $\dot{m}$, P_r and P_p. Since this system is linear in the squared pressures, the system can be written in matrix form and solved:

$$\begin{bmatrix} G_r & 0 & 1 \\ G_p & -G_p & -1 \\ 0 & G_e & -1 \end{bmatrix} \begin{bmatrix} P_r^2 \\ P_p^2 \\ \dot{m} \end{bmatrix} = \begin{bmatrix} G_r\, P_s^2 \\ 0 \\ G_e\, P_a^2 \end{bmatrix} \tag{3-10}$$

Alternatively, the pressures can be found by treating the system as linear circuit where the voltage is the pressure squared. The mass flow can be solved with:

$$\dot{m} = \frac{P_s^2 - P_a^2}{\frac{1}{G_r} + \frac{1}{G_p} + \frac{1}{G_e}} = \left(P_s^2 - P_a^2\right) \frac{G_r\, G_p\, G_e}{G_r\, G_p + G_r\, G_e + G_p\, G_e} \tag{3-11}$$

Then, pressures can be found with (3-9).

To find the load capacity, the film pressure between P_r and P_p, and P_p and P_a needs to be determined. Taking the pressure drop from P_p to P_a as example, this can be written as [10], [23]:

$$p(r) = P_a \sqrt{\left(\frac{P_p}{P_a}\right)^2 - \frac{\ln(r/r_p)}{\ln(r_o/r_p)}\left(\left(\frac{P_p}{P_a}\right)^2 - 1\right)} \tag{3-12}$$

The load capacity is given by the integral of this equation and the integral under the pocket plus the pressure at the restrictor minus the ambient pressure on the bearing:

$$W = \underbrace{\pi\, r_r^2\, P_r}_{\text{restrictor}} + \underbrace{\int_{r_r}^{r_p} 2\,\pi\, r\, p(r)\, dr}_{\text{pocket}} + \underbrace{\int_{r_p}^{r_o} 2\,\pi\, r\, p(r)\, dr}_{\text{edge}} - \underbrace{\pi\, r_o^2\, P_a}_{\text{ambient}} \tag{3-13}$$

Both [10] and [24] state that the integrals in this equation can not be solved analytically. However, the integral can be shown to be [23, (2.159)]:

$$\int_{r_p}^{r_o} 2\,\pi\, r\, p(r)\, dr = \pi\, r_o^2\, P_p \left(\frac{r_p}{r_o}\right)^2 \mathrm{e}^{\frac{2}{a}} \sqrt{\frac{\pi\, a}{8}} \left[\mathrm{Erf}\left(\sqrt{\frac{2}{a}}\right) - \mathrm{Erf}\left(\frac{P_a}{P_p}\sqrt{\frac{2}{a}}\right)\right] \tag{3-14}$$

where

$$a = \frac{1 - \left(\frac{P_a}{P_p}\right)^2}{\ln\left(\frac{r_o}{r_p}\right)} \tag{3-15}$$

Where $\mathrm{Erf}(x)$ is the Gauss error function. Alternatively, the integrals in (3-13) can be solved numerically without substitution of (3-14). This describes the first method of finding the load capacity as function of the fly height.

3-4-3 Finite volume method

Alternative to the multiple resistance method, a finite volume approach for solving Reynolds equation has been developed. Although the multiple resistance model suffices, this alternative method has been built to provide the basis for a dynamic model, which will be treated in the next chapter.

Dimensionless numbers

Since fly heights are in the order of 10×10^{-5} m and are cubed in the conductivity, typical values for conductivity are in the order of 10^{-15} or smaller. To improve numerical stability, equations have been written in a dimensionless form by introducing dimensionless radius, pressure and height:

$$\begin{aligned} r\ [\mathrm{m}] &= \bar{r}\ [-]\ R\ [\mathrm{m}] \\ p\ [\mathrm{Pa}] &= \bar{p}\ [-]\ P\ [\mathrm{Pa}] \\ h\ [\mathrm{m}] &= \bar{h}\ [-]\ H\ [\mathrm{m}] \end{aligned} \tag{3-16}$$

A common choice for R is the outside radius r_o. P is choosen as ambient pressure P_a and H it is at the fly height h.

Starting with (2-8), removing all constants except the film height and substituting the dimensionless variables, gives:

$$\frac{H^3\,P^2}{R}\frac{\partial}{\partial \bar{r}}\left(\bar{r}\,\bar{h}^3\,\bar{p}\frac{\partial \bar{p}}{\partial \bar{r}}\right) = 0 \tag{3-17}$$

Discretization and setting up equations

To solve (3-17), the differential equation has been discretized. The thin film has been divided into volumes, and a set of equations has been set up describing how the pressure in a specific volume depends on the pressures in neighbouring volumes. Flow of air through the restrictor and boundary conditions are also discretized. This leads to a system of equations for the pressure in each volume. The system of equations can be solved to find the pressures in each volume, satisfying the boundary conditions.

With the solution of (3-17) numerically approximated, the dimensionless load capacity $\bar{W}$ can be found by integrating the pressures in the elements. The dimensionless load capacity can be converted to dimensioned load capacity by multiplying with the conversion factors as defined in (3-16).

The process of discretization, setting up equations, solving and finding the load capacity is treated in appendix B-1. This section only has shortly summarized the process from differential equation to solution. For a more detailed insight into this process, the reader is encouraged to read the appendix. All mathematics are derived there, giving the reader an opportunity to program his or her own finite volume solution using only this thesis as reference.

3-4-4 Finite Element Method: COMSOL Multiphysics

A third static model has been developed in COMSOL, a commercial finite element package. This model was mainly used to verify the solutions of the finite volume model. The main advantage of using COMSOL is the ease at which the model is created. Differential equations can be put in directly, with COMSOL taking care of discretization.

The model is set up using a 1D axisymmetric component with General form PDE physics. The conservative flux is set to:

$$\Gamma = \bar{r}\,\bar{h}^3\,\bar{p}\,\frac{\partial \bar{p}}{\partial \bar{r}} \tag{3-18}$$

The source is added as a flux:

$$g = \frac{\bar{G}_r}{2}\left(\bar{P}_s^2 - \bar{p}^2\right) \tag{3-19}$$

the factor 2 compensates for (B-3). The boundary condition at $r = 1$ is taken care of with a Dirichlet boundary condition, and the symmetry boundary conditions are taken care of automatically by COMSOL since the component is axisymmetric.

3-4-5 Model comparison

In this section, pressure distribution and load capacity as found by the different models are compared. Also, an analysis of model run times and some considerations for a parameter study are made. All models are programmed in MATLAB R2014b, except the COMSOL model which has been created in version 4.4.

Pressure distribution

The pressure distribution is computed with three different models: The multiple resistance model, the finite volume model and the COMSOL finite element model. For the parameters as listed in Table 3-1, the results are plotted in Figure 3-6. All models show equal pressure distributions. Three distinct regions are clearly shown: first the constant pressure on the inside of the restrictor radius, then a small drop in pressure caused by the pocket, from $r = 0.1\,\mathrm{m}$ to $r = 0.4\,\mathrm{m}$ and last a greater drop in pressure over the edge.

Load capacity

The load capacity for a given pressure distribution can be found in four ways: by analytical integration using the Gauss error function (3-14), by numerical integration of the pressure distribution, by summing finite volume pressures and by using COMSOL's built in integration over its finite elements. The results can be found in Table 3-2.

Analytical integration, numerical integration and COMSOL show almost identical values. The finite volume method result is accurate up to the third significant number. If the volume count is increased, the results approaches that of the other models.

Run time and parameter study considerations

The run times for 500 runs are printed in Table 3-3. Both finite volume method and COMSOL use 250 linear elements, giving 250 degrees of freedom.

The analytical integral is the fastest by far. Numerical integration and finite volume method are close together at second and third. COMSOL is a lot more slow, probably caused by user interface overhead.

When conducting an expensive parameter study, different considerations are to be taken. If only a static solution is required, Gauss approximation is fast and accurate. The results of this method, however, rely on the accuracy of $\mathrm{Erf}(x)$. For high pressure drops, the results of $\mathrm{Erf}\left(\sqrt{\frac{2}{a}}\right) - \mathrm{Erf}\left(\frac{P_a}{P_p}\sqrt{\frac{2}{a}}\right)$ approaches zero, resulting in an inaccurate approximantion of load capacity. Constraints and validity checks should be added to ensure the solution is valid. Numerical integration does not risk this error. It is therefore more reliable and requires less effort to be made robust. This comes a cost of runtime. Both models are simple to program.

Finite volume should only be used if dynamics are also considered, which will be further developed in the next chapter. It is not as fast or accurate as the previous two models, and a greater programming effort.

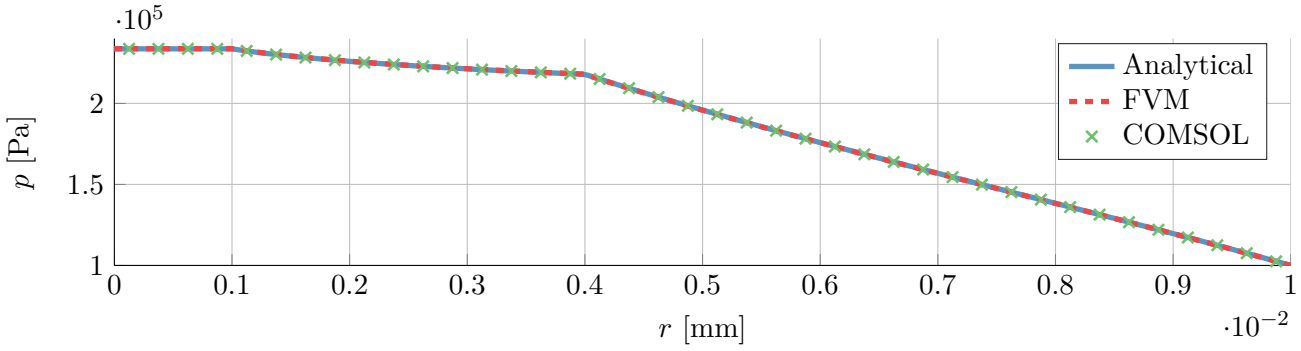

Figure 3-6: Thin film pressure versus radius. All solutions match.

Table 3-1: List of model parameters

variable	value	unit
G_r	$2 \cdot 10^{-16}$	m^2s^3/kg
P_s	$3{\cdot}10^5$	Pa
P_a	$1{\cdot}10^5$	Pa
r_r	$1{\cdot}10^{-3}$	m
r_p	$4{\cdot}10^{-3}$	m
r_o	$10{\cdot}10^{-3}$	m
h_p	$10{\cdot}10^{-6}$	m
h	$10{\cdot}10^{-6}$	m
η	$18{\cdot}10^{-6}$	Pa s
R_s	287	m^2/s^2K
T	293	K

Table 3-2: Modelled load capacities

model	load capacity [N]
Gauss approx	19.2096
Numerical int	19.2096
Finite volume	19.1828
COMSOL	19.2097

Table 3-3: Computation time for 500 runs

model	time [s]
Analytical int	0.11
Numerical int	0.77
Finite volume	0.93
COMSOL	9

The COMSOL model is easy to set up, but given its slow runtime, proves to be unwieldy for an extensive parameter study.

3-5 Conclusions and outlook

In this chapter, static modelling of externally pressurized circular air bearings has been discussed. The function of a restrictor in combination with a thin film is explained as a way to achieve stiffness. Models for mass flow through both restrictor and thin film are developed, leading to different solution strategies for finding load capacity for a given fly height and bearing geometry.

The multiple resistance method, with two possible integration options, is fast and accurate. The finite volume method is slower and less accurate, but provides a basis for the dynamic model which is developed in the next chapter. The COMSOL model is primarily used as reference, since it is quite slow in comparison.

In the next chapter, the dynamic model will be treated. By linear perturbation of Reynolds equation, stiffness and damping as function of frequency, fly height and bearing geometry will be determined.

4

Dynamic air bearing modelling

In the previous chapter, different models for load capacity as function of fly height and bearing geometry have been developed and compared. In this chapter, a model will be developed to determine stiffness and damping of a thin film of air when subjected to a sinusoidal squeeze motion: a change of fly height in time. Using a technique called linear perturbation, the effects of squeeze motion around a static solution will be explored, resulting in a differential equation. Different solution techniques will be discussed, of which two will be chosen. The solutions found by the different techniques, and properties of these techniques, will be discussed.

4-1 Linear perturbation of Reynolds equation

To gain more insight in the dynamic behaviour of air bearings with vibrating surfaces, Reynolds equation is linearly perturbed. First, the process of perturbation is explained. The derivation of the perturbed Reynolds equation is shown after that.

4-1-1 Stiffness and damping

Perturbation is a mathematical technique for finding an approximate solution to a problem, by starting from the exact solution of a related, simpler problem. In this thesis the static solution is perturbed by a real and imaginary sinusoidal signal with small amplitude. This leads to the stiffness and damping of the thin film. The static height h_0 is perturbed with δh, leading to a change in pressure δp:

$$\begin{aligned} h &= h_0 + \delta h(t), \quad \delta h = \tilde{h}\, e^{j\,\omega\, t} \\ p &= p_0 + \delta p(t), \quad \delta p = \tilde{p}\, e^{j\,\omega\, t} \end{aligned} \tag{4-1}$$

The perturbed load capacity can be found by integrating the perturbed pressure, giving δW. Calling the unperturbed load capacity W_0, the stiffness can be found with:

$$k = -\frac{\partial W}{\partial h} \approx -\frac{\delta W - W_0}{(h_0 + \delta h) - h_0} = -\frac{\int p_0 + \delta p\, dr - \int p_0\, dr}{(h_0 + \delta h) - h_0} = -\frac{\int \tilde{p}\, dr}{\tilde{h}} \tag{4-2}$$

Thus, stiffness can be found by solving the perturbed Reynolds equation and integrating the real part of the perturbed pressure. Damping, defined as the negative change of load with velocity, can be found with:

$$c = -\frac{\partial W}{\partial \dot{h}} \approx -\frac{\delta W - W_0}{\left(\dot{h}_0 + \delta\dot{h}\right) - \dot{h}_0} = -\frac{\int \tilde{p}\, dr}{j\,\omega\,\tilde{h}} \tag{4-3}$$

Therefore, damping can be found by integrating the imaginary part of the perturbed pressure and dividing by the frequency.

4-1-2 Substitution of perturbed variables

The perturbed height and pressure are substituted in the axisymmetric Reynolds equation as described in (2-8), which is copied for the reader's convenience:

$$-\frac{1}{r}\frac{\partial}{\partial r}\left(\frac{r\,p\,h^3}{12\,\eta\,R_s\,T}\frac{\partial p}{\partial r}\right) + \frac{\partial}{\partial t}\left(\frac{p\,h}{R_s\,T}\right) = 0 \tag{4-4}$$

Both p and h are function of time. All other variables are assumed constant. Substituting (4-1) into this equation gives:

$$-\frac{1}{12\,\eta\,r}\frac{\partial}{\partial r}\left[r\,(p_o+\delta p)\,(h_0+\delta h)^3\,\frac{\partial\,(p_0+\delta p)}{\partial r}\right] + \frac{\partial}{\partial t}\left[(p_o+\delta p)\,(h_0+\delta h)\right] = 0 \tag{4-5}$$

Neglecting all higher order terms in δ, like $\delta h\,\delta p$, stating $\frac{\partial}{\partial t}(p_0) = 0$ and $\frac{\partial}{\partial t}(h_0) = 0$ and substituting $\delta h = \tilde{h}\,e^{j\,\omega\,t}$ and $\delta p = \tilde{p}\,e^{j\,\omega\,t}$ gives:

$$\begin{aligned} -\frac{1}{12\,\eta\,r}\frac{\partial}{\partial r}\Bigg(r\,h_0^3\,p_0\,\frac{\partial p_0}{\partial r} + r\,h_0^3\,p_0\,\frac{\partial \tilde{p}}{\partial r}e^{j\,\omega\,t} + r\,h_0^3\,\tilde{p}\,e^{j\,\omega\,t}\frac{\partial p_0}{\partial r} + 3\,h_0^2\,\tilde{h}\,e^{j\,\omega\,t}\,p_0\frac{\partial p_0}{\partial r}\Bigg) + \\ j\,\omega\,p_0\,\tilde{h}\,e^{j\,\omega\,t} + j\,\omega\,h_0\,\tilde{p}\,e^{j\,\omega\,t} = 0 \end{aligned} \tag{4-6}$$

The first part in brackets, $r\,h_0^3\,p_0\,\frac{\partial p_0}{\partial r}$, is the static solution and is equal to zero, as shown in chapter 3. Therefore it can be removed. All remaining term are now multiplied with $e^{j\,\omega\,t}$, which can therefore also be removed. This gives the perturbed Reynolds equation:

$$-\frac{\partial}{\partial r}\left(r\,h_0^3\,p_0\,\frac{\partial \tilde{p}}{\partial r} + r\,h_0^3\,\tilde{p}\,\frac{\partial p_0}{\partial r} + 3\,h_0^2\,\tilde{h}\,p_0\frac{\partial p_0}{\partial r}\right) + 12\,\eta\,r\,j\,\omega\,\left(p_0\,\tilde{h} + h_0\,\tilde{p}\right) = 0 \tag{4-7}$$

This equation describes the change in pressure in radial direction in a thin film as a result of small deviation of fly height.

The perturbed Reynolds equation contains the static solution and the first and second derivative of the static solution to r. This means that the static solution has to be solved and substituted before the perturbed equation can be solved.

4-2 Solving the perturbed Reynolds equation

With the perturbed Reynolds equation set up, this section will deal with different solving techniques. The most promising techniques will be further developed.

4-2-1 Solving techniques

The change of perturbed pressure is governed by (4-7). To solve this equation, boundary conditions have to be added. At the inner edge, symmetry demands no change in perturbed pressure: $\frac{\partial \tilde{p}(r=0)}{\partial r} = 0$. At the outside border, the perturbed pressure is 0: $\tilde{p}(r = r_o) = 0$. This makes this a boundary value problem. Different solution techniques are tried and will be discussed subsequently.

Shooting method

The shooting method is a method for solving a boundary value problem by reducing it to the solution of an initial value problem. Simply put, it changes starting conditions to iterate to a solution that fits the boundary conditions.

A shooting method was implemented in Matlab which could iterate to a solution. However, the iteration process was quite computationally heavy, taking multiple seconds per solution, and therefore a better method was sought.

Finite Element Method: COMSOL Multiphysics

Similar to the model as discussed in subsection 3-4-4, this differential equation can also be solved by the finite element package COMSOL. This model is easy to build, but too slow for an extensive parameter study. Because it was used extensively to check results of different models, it is discussed in greater detail in a next subsection.

Finite volume

Lastly, a finite volume model is developed to solve the perturbed Reynolds equation. It gives reliable results and is fast enough to be used in a parameter study. The finite volume model will be discussed in the next subsection.

4-2-2 Finite volume method

In this subsection, development of the dynamic finite volume method model is treated. Static solutions required in the perturbed equation are found with the static finite volume method model as treated in the previous chapter.

The steps in developing a finite volume model to solve the perturbed Reynolds equation are similar to those for Reynolds equation, as described in subsection 3-4-3. First, the perturbed Reynolds equation is put into a dimensionless form by defining an extra dimensionless number:

$$\omega \ [1/\mathrm{s}] = \bar{\omega} \ [-] \ \Omega \ [1/\mathrm{s}] = \bar{\omega} \ [-] \ \frac{P \, H^2}{12 \, \eta \, R^2} \ [1/\mathrm{s}] \tag{4-8}$$

Substituting this into (4-7) gives:

$$-\frac{\partial}{\partial \bar{r}} \left(\bar{r} \, \bar{h}_0^3 \, \bar{p}_0 \, \frac{\partial \tilde{\bar{p}}}{\partial \bar{r}} + r \, \bar{h}_0^3 \, \tilde{\bar{p}} \, \frac{\partial \bar{p}_0}{\partial \bar{r}} + 3 \, \bar{h}_0^2 \, \tilde{\bar{h}} \, \bar{p}_0 \frac{\partial \bar{p}_0}{\partial \bar{r}} \right) + \bar{r} \, j \, \bar{\omega} \left(\bar{p}_0 \, \tilde{\bar{h}} + \bar{h}_0 \, \tilde{\bar{p}} \right) = 0 \tag{4-9}$$

By discretizing this equation, the air feed equation and boundary conditions, a linear set of equations is found. Note that the perturbed pressure is a complex number. To simplify solving, the complex equations are split up into real and imaginary parts, leading to a final set of equations which can be solved to find the perturbed pressure. Dimensionless stiffness and damping can be determined by integrating the perturbed pressure solution over the radius, which in discretized form is equal to summing the volume areas multiplied with values for pressure. The dimensionless stiffness and damping can be converted to dimensioned numbers by multiplying with the conversion factors.

This process is fully documented in appendix B-2. For an appreciation of the effort needed to solve this differential equation and develop a working model, a view at the appendix is suggested. Using only this appendix as reference, a fully working finite volume implementation for solving the perturbed Reynolds equation can be programmed.

4-2-3 Finite element method: COMSOL

To validate the finite volume model, the perturbed Reynolds equation is also solved using COMSOL. The model is very similar to the static model as discussed in subsection 3-4-4. A 1D axisymmetric component has been used with general form PDE physics. The conservative flux is set to:

$$\Gamma = \bar{r}\,\bar{h}^3\,\bar{p}_0\,\frac{\partial\tilde{\bar{p}}}{\partial\bar{r}} + \bar{r}\,\bar{h}^3\,\tilde{\bar{p}}\,\frac{\partial\bar{p}_0}{\partial\bar{r}} + 3\,\bar{r}\,\bar{h}^2\,\tilde{\bar{h}}\,\bar{p}_0\,\frac{\partial\bar{p}_0}{\partial\bar{r}} \tag{4-10}$$

the source term is set to:

$$f = \frac{12\,\eta\,R^2\,i\,\Omega}{P\,H^2}\,\bar{r}\,\left(\bar{p}_0\,\tilde{\bar{h}} + \bar{h}\,\tilde{\bar{p}}\right) \tag{4-11}$$

The feed is modelled with a flux set to:

$$g = \bar{G}_r\,\bar{p}_0\,\tilde{\bar{p}} \tag{4-12}$$

The boundary on $\bar{r} = 1$ was set with a Dirichlet boundary condition, the boundary on $\bar{r} = 0$ is taken care of by the axisymmetry of the component.

4-2-4 Comparison of solutions

With both the finite volume method as a COMSOL method set up, the solutions to the perturbed Reynolds equation can be compared. First, perturbed pressure versus radius is analysed for both models. Next, the integrals of the real and imaginary part of the perturbed pressure, leading to stiffness and damping, are compared. At last, perturbed stiffness is related to a finite difference stiffness of the static solution.

Dynamic pressure

In Figure 4-1, the dynamic pressures are plotted. Bearing geometries are equal to those of the previous chapter, as listed in Table 3-1. The real and imaginary parts are plotted for

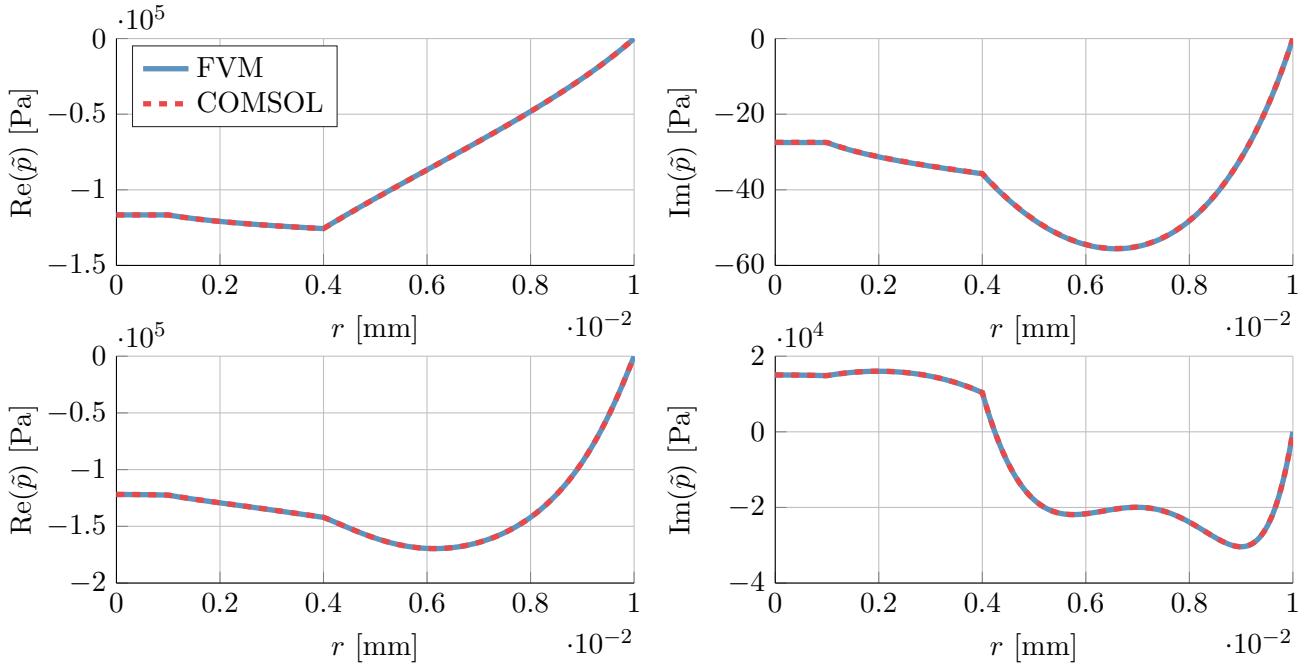

Figure 4-1: Dynamic pressure in thin film at low frequencies, top row, and high frequency, bottom row. Since both plots are made for identical bearing geometry, and the dynamic pressure changes with frequency, both stiffness and damping are frequency dependent.

Table 4-1: Stiffness and damping results for the finite volume method model and COMSOL

	1 Hz		1×10^4 Hz	
model	k [N/m]	c [Ns/m]	k [N/m]	c [Ns/m]
Finite volume	2.140×10^6	1.999×10^2	4.029×10^6	7.697
COMSOL	2.141×10^6	1.996×10^2	4.029×10^6	7.697

a solution at 1 Hz and at 1×10^4 Hz. The finite volume method solutions match with the COMSOL model solutions in both cases. This is also reflected in the values for stiffness and damping, which are printed for both frequencies in Table 4-1. This validates the finite volume method as a method of solving the perturbed Reynolds equation.

Note that only the frequency changes between the upper and lower row in Figure 4-1. Since the surface area beneath the graphs, which is a measure for stiffness and damping, changes between both cases, stiffness and damping are frequency dependent.

For 500 runs, the finite volume model with 250 volumes takes 2.95 s, while COMSOL with 250 linear elements takes 19 s for 500 runs. Being faster, the finite volume method is more suitable for an extensive parameter study.

Both solving times are significantly longer than their static counterparts. Because the static solution is needed to solve the perturbed equation, every run solves both the static and perturbed equations.

Comparison with static model stiffness

As an additional check, the perturbed stiffness at a low frequency is compared to the stiffness that can be derived from the static model via finite difference. For the model with geometries as stated in Table 3-1, finite difference on the numerical integral gives 2.14×10^6 N/m, which is equal to that of the finite volume model at 1 Hz. This validates that perturbation of Reynolds equation results in the correct stiffness at low frequencies.

4-2-5 Range of validity of the model

In chapter 2, Reynolds equation and assumptions are discussed. In assumption 6, fluid inertia is neglected. The validity of this assumption for both radial flow as for squeeze motion is discussed in this subsection.

Navier - Stokes equations describe the motion of viscous fluids. Reynolds equation can be derived from Navier - Stokes equation by using the assumptions as mentioned in chapter 2 and neglecting higher order terms of h/r, as shown by [21] and [24]. If inertia terms are not removed, the reduced Navier - Stokes momentum equation in dimensionless form and polar coordinates becomes [24, (6.20)]:

$$\bar{\rho}\left(\bar{\bar{h}}\, R_{e,sq}\, \frac{\partial \bar{u}}{\partial \bar{t}} + R_{e,r}\left[\bar{u}\frac{\partial \bar{u}}{\partial \bar{r}} + \bar{w}\frac{\partial \bar{u}}{\partial \bar{z}}\right]\right) = -\frac{R_{e,r}}{\kappa\, M_a^2}\frac{\partial \bar{p}}{\partial \bar{r}} + \frac{\partial^2 \bar{u}}{\partial \bar{z}^2} \tag{4-13}$$

where $\bar{u}$ is the normalised fluid velocity in r direction and $\bar{w}$ is the normalised fluid velocity in z direction. Time is normalised by dividing through the scaled radial frequency: $t\ [\mathrm{s}] = \bar{t}\ [-]\,/\bar{\bar{h}}\,\omega\ [1/\mathrm{s}]$. M_a is the Mach number and κ the ratio of specific heats.

The terms on the left hand side are the inertia terms. Their relative importance can be judged by the terms with which they are multiplied, which are the reduced Reynolds number:

$$R_{e,r} = \frac{\rho^*\, U\, H^2}{\eta\, R} \tag{4-14}$$

and the squeeze Reynolds number:

$$R_{e,sq} = \frac{\rho^*\, H^2\, \omega}{\eta} \tag{4-15}$$

where density is normalised with ρ^*: $\rho\ [\mathrm{kg/m^3}] = \bar{\rho}\ [-]\ \rho^*\ [\mathrm{kg/m^3}]$. The assumption of neglecting fluid inertia is valid if both Reynolds numbers are much smaller than one.

For a typical air bearing with a radius of 10 mm, a fly height of 10 µm and fed in the middle with a restrictor pressure of 2×10^5 Pa (source pressure 3×10^5 Pa), the average density is around 1.6 kg/m^3. The average velocity is 6 m/s. This gives a reduced Reynolds number of 6×10^{-3}, justifying the assumption that globally speaking the inertia in r direction can be neglected.

If this bearing is vibrating with a frequency of 1 kHz, the squeeze Reynolds number becomes 6×10^{-2}, small enough to disregard the inertial terms. Around 15 kHz, the squeeze Reynolds number becomes 1, and inertia due to the squeeze motion can no longer be neglected.

4-3 Conclusions and outlook

Stiffness and damping of an air film in squeeze motion can be found by linear perturbation of Reynolds equation, as shown in this chapter. The perturbed Reynolds equation is derived and solved using a self developed finite volume method. The solution found by the finite volume model shows correspondence with the COMSOL model. The finite volume method is almost 10 times faster than the COMSOL model, making it suitable for extensive parameter studies. The range of validity of linear perturbation is discussed.

In the next chapter, the developed model will be used to find a low transmissibility air bearing design. First, transmissibility is explained. Then, a study is performed to determine the influence of different design parameters. The effects of adding a vacuum bearing to a thrust bearing is explored, leading to two methods for achieving low stiffness. Last, these designs will be optimized.

5

Low transmissibility bearing design

In this chapter, design of a low transmissibility air bearing will be explored. First, the concept of transmissibility and how it can be influenced is explained. Next, a dimensionless parameter study will be conducted to examine how bearing stiffness can be influenced. The effects of combining thrust with vacuum bearings will be analysed. This will lead to two concepts for a low stiffness air bearing. Both concepts will be thoroughly examined, optimized and compared.

5-1 Transmissibility

The term transmissibility refers to the capability of a system to transfer motion from one body to another. It is defined as the ratio of movements between two bodies. Because transmissibility relates relative movements, it is a useful measure in judging vibration isolation. An ideal vibration isolation system will not transfer any vibrations and have zero transmissibility over the full frequency spectrum. This is not achieved in real systems, but the trend is that lower transmissibility will result in better vibration isolation.

In Figure 5-1, the air bearing system is sketched. The thin film is represented by a spring with stiffness k and a damper with damping c. The counter surface, or floor, moves with distance x_f, causing the bearing to move with distance x_b.

Transmissibility of this system can be shown to be [25, (3.62)]:

$$\frac{x_f}{x_b} = \frac{j\,\omega\,c + k}{-m\,\omega^2 + j\,\omega\,c + k} \tag{5-1}$$

As can be seen from this equation, transmissibility is controlled by three parameters: stiffness, damping and mass. The influence of all three factors will be investigated and compared to a reference: a system with $k = 1 \cdot 10^5\,\mathrm{N/m}$, $c = 3\,\mathrm{N/ms}$ and $m = 1\,\mathrm{kg}$. The eigenfrequency of a mass spring system is given by $\omega_0 = \sqrt{k/m}$, which is 50 Hz for the reference.

This can be seen in Figure 5-2, where a bode plot of the transmissibility is shown, with the magnitude in the top axis and the phase in the lower axis. The reference has been drawn in blue.

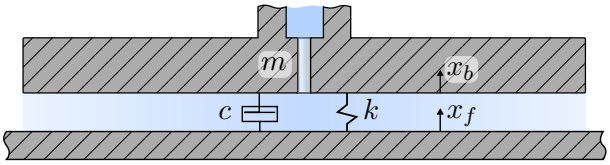

Figure 5-1: Modelling thin film as a spring and damper to find the transmissibility of vibrations from the floor to the bearing

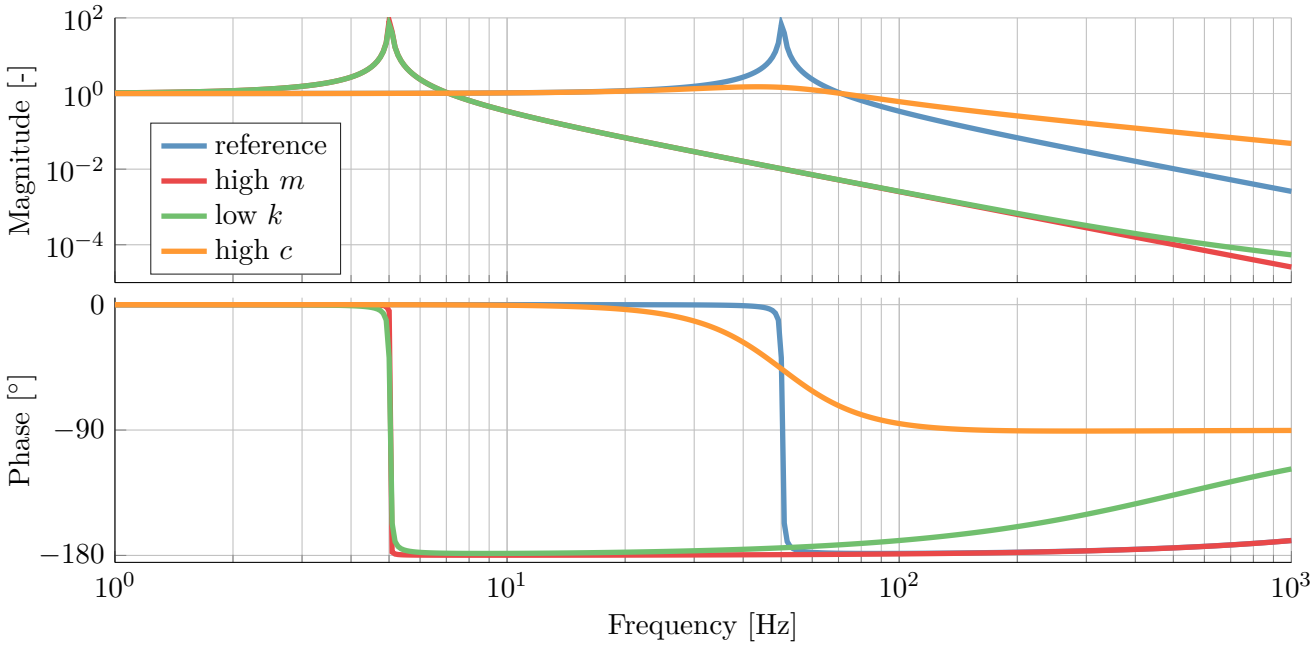

Figure 5-2: Bode plot of transmissibility for four different systems. High mass and low stiffness decrease the eigenfrequency, leading to low transmissibility at high frequencies. High damping reduces eigenfrequency amplitude and couples more strongly at high frequencies.

Increasing mass

By increasing mass with a factor 100, the natural frequency of the system is reduced with a factor 10, from 50 Hz to 5 Hz, as can be seen in Figure 5-2 where the high mass system is drawn in red and is somewhat hidden behind the green line.

For frequencies above the natural frequency, the transmissibility decreases with a slope of -2 (amplitude $\times 10^{-2}$ per decade). A lower natural frequency therefore leads to less throughput of vibration, since transmissibility decrease starts at a lower frequency.

Although the high mass system has better vibration isolation properties, making systems heavier might not be feasible. It will result in a trade off in other system performances. The system is supported on air bearings because it should be able to move parallel to the floor. For example, assume the bearing supports a high speed scan stage. Although increasing the mass has a beneficial effect on vibration isolation, it will also increase the force required to accelerate parallel to the floor, introducing other problems. Decisions concerning the trade off between transmissibility and acceleration can only be made on a system design level, since

it will affect more than only the bearings. Therefore, increasing system mass is not treated further in this thesis as a transmissibility reducing option.

Decreasing stiffness at constant damping ratio

Transmissibility is also influenced by stiffness. In Figure 5-2 the low stiffness case is drawn in green. Stiffness has been reduced with a factor 100, from $1 \times 10^5\,\mathrm{N/m}$ to $1 \times 10^3\,\mathrm{N/m}$. Damping has been changed from $c = 3\,\mathrm{N/ms}$ to $c = 0.3\,\mathrm{N/ms}$, to keep damping ratio ζ constant:

$$\zeta = \frac{c}{2\sqrt{k\,m}} \tag{5-2}$$

at a value of $\zeta = 0.005$. The decrease in stiffness of a factor 100 leads to a decrease in natural frequency with a factor 10. This has an effect equal to increasing the mass: the -2 slope starts at a lower frequency, leading to less vibration throughput at the higher frequencies. In contrast with increasing mass, lowering stiffness has less negative side effects. Therefore, this option is explored in this thesis.

Increasing damping

Finally, damping ratio is changed. The result of increasing damping from $c = 3\,\mathrm{N/ms}$ to $c = 300\,\mathrm{N/ms}$ has been plotted in yellow in Figure 5-2. The resulting damping ratios are $\zeta = 0.005$ and $\zeta = 0.5$, respectively.

Two noticeable effects can be seen in the transmissibility magnitude. First, the peak at the natural frequency has disappeared completely. Second, the decrease in transmissibility after the natural frequency has changed in a -1 (amplitude $\times 10^{-1}$ per decade) slope. More vibrations will be transferred to the bearing at higher frequencies, because the damper is coupling the floor and bearing more strongly at these frequencies.

The phase of the transmissibility also shows two noticeable differences. The phase at the natural frequency now changes more smoothly and decreases to $-90°$ instead of $-180°$. This behaviour is typical of a damper.

A closer look at the low stiffness case in green shows that the phase at high frequencies is starting to increase, and the magnitude is transferring from a -2 line to a -1 line. This is also caused by damping.

The decrease in resonance peak magnitude is beneficial, but stronger coupling at high frequencies is not. Therefore, the properties of a vibration isolating air bearing to optimize are low stiffness and low damping. The resonance peak should be dealt with differently, for example with tuned mass-spring-damper, as discussed in [25].

5-2 Parameter study

Low transmissibility can be achieved with low bearing stiffness. To design a low stiffness bearing, first some insight in the effect of design parameters is required. Therefore, a parameter study is conducted in this section.

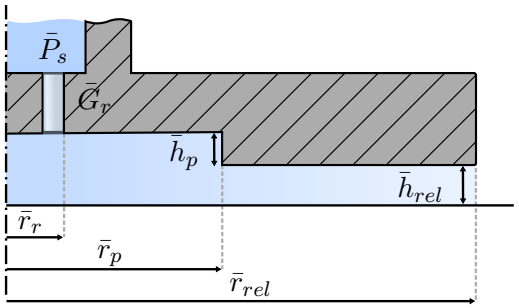

Figure 5-3: Declaration of dimensionless geometry parameters for the air bearing model, drawn in axisymmetric view. To allow height offsets and different radii between multiple dimensionless bearings, the relative fly height and outer radius are defined.

First, the benefits of doing a dimensionless study are discussed and design parameters are set up. Next, the effect of these parameters on load capacity, stiffness and damping is treated.

5-2-1 Dimensionless analysis

The finite volume method models developed in chapter 3 and chapter 4 are in dimensionless form. This has two clear advantages, but also requires a conversion to dimensioned values.

First, by using dimensionless equations, the numerical accuracy is increased, as discussed in subsection 3-4-3.

Second, the solutions found in a dimensionless solution are valid for every bearing that has the same normalised geometry: the solution can be scaled to a certain dimension to describe a dimensioned design. This considerably simplifies the design process. One dimensionless design with advantageous properties, like low stiffness, can be scaled to fit multiple dimensioned designs with different load capacities.

Dimensionless design parameters

The set of parameters for this dimensionless axisymmetric air bearing design is reduced compared to the dimensioned design. Because the outer radius and fly height are normalised, they can be removed from the design parameters for a single bearing. However, because the effect of combining two bearings is studied in a coming section, a relative fly height and radius is added. For a study with two bearings, this leads to 12 design parameters in total: 2 times 3 geometry parameters, 2 feed pressures, 2 restrictor conductivities and 2 relative geometry parameters.

5-2-2 Influence of design parameters

In this section, the effect of changing design parameters is explored. All changed characteristics are compared to a reference design, a bearing without a pocket and with the air feed located in the middle. The parameters of all modelled designs are listed in Table 5-1. All plots that do not have dimensionless fly height $\bar{h}$ on the x axis are drawn at $\bar{h} = 1$, unless stated otherwise.

Table 5-1: Design parameters for all examined models. Parameters that did not change with respect to the reference are noted with a "-".

Parameter	Reference	$\bar{r}_r = 0.3$	$\bar{r}_p = 0.3$	$\bar{G}_r = 3$	$\bar{G}_r = 1/3$	$\bar{P}_s = 6$	$\bar{P}_s = 1.5$
$\bar{r}_p$	0	-	0.3	-	-	-	-
$\bar{h}_p$	0	-	10	-	-	-	-
$\bar{r}_r$	0.01	0.3	-	-	-	-	-
$\bar{P}_s$	3	-	-	-	-	6	1.5
$\bar{G}_r$	1	-	-	3	1/3	-	-

Influence of restrictor radius and pocket

First, the effect of placing the restrictor off centre is studied. Because adding pocket has a similar effect, this is also treated here. Results are plotted in Figure 5-4.

The top left axis shows the pressure distribution versus the radius. For radii lower than the restrictor or pocket radius, pressure is constant. High film height in the pocket results in an negligible resistance; there is virtually no pressure drop in the pocket. Therefore, adding a pocket has the same effect as increasing the restrictor radius and the off centre air feed creates a 'virtual pocket'.

The thin film from restrictor (or pocket) to the outer edge is shorter compared to the reference case. Since this is the only part with significant resistance, the total resistance is lower. This results in a lower restrictor pressure compared to the reference case, from $\bar{P}_r = 2.8$ for the reference case to $\bar{P}_r = 2.3$.

Although the restrictor pressure is lower for both bearings, their load capacity is considerably higher than the reference case. This can be seen in the lower left figure. Because the pressure is higher for essentially the total radius, the load capacity is increased.

The stiffness and damping versus the frequency at $\bar{h} = 1$ are plotted in the right column. Before examining the effect of different parameters, the overall behaviour is explained, as displayed by the reference bearing.

At low frequencies, squeeze motion results in damping. A change in fly height forces fluid in and out at a flow rate proportional to the relative velocity of the bearing. Resistance to this flow, which is also proportional to the flow rate, creates a reaction force on the bearing. This force is thus proportional to, and in phase with, velocity and therefore identified as damping.

At higher frequencies, the fluid is no longer forced in and out of the air gap by a change in fly height, but it is compressed. The resulting force on the bearing becomes proportional to displacement instead of velocity. The film now acts as a spring instead of a damper. [26].

Both decreasing damping and increasing stiffness can be seen in the graphs. The stiffness is not zero for low frequencies due to the static behaviour of the bearing. This can be seen in the load capacity - fly height diagram on the bottom left, which as a non zero slope at $\bar{h} = 1$.

Both non reference bearings show equal and increased stiffness at low frequencies compared to the reference. This can also be seen from the $\bar{W}$- $\bar{h}$ graph, where the derivative at $\bar{h} = 1$ is larger than that of the reference bearing. For higher frequencies, the pocket shows a different stiffness behaviour than the increased radius, caused by a difference in film volume.

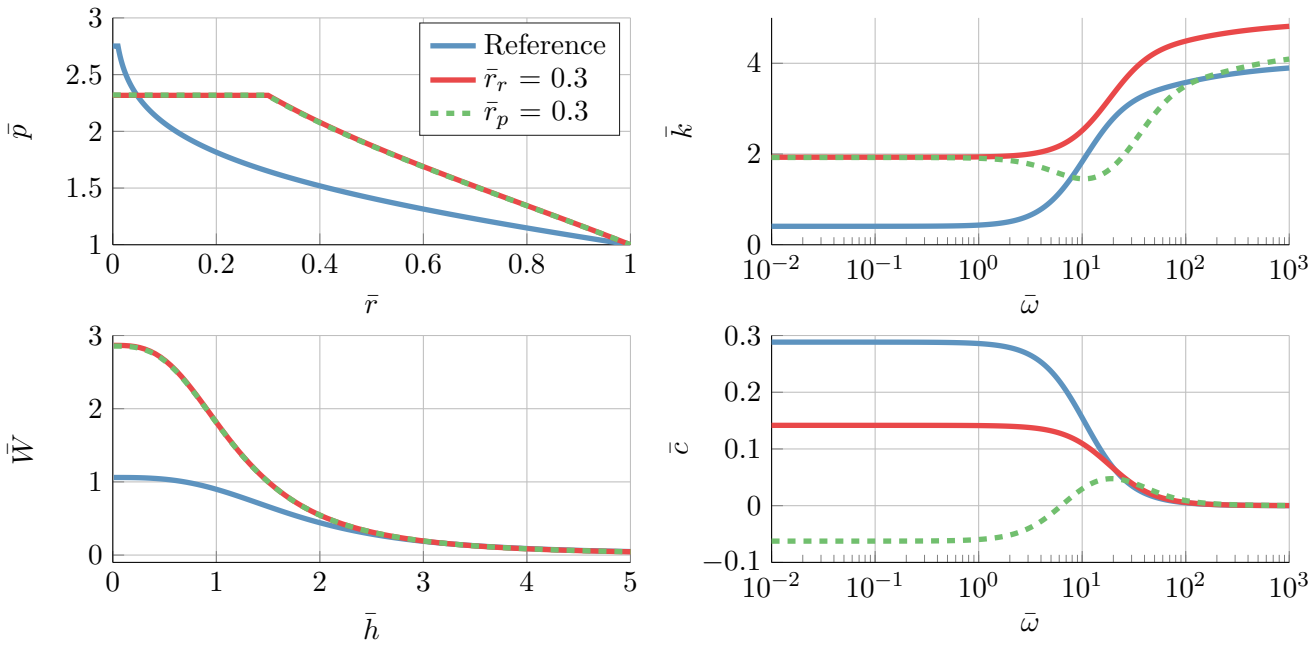

Figure 5-4: Characteristics of a bearing with feed at $\bar{r} = 0.3$ and with a pocket with height $\bar{h}_p = 10$ at $\bar{r}_p = 0.3$. Statically, a pocket and feed radius have the same effect, dynamically they do not. The bearing with pocket is dynamically unstable, because damping is negative at low frequencies.

A difference in damping is also observed, shown in the bottom right. Contrary to the reference and off centre restrictor bearing, damping for the pocket bearing starts at a negative value. This means that the bearing is dynamically unstable. This instability is a well known phenomena in air bearing design and is called 'pneumatic hammer'. It is caused by having significant volumes in the thin film, downstream of the restrictor. It will be treated in more detail in section 6-2.

Influence of restrictor conductivity

A change in conductivity will result in a change of stiffness. This can be seen in Figure 5-5, where the results for increased and decreased conductivities are plotted. The most pronounced effect is seen in the $\bar{W}$- $\bar{h}$ plot, on the bottom left. By increasing the conductivity, stiffness is decreased and vice versa. This is also reflected in the low frequency stiffness, which is higher for a lower conductivity.

This effect can be understood by analysing the bearing as a system of two resistances in series, namely the restrictor and the thin film. The load capacity is proportional to the ratio of thin film resistance over total resistance: $\bar{W} \sim R_{tf}/(R_r + R_{tf})$. Since the geometries for the three compared bearings in this study is equal, their thin film resistance is equal at equal fly height.

Therefore, a high restrictor resistance (low $\bar{G}_r$) will give a lower load capacity at a particular fly height. But since the maximum load capacity is only dependent on the thin film geometry (for low $\bar{h}$: $R_{tf} >> R_r$), and the geometry is equal, the higher resistance will result in a faster decrease of $\bar{W}$ with increasing $\bar{h}$, resulting in a higher stiffness.

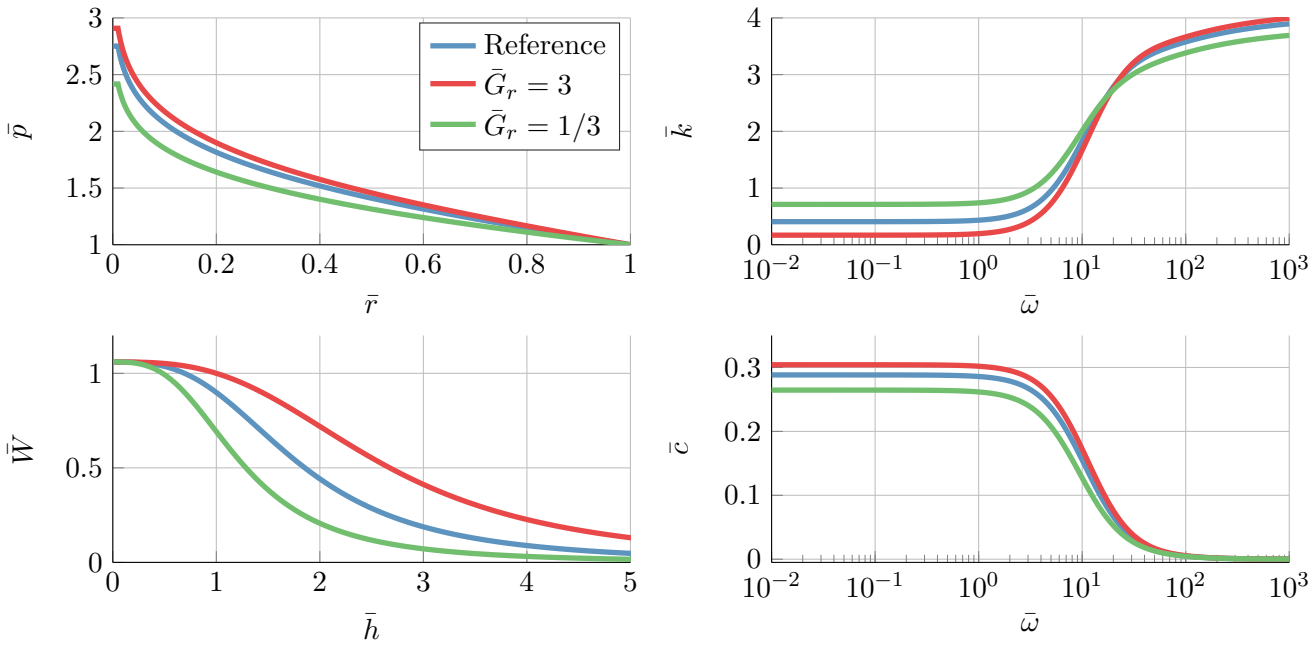

Figure 5-5: Characteristics of bearings with $\bar{G}_r = 1$, $\bar{G}_r = 3$ and $\bar{G}_r = 1/3$. Increasing conductivity decreases stiffness.

Decreasing stiffness by increasing $\bar{G}_r$ looks promising for a low transmissibility design. For an infinitely high $\bar{G}_r$ the system indeed has no stiffness, but also is unstable. This results in the bearing as shown in Figure 3-1, with a constant $\bar{W}$, independent of $\bar{h}$.

Influence of increasing the source pressure

In Figure 5-6, the results for an increased and decreased source pressure are drawn. Increasing the source pressure raises the maximum load capacity. The higher maximum load also leads to a higher stiffness, since the load capacity still declines over almost the same range in fly height but starts at a higher value. Higher source pressure increases stiffness over the whole frequency spectrum. It has no pronounced effect on damping.

Influence of relative bearing height and radius

As can be seen in the left graph of Figure 5-7, increasing the relative fly height with 0.5 has the effect of shifting the $\bar{W} - \bar{h}$ curve to the left with 0.5. Decreasing the relative fly height with 0.5 will shift the curve and cause the model to stop at $\bar{h} = 0.5$, since at that height the bearing will make contact. The $\bar{p} - \bar{r}$, $\bar{k} - \bar{\omega}$ and $\bar{c} - \bar{\omega}$ plots, are identical for all three bearings, only the frequency is shifted with a factor $\bar{h}^2_{rel}$. Therefore, they are omitted.

On the right side of Figure 5-7, the effect of a relative change in radius is plotted. A larger radius will increase the load capacity. The stiffness and damping magnitude is scaled with $\bar{r}^2_{rel}$, the frequency with $1/\bar{r}^2_{rel}$.

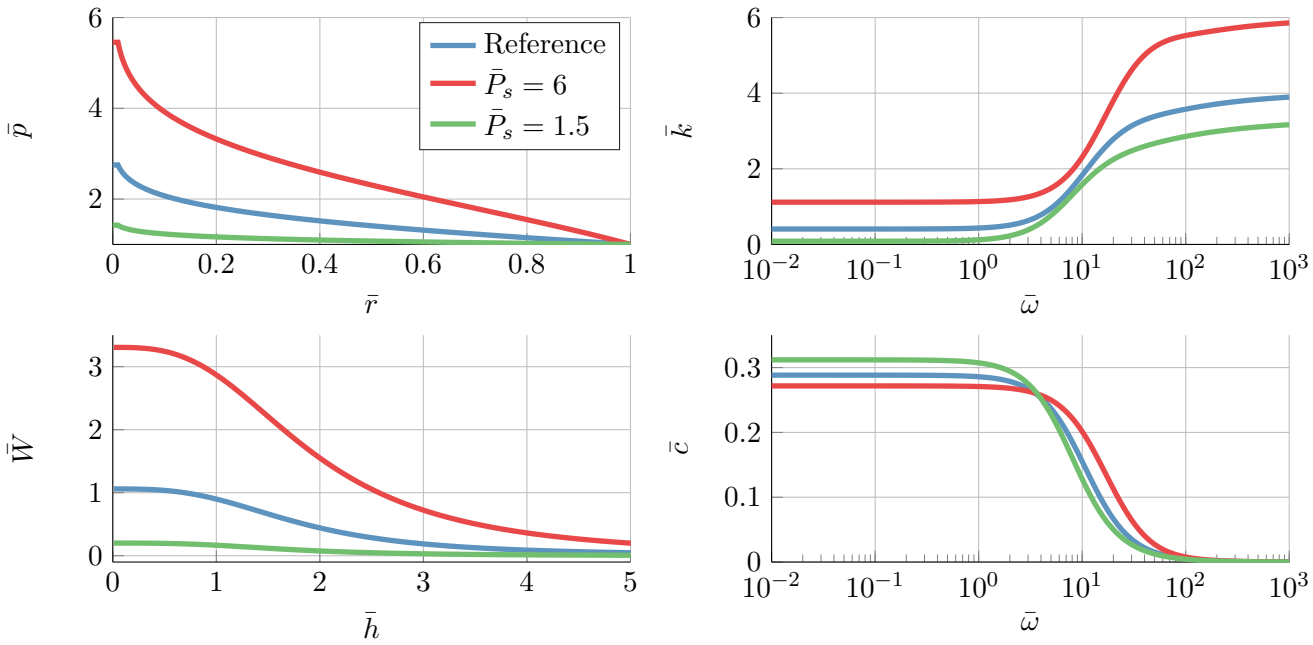

Figure 5-6: Characteristics of a bearings with $\bar{P}_s = 6$ and $\bar{P}_s = 1.5$. Increasing source pressure results in a higher maximum load capacity and increased stiffness.

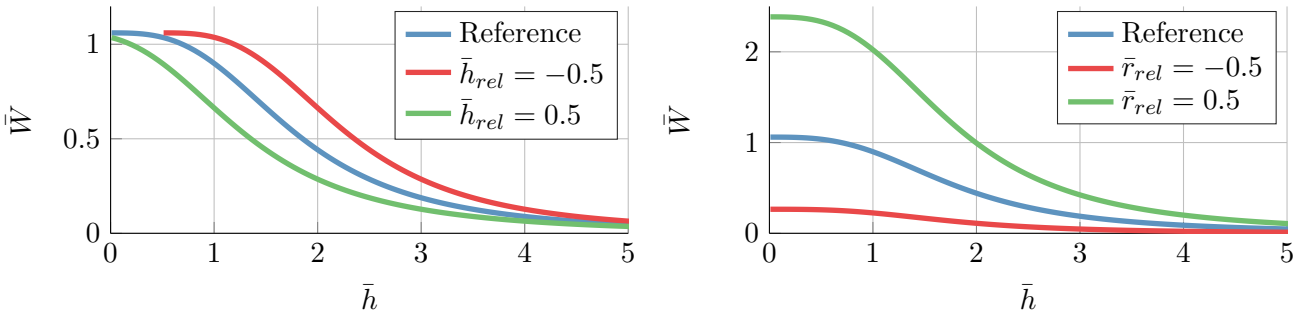

Figure 5-7: Load capacity versus fly height of a bearings with a different relative fly height (left) and radius (right). Increasing relative fly height shifts the $\bar{W} - \bar{h}$ line to the left. Increasing relative radius raises load capacity.

5-3 Combing thrust and vacuum bearings

With the influence of design parameters on the behaviour of a single bearing discussed, in this section a vacuum bearing is added to the thrust bearing. This is commonly used to increase the total bearing stiffness, as discussed in chapter 1. This mechanism will be shown in the next subsection. The addition of a vacuum bearing also creates an opportunity for a stable low stiffness design, as will be treated subsequently.

The source pressure of a vacuum bearing is lower than ambient pressure. This gives a vacuum bearing a negative load capacity and negative stiffness. The design parameters, as discussed in the last section, effect a vacuum bearing in a similar way as it effects thrust bearings. Load capacity can be changed with (virtual) pockets and conductivity influences stiffness.

Although stiffness is negative for feed pressures < 1, damping is not. It shows similar behaviour as damping in thrust bearings.

5-3-1 Vacuum pre-loading

As discussed in chapter 1, air bearings are usually optimized for high stiffness. While maintaining equal load capacity, bearing stiffness can be enhanced by increasing source pressure and pre-loading, often done using vacuum bearings.

The function of the vacuum bearing is to pre-load the thrust bearing. The increased load capacity caused by the high feed pressure is countered by the negative load capacity of the vacuum bearing. Vacuum bearings are implemented such that they exert a constant force, thus with zero stiffness. Therefore, the increased stiffness of the high source pressure now occurs at the same load capacity and fly height as the default source pressure without pre-load.

To ensure a constant negative force by the vacuum bearing, in actual air bearings the vacuum film is significantly higher than the pressurized film. Also, the vacuum flow is only restricted by mass flow limits in the vacuum source. Because this behaviour is not captured by the model, it is illustrated by using a equal film height, high restrictor conductivity vacuum air bearing.

Increased stiffness is illustrated in Figure 5-8. In this $\bar{W} - \bar{h}$ graph, the reference bearing is compared to a increased source pressure and vacuum pre-loaded bearing. At the operating point of $\bar{h} = 1.6$, stiffness of the pre-loaded bearing is significantly higher than the reference case, while having the same load capacity.

5-3-2 Effect of negative stiffness on bearing stability

Vacuum bearings used for pre-loading exert a fly height independent and thus constant force. This force can made fly height dependent by having the vacuum surface at equal height to the pressurized surface and restricting vacuum flow. This gives the vacuum bearing stiffness, which is negative because the vacuum force is negative and increasing to zero. The total system stiffness is the sum of thrust and vacuum stiffness. Therefore, a vacuum bearing can be used to reduce total stiffness. However, this will not lead to a stable, low stiffness operating point, as will be shown.

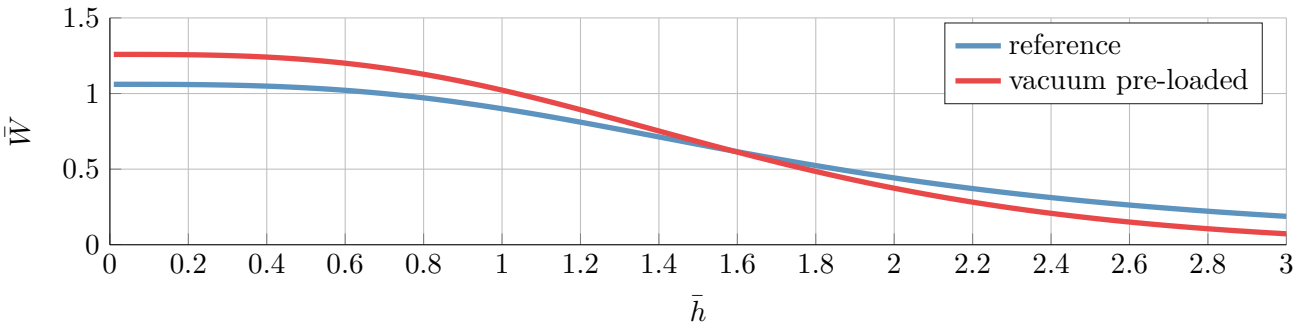

Figure 5-8: Load capacity for reference bearing and vacuum pre-loaded bearing. The increased load capacity is countered by the pre-load, resulting in higher stiffness.

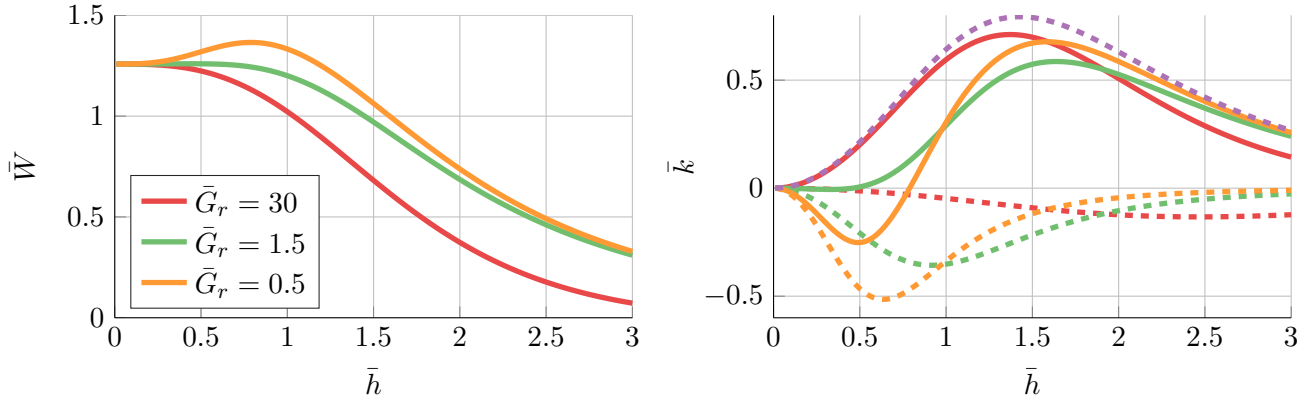

Figure 5-9: Effect of increasing negative stiffness in the vacuum pre-loaded system. The solid red line, $\bar{G}_r = 30$, is the pre-loaded system as drawn in Figure 5-8. In the right axis, the stiffness versus fly height has been plotted. The stiffness of the thrust bearing is drawn with a purple dashed line. Other dashed lines, with negative stiffness values, are vacuum stiffnesses at different conductivities. Combined vacuum and pressurized load capacities and stiffnesses are drawn with solid lines.

To illustrate this, the vacuum conductivity of the system from the previous subsection, which has surfaces at equal heights, is decreased. The results have been plotted in Figure 5-9.

First examine the red line, which is the pre-loaded system from Figure 5-8. The total stiffness, drawn with a solid line in the right graph, is the sum of the thrust (purple dashed) and vacuum (red dashed) stiffness. The vacuum stiffness is low and almost constant, having little effect on the total stiffness. If conductivity is reduced to $\bar{G}_r = 1.5$, stiffnesses balance. The solid green line has low stiffness up to $\bar{h} = 0.5$.

If the conductivity is reduced even further, as drawn in yellow, a zero stiffness point appears. Left of this point is a region with negative stiffness, making this zero stiffness point unstable. If the bearing is operating at the zero stiffness point and a small disturbance decreases the fly height, the vacuum part will pull harder than the thrust part can push. The bearing snaps in and makes contact, which is undesirable.

To create a stable low stiffness point, the $\bar{W} - \bar{h}$ curve should be *monotonically decreasing*. The low stiffness point should not cross the $\bar{k} = 0$ line, but at best be tangent to it.

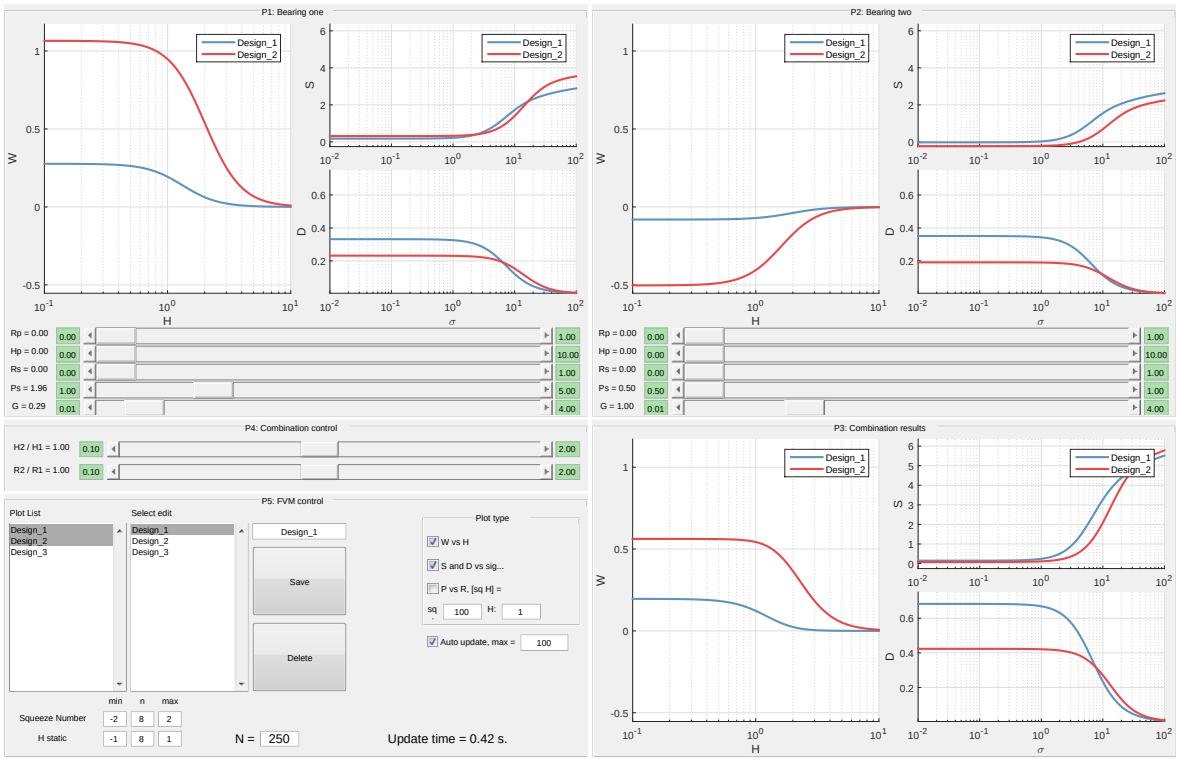

Figure 5-10: Screen capture of the graphical user interface. Influence of design parameters can be tested, combination of bearings assessed and different combinations compared.

The system with $\bar{G}_r = 1.5$ complies to these rules, but is also not a feasible vibration isolator. The low stiffness region occurs at maximum load capacity. If the bearing operates at this point, the fly height could reduce to $\bar{h} = 0$ and the bearing could make contact.

This sets a second rule. The low stiffness point should not be at the maximum load capacity, but should be a decrease in the $\bar{k} - \bar{h}$ curve, in between two areas with positive stiffness.

By only changing the vacuum conductivity and vacuum restrictor radius, and thus influencing the negative load capacity and stiffness, no designs complying to both rules have been found. If the vacuum stiffness is equalized to the bearing stiffness, it would always resemble the green line in Figure 5-9. The stiffness decrease of the vacuum starts at the same fly height as the increase of the thrust bearing. A different design strategy is required to find an operable low stiffness working point.

To simplify the design process and create insight in the effects of parameters, the 'air bearing design tool' has been programmed. This is a user interface that uses sliders to change the geometries of a thrust and vacuum bearing, and in real time plot the corresponding curves, as can be seen in Figure 5-10. Details of this tool can be found in Appendix C.

5-4 Low stiffness air bearing design

As seen in the last section, decreasing vacuum bearing conductivity to balance negative stiffness with the thrust pad's positive stiffness does not lead to an operable low stiffness working

Table 5-2: Design parameters for vacuum bearing as drawn in Figure 5-11

Parameter	Design 1	Design 2	Design 3	Design 4
$\bar{h}_{rel}$	-0.3	-0.5	-0.7	-0.9
$\bar{r}_r$	0.28	0.33	0.33	0.31
$\bar{G}_r$	1	-	-	-
$\bar{P}_s$	0.5	-	-	-

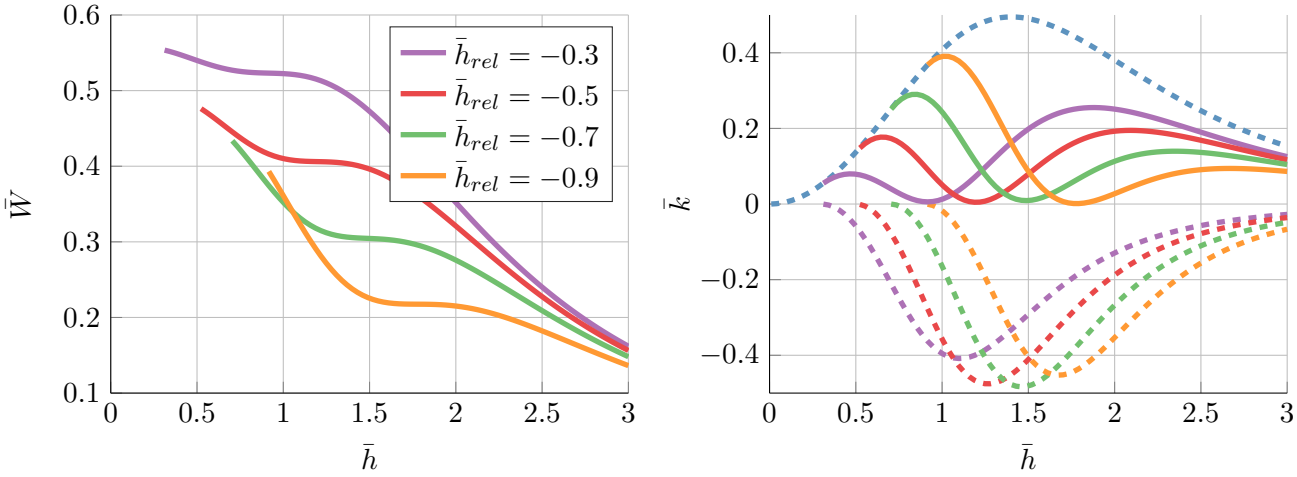

Figure 5-11: Load capacity and stiffness diagrams for low stiffness designs. The blue dashed line in the right graph is the reference bearing stiffness. The dashed lines in other colours are the stiffnesses of the vacuum bearings. The combined load capacity and stiffness are plotted in solid lines.

point. If stiffnesses are balanced, the low stiffness point will occur at maximum load capacity. However, by changing the fly height at which the negative stiffness is maximum, a stable design and operable working point can be achieved. Alternatively, using the air bearing design tool, another promising design was found. Both are described in the next subsection.

5-4-1 Low stiffness by height difference - concept one

In section 5-2, a decrease in relative fly height is shown to shift the $\bar{W} - \bar{h}$ curve to the right. If the vacuum bearing is given a height offset, its stiffness will start to increase for higher fly heights. This solves the problem that stiffnesses can only be made to balance at low fly heights, close to the maximum load capacity.

Stable designs can be achieved with a negative relative fly height. The vacuum restrictor radius needs to be changed for different height offsets to balance the stiffnesses. Some results, combining the reference bearing with a vacuum bearing, are plotted in Figure 5-11. The parameters are listed in Table 5-2.

The combined load capacity versus fly height curve is drawn on the left. The stiffness versus fly height is drawn on the right. The stiffness of the reference bearing is drawn with a blue dashed line. This bearing is combined with 4 different vacuum bearings, leading to 4 low

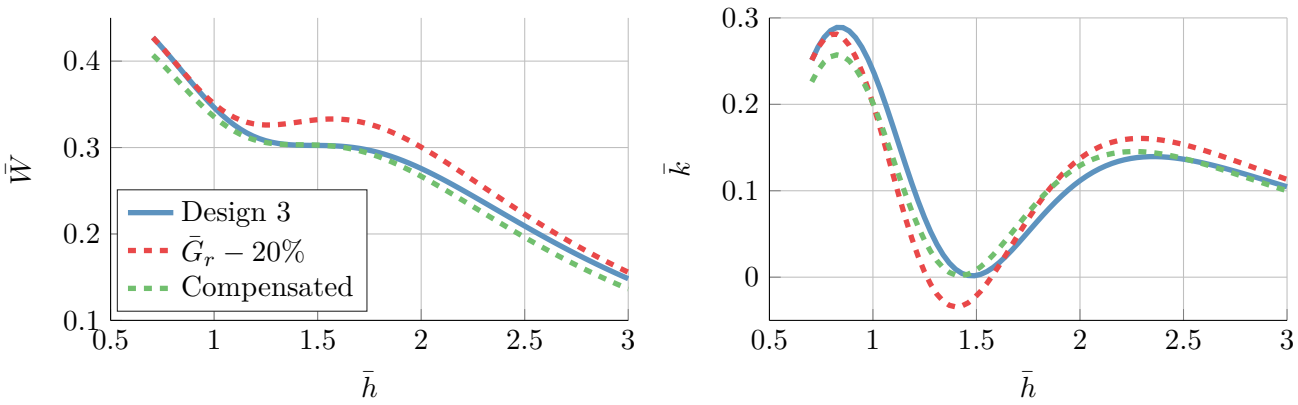

Figure 5-12: Load capacity and stiffness diagrams for low stiffness designs with 20% error in $\bar{G}_r$. The error is compensated by tuning both supply pressures.

stiffness systems. Each vacuum bearing has a different height offset. The vacuum stiffnesses are drawn in dashed lines, all are negative. The combined stiffnesses are plotted in solid lines, where the colour of the combined (solid) line corresponds to the colour of the vacuum (dashed) line.

For an increasing height difference, the low stiffness point occurs at lower fly heights. It determines the balance of load capacity before and after the low stiffness point. The trade off is in the load capacity at the low stiffness point. A lower relative fly height difference will lead to a higher load capacity at the low stiffness point, but less margin for unexpected changes in load. Designs using this method of height offset to create a low stiffness point are hereby referenced as concept one.

Compensation of manufacturing uncertainties

When a design is manufactured, parameters have some degree of uncertainty. Some will have more relative uncertainty than others, and therefore influence expected performance more.

The average fly height of an air bearing is 10 µm, thus the height offset is in the order of µm. This is 4 orders of magnitude smaller than the radius, which is typically in the order of 10 mm. Therefore the height offset can be expected to have relative high uncertainty. Restrictor conductivity also has a high manufacturing uncertainty, as will be shown in chapter 6.

A change of 20% in both $\bar{G}_r$ and $\bar{h}_{rel}$ shows around a 10% change in load capacity at the low stiffness operating point. Especially a change in $\bar{G}_r$ has a negative effect because it will cause the vacuum stiffness to no longer balance the thrust stiffness.

However, both source pressures can be tuned in operation. By changing source pressures, uncertainty in manufacturing can be compensated.

This is shown in Figure 5-12, where the vacuum restrictor conductivity of design 3 from the previous subsection is lowered with 20%. This increases vacuum stiffness, leading to an unstable point around $\bar{h} = 1.4$. If the thrust pressure is lowered to 2.82 and the vacuum pressure increased to 0.59, low stiffness can still be achieved at the anticipated load capacity. Uncertainty in can $\bar{h}_{rel}$ can be compensated with a similar strategy.

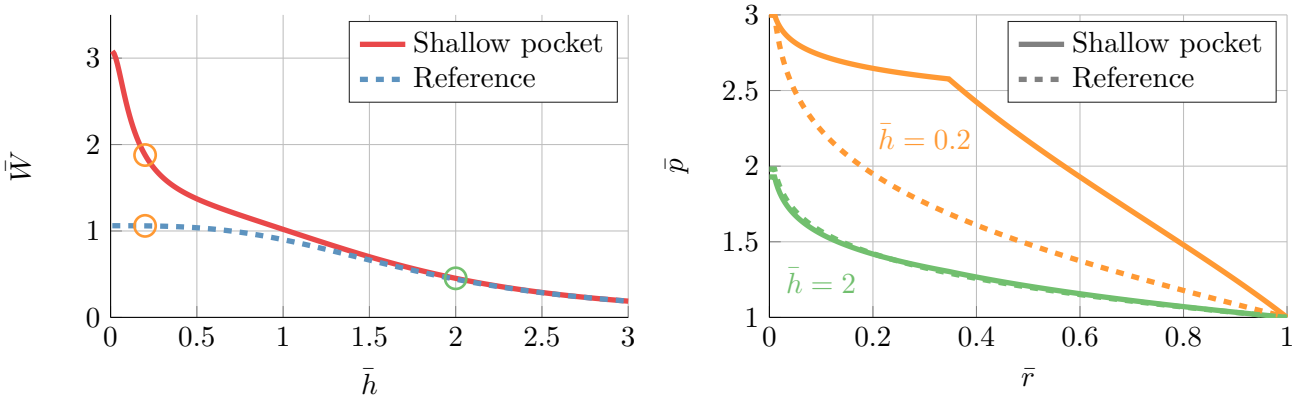

Figure 5-13: Load capacity and pressure of a shallow pocket bearing. At low fly heights, the shallow pocket has a significant effect on load capacity. At higher fly heights, the effect of the pocket is negligible.

5-4-2 Low stiffness by shallow pocket - concept two

By manipulating the user interface as described in Appendix C, an alternative low stiffness design has been found. This concept uses a shallow pocket, which influences low fly height stiffness. First, the mechanism resulting in high stiffness is explained. Thereafter, it will be used to find an alternative low stiffness design.

Influence of a shallow pocket

On the left of Figure 5-13, the $\bar{W} - \bar{h}$ of a bearing with a pocket depth of 0.1 is drawn. For $\bar{h} > 1$, the bearing shows almost identical behaviour to the reference bearing, but for lower fly heights, both load capacity and stiffness increases significantly.

The mechanism driving this effect can be understood by examining the right graph, where film pressures for $\bar{h} = 2$ and $\bar{h} = 0.2$ have been drawn.

For $\bar{h} = 2$, the film pressures are almost identical. The relative height increase in the pocket is only 5% of the total film height and has a negligible effect on the resistance of the thin film.

For lower fly heights, the relative height increase becomes significant. At $\bar{h} = 0.2$, the film in the pocket is 50% higher than the film in the edge. The pocket resistance is significantly lower than that of the edge, increasing the load capacity and stiffness.

This leads to a bearing with a high stiffness at low fly heights and thus a lower, more constant stiffness at moderate fly heights. By combining this bearing with a vacuum bearing, a low stiffness operating point can be created.

Combining a shallow pocket with a vacuum bearing

High stiffness for low fly heights circumvents the problem as stated in subsection 5-3-2, where vacuum stiffness (without offset) for low fly heights would always lead to a low stiffness point at maximum load capacity. The shallow pocket thrust stiffness is no longer fully balanced by

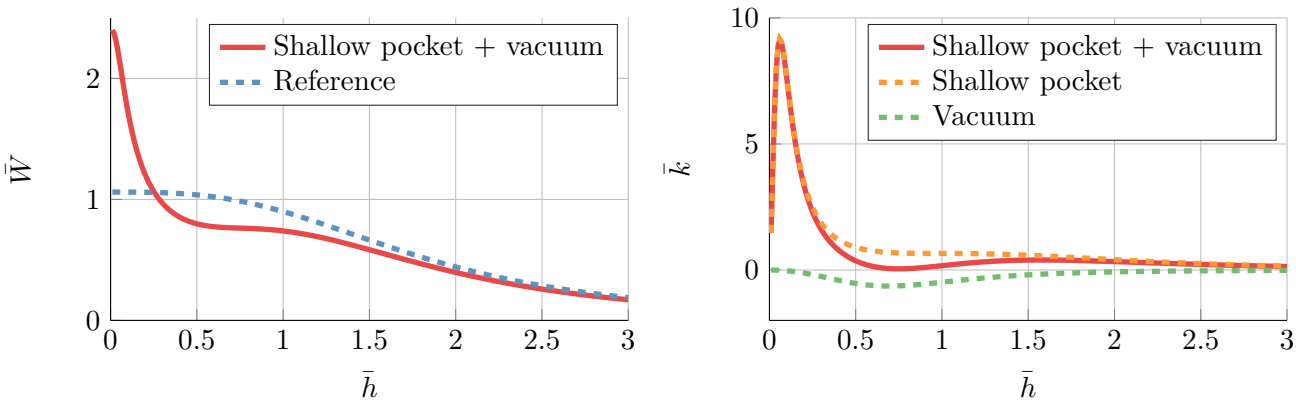

Figure 5-14: Load capacity and stiffness diagram of a shallow pocket low stiffness design. High stiffness at low fly heights caused by a shallow pocket are no longer balanced by a vacuum bearing without height offset.

Table 5-3: Parameters for shallow pocket low stiffness design

Parameter	Shallow pocket	Vacuum
$\bar{P}_s$	3	0.5
$\bar{r}_r$	0.01	0.42
$\bar{r}_p$	0.35	0
$\bar{h}_p$	0.1	0

the vacuum stiffness for all low fly heights. Thus, a stable and workable low stiffness design can be achieved with a thrust and vacuum bearing without a relative height offset.

An example of such a design is shown in Figure 5-14. Design parameters are listed in Table 5-3. High stiffness at low fly heights is not fully compensated by the vacuum stiffness, leading to a stable low stiffness operating point at $\bar{h} = 0.6$, as can be seen in the right graph. Designs using a shallow pocket to create a low stiffness operating point will be referenced as concept two.

Compensation of manufacturing uncertainties

Similarly as for the concept 1, an uncertainty analysis is done for concept two to show that manufacturing uncertainties can be compensated by tuning source pressures.

For a shallow pocket design, following the same reasoning as in the previous uncertainty analysis, the pocket depth and conductivity are subject to relatively high uncertainties. As shown in Figure 5-15, an increase in pocket depth of 50% will lead to a higher stiffness at the operating point. By decreasing the vacuum source pressure, the stiffness at the operating point reduces to the same level as in the intended design. The change in load capacity is dealt with by a slight increase in thrust source pressure.

This example illustrates that relatively high design uncertainty can be dealt with by tuning source pressures.

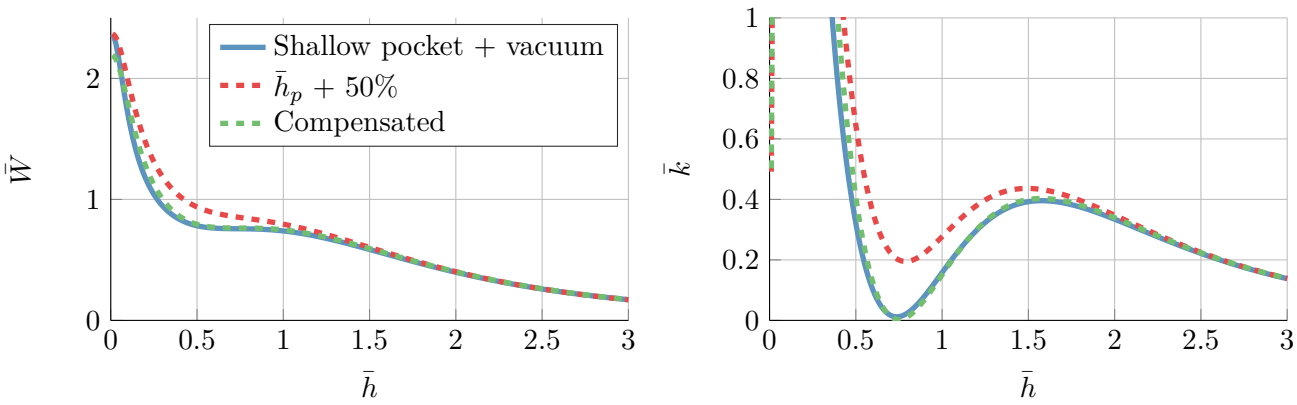

Figure 5-15: Load capacity and stiffness diagram of a shallow pocket with a 50% deviation in pocket depth. By compensating both supply pressures, manufacturing errors can be negated.

5-4-3 Design optimisation

In the previous sections, two concepts for low stiffness bearings have been discussed. The presented designs are just examples of the working principle. When designing a low transmissibility bearing, some extra requirements can be considered to improve the system's performance. This will be treated in this subsection.

The designs in this subsection are optimised manually, by examining load capacity and stiffness characteristics, and not using optimisation algorithms. Therefore, the objective and constraints are not written in equations, as is modus operandi for algorithmic optimisations, but explained in words. Because the thought process for a manual optimisation is similar to that of setting up an algorithmic optimisation, the structure of an algorithmic optimisation is used. First the objective to be optimised is defined. Then, constraints to which the design should comply are discussed.

Objective

For a vibration isolation system, a large low stiffness range is beneficial. If vibration amplitudes exceed the range of low stiffness, transmissibility will increase and vibrations will be passed through. Therefore, the range of low stiffness should be maximised.

This range could be measured in two ways. First, a boundary value $\bar{k}_{min}$ can be defined. The ratio of heights for which the system stiffness crosses the boundary stiffness can be used as an objective. However, this requires model evaluations for a range of fly heights. This is no problem when doing a manual optimization since the model is fast and bearing characteristics will be examined for a range of fly heights anyway.

When an algorithm is used for optimisation, an alternative, possibly more efficient, approach is possible. The stiffness in the operating point should be a minimum. Thus, the derivative of the stiffness is crossing zero. The angle at which it crosses determines the rate of change of the stiffness. A more shallow change in stiffness derivative, so a smaller angle, leads to a larger low stiffness fly height range. Since the angle of the change in stiffness is the second derivative of the stiffness, this metric should be minimized at the operating point.

A secondary design objective could be to increase the load capacity at the operating point. This leads to smaller bearings for equal load capacities.

Constraints

Rules for stable designs are optimization constraints. They are covered in the previous sections, and therefore only shortly summarized here. For a stable bearing design, the load capacity should be monotonically decreasing. The operating point should also have some stiffness for lower and higher fly heights to ensure that an unexpected load increase does not cause contact.

The design parameters are also constrained. Some ranges have to be chosen such that they are reasonable from an engineering point of view. These ranges are debatable. For instance, the maximum source pressure for this optimization is set at three, but six might as well have been chosen.

Since deep pockets will lead to pneumatic hammer, pockets will only be used for the shallow pocket effect. Only virtual pockets will be used to increase load capacity and stiffness.

Optimization results and comparison

The manually optimized parameters are listed in Table 5-4 and the resulting stiffness and load capacities are plotted in Figure 5-16. The design scores, defined as the ratio of the highest fly height with stiffness below $\bar{k}_{min}$ over the lowest can be found in Table 5-5. $\bar{k}_{min}$ is set to 0.05.

Optimized concept one has increased load capacity and increased low stiffness range. By raising the height offset, the vacuum stiffness starts acting at a higher fly height. Both conductivities are increased to lower stiffness over a wider range of fly heights. The source radius is not put off centre, because the increase in stiffness this provides has to be balanced with the vacuum bearing. This did not lead to an increase in load capacity.

Optimized concept two is more balanced in pre and post operating point load capacity. By increasing thrust resistor radius, maximum load capacity is increased. By lowering pocket radius, pre working point stiffness is sacrificed for post working point stiffness. The increased load capacity comes at the cost of slightly smaller low stiffness range.

Concept one shows a higher score, so it has a larger low stiffness range. The load capacity for bearings with the same size, however, is less than half that of the shallow pocket design.

Table 5-4: Manually optimized parameters

	Concept one		**Concept two**	
Parameter	Thrust	Vacuum	Thrust	Vacuum
$\bar{G}_r$	3	2	1	1
$\bar{P}_s$	3	0.5	3	0.5
$\bar{r}_r$	0.01	0.29	0.05	0.528
$\bar{r}_p$	-	-	0.25	-
$\bar{h}_p$	-	-	0.1	-
$\bar{h}_{rel}$	1	-0.9	1	1

Table 5-5: Optimization scores

Model	Score
Concept one example	1.35
Concept one optimized	1.42
Concept two example	1.36
Concept two optimized	1.32

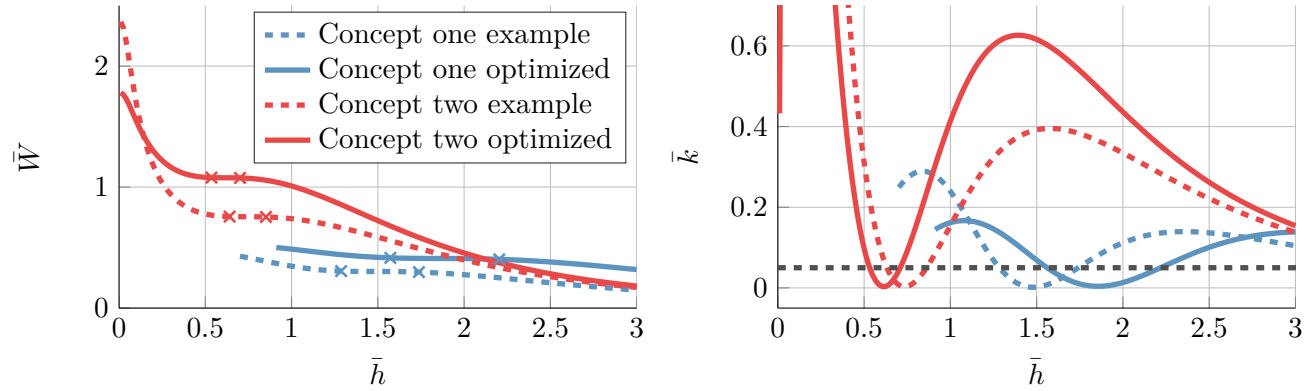

Figure 5-16: Load capacity and stiffness diagrams for optimized low stiffness bearings. The grey dashes line in the stiffness diagram marks the low stiffness range. The crosses in the load capacity diagram mark the points where the designs cross the low stiffness range.

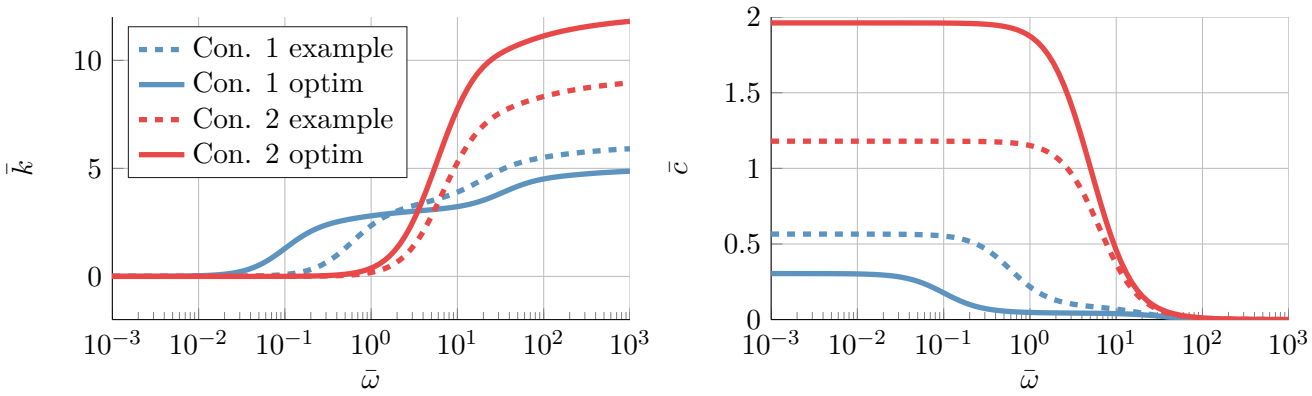

Figure 5-17: Stiffness and damping in the frequency domain for both optimized bearings. All models are run at the low stiffness fly height of that particular bearing.

Depending on the dimensioned design requirements and manufacturability, a choice has to be made for one both concepts. There is no clear best design.

Although the optimized results look promising, there is no doubt that an algorithmic optimization would give even better results. Especially a method that is good finding the global minimum, like a genetic algorithm, could yield interesting combinations of parameters. This is left as a recommendation.

Dynamic properties of optimized design

In Figure 5-17, stiffness and damping versus frequency for both concepts are plotted. The frequency models are evaluated at the operating point fly height. Therefore the low frequency stiffness is close to zero for all models.

Stiffness for concept one increases at lower frequencies than it does for concept two, because a negative height difference shifts the frequency at which the stiffness increase begins to lower frequencies. Damping also shifts to lower frequencies. Concept one has a lower dimensionless

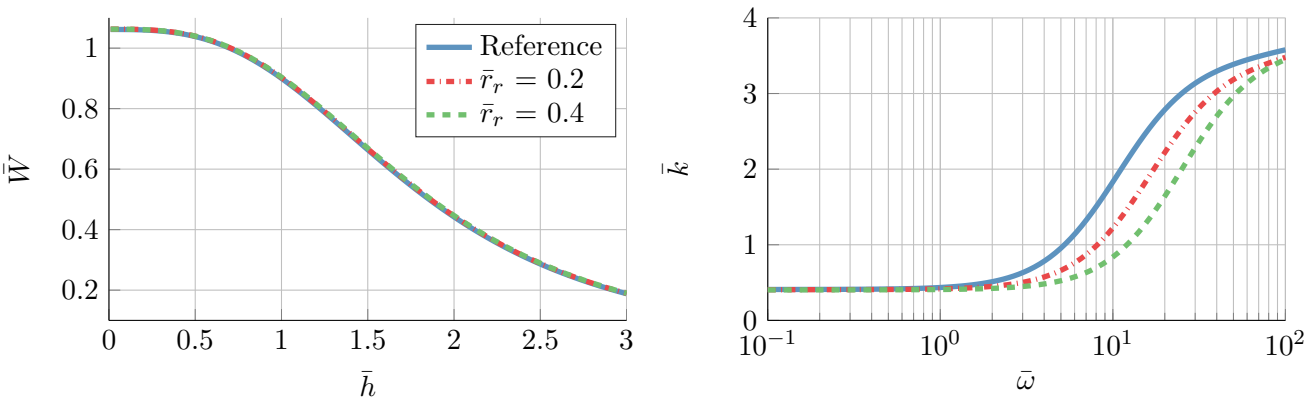

Figure 5-18: Equal load capacity for different bearing geometries. A change in restrictor radius is compensated with the restrictor pressure and conductivity, leading to a constant static behaviour but different frequency responses.

load capacity, and thus needs a larger radius for equal dimensioned load capacity. This will also shift the dimensioned frequency response to the left. Therefore, the low stiffness range in the frequency domain of concept two is larger.

For low transmissibility, damping should also be minimized. Concept one has an overall lower damping, and also declines at a lower frequency. Therefore, in the frequency domain also a trade off has to be made between low damping and a low frequency range or increased damping and a higher frequency range.

In this optimization study, frequency behaviour is not discussed in the objective or constraints. The optimization is conducted only for the static response of the system. Although definitely of influence on the transmissibility, frequency domain characteristics have been omitted from the optimization and only shortly discussed. A future algorithmic optimization could take the frequency behaviour into account, by including it into the objective or constraints.

However, some thoughts and ideas were formed on how such an optimization could be shaped. During manual optimization, different geometries have shown equal $\bar{W} - \bar{h}$ characteristics but different dynamic properties. For example, a change in restrictor radius can be compensated by changing source pressure and conductivity.

This is shown in Figure 5-18. The reference design is drawn, combined with designs where the restrictor radius is changed to 0.2 and 0.4. By lowering the source pressure and increasing conductivity, static behaviour has remained identical. This creates the possibility to optimize dynamics after a promising static design is found.

5-5 Dimensioned design

In the previous section, two dimensionless concepts are discussed. To convert the dimensionless designs into dimensioned design, conversion factors need te be determined. As an example, concept two will be scaled to 10 N load capacity at a 10 µm operating point.

First H is determined by choosing the dimensioned fly height at which the operating point is to be placed. At $\bar{h} = 0.62$, stiffness is minimal. This dimensionless height should correspond

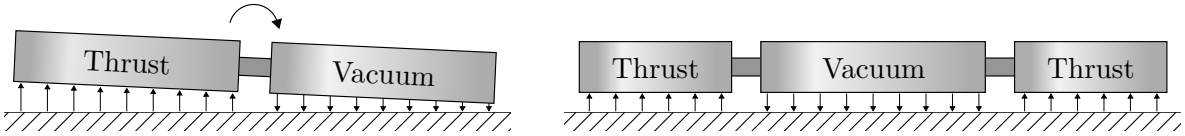

Figure 5-19: Combining a thrust and vacuum bearing will result in a net torque, causing the combination to tilt. For tip-tilt stability, the vacuum bearing is enclosed with thrust bearings, solving this problem.

to 10 µm. H can be determined with:

$$H = \frac{h}{\bar{h}} = \frac{10 \cdot 10^{-6} \text{ [m]}}{0.62} = 1.61 \cdot 10^{-5} \text{ [m]} \tag{5-3}$$

This also sets the pocket depth at $0.1\,H = 1.6\,\mu\text{m}$. R can be found by choosing the load capacity at the operating point:

$$R = \sqrt{\frac{W}{\bar{W}\,P}} = \sqrt{\frac{10 \text{ [N]}}{1.08 \cdot 10^{5} \text{ [Pa]}}} = 9.6 \cdot 10^{-3} \text{ [m]} \tag{5-4}$$

The restrictor conductivity can now be found with (B-11), which gives $G_r = 7.22 \times 10^{-16}\,\text{m}^2\text{s}^3/\text{kg}$. Assuming a restrictor diameter of 0.18×10^{-3} mm, this gives a restrictor length of 11.8 mm.

Finally, the frequencies can be dimensioned. The conversion from ω to $\bar{\omega}$ is given by:

$$\omega = \bar{\omega}\,\frac{P\,H^2}{12\,\eta\,R^2} = \bar{\omega} \cdot 1.3 \cdot 10^{3} \text{ [rad/s]} \tag{5-5}$$

So at $\bar{\omega} = 1$, the frequency is $f = 1.3 \cdot 10^3/2\,\pi = 207\,\text{Hz}$.

Doing similar calculations on the height difference design, leads to $H = 5.40 \times 10^{-6}\,\text{m}$, $R = 13.6 \times 10^{-3}\,\text{m}$ and $\bar{\omega} = 1$ at 12 Hz. The thrust conductivity is $8.2 \times 10^{-17}\,\text{m}^2\text{s}^3/\text{kg}$ and the vacuum conductivity is $5.4 \times 10^{-17}\,\text{m}^2\text{s}^3/\text{kg}$. The height difference between the vacuum and thrust bearing is $(1 - 0.9)\,H = 0.5\,\mu\text{m}$.

Tip-tilt stiffness

The dimensioned design consists of a single thrust and a single vacuum bearing. Connecting these bearings will result in a net torque, causing the combination to tilt as sketched on the left of Figure 5-19. By enclosing the vacuum bearing with thrust bearings, the torque is cancelled, as drawn in the right.

Figure 5-19 is a 2D representation. In 3D the vacuum bearing must be enclosed with three bearings to cancel both tip and tilt torques. To maintain equal static characteristics, the total area of three thrust bearings should be equal to the previously determined value for one bearing. By adding n thrust bearings, their new radius r_n becomes:

$$r_n = \sqrt{\frac{r_1^2}{n}} \tag{5-6}$$

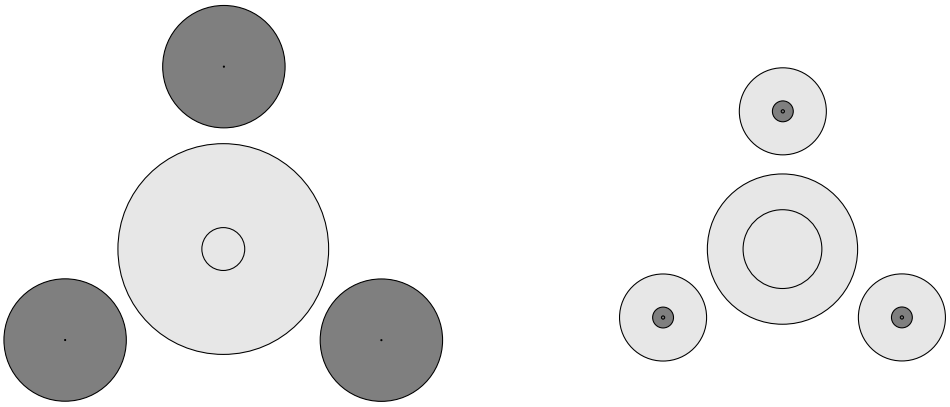

Figure 5-20: Top view of both low stiffness bearing designs, scale 1:1. Left is the height difference concept, right is the shallow pocket concept. Dark coloured surfaces are sunk deeper into the paper than the lighter coloured surfaces. The circles inside the vacuum bearings are the restrictor radii, so both design utilize a virtual pocket.

where r_1 is the radius of a single bearings. Static behaviour of the system of bearings remains equal, dynamic behaviour changes. Because the thrust bearings are becoming smaller, the frequencies scale up.

In Figure 5-20, the top view of both optimized designs is drawn. Both drawings are of scale 1:1. The dark coloured surfaces are sunk deeper than the light coloured surfaces. Concept one is drawn on the left, concept two is drawn on the right. Both design have a virtual pocket, which can be seen by the concentric circles in the vacuum bearings.

5-6 Conclusions and outlook

In this chapter, the concept of transmissibility and how it can be influenced is explored. This leads to the conclusion that, for the applications in mind, reducing stiffness and damping is the favourable option. Subsequently, a dimensionless analysis is introduced and a parameter study is conducted to see the influence of bearing geometry on the static and dynamic behaviour.

A vacuum bearing, normally used to pre-load a thrust bearing, is added to the analysis to compensate the thrust bearing's stiffness. However, this does not lead to a stable design. Nonetheless, by introducing a height difference, stable design can be realised.

Two concepts are discussed. Concept one uses a height offset between the thrust and vacuum bearing, concept two uses a shallow pocket in the thrust bearing. Both designs are optimized manually, and some remarks regarding a possible algorithmic optimization are made. Finally, the dynamic properties of the design and the conversion to a dimensioned design are discussed.

In the next chapter, the practical side of manufacturing the proposed designs is treated. Both uncertainties in air bearing surfaces manufacturing as design and realisation of restrictors will be treated. This will lead to some valuable insight in the production of air bearings.

6

Design realisation

With a design concepts for a low stiffness air bearing developed, this chapter deals with manufacturing critical parts of the design: the bearing surface and the restrictor. Since the design has strict demands on surface flatness and height offsets, manufacturing bearing surfaces has proven not to be a trivial task. Capillary restrictors feature large depth over diameter ratios, making manufacturing not trivial. The integration of restrictors into the design has also been found to be challenging. Both bearing surface manufacturing and restrictor integration will be discussed in this chapter.

6-1 Bearing surface manufacturing

The concepts, as discussed in section 5-5, have two surface features that require tight tolerance on manufacturing: flatness and a step in surface height. Flatness of bearing surfaces has to be accurately controlled to ensure constant film height. This will be discussed in the first subsection.

Both designs feature a height offset in the order of micrometers. One design uses three bearings with a shallow pocket with a depth of a few microns, the other features an height offset of a micrometer between the vacuum and thrust bearings. Manufacturing techniques for both designs will be treated in the second subsection.

To allow a fast cycle of manufacturing, assembly and testing, techniques analysed in this section are those available for MSc students in the work shop.

6-1-1 Surface flatness

In the preceding chapters, bearing surfaces are assumed to be parallel. If the modelled bearing behaviour is to be verified experimentally, the validity of this parallel surfaces assumption should be checked. To ensure a constant film height, both bearing and counter surface should be flat. First, for clarification, surface flatness is discussed. Next, achievable performance of different production methods is treated.

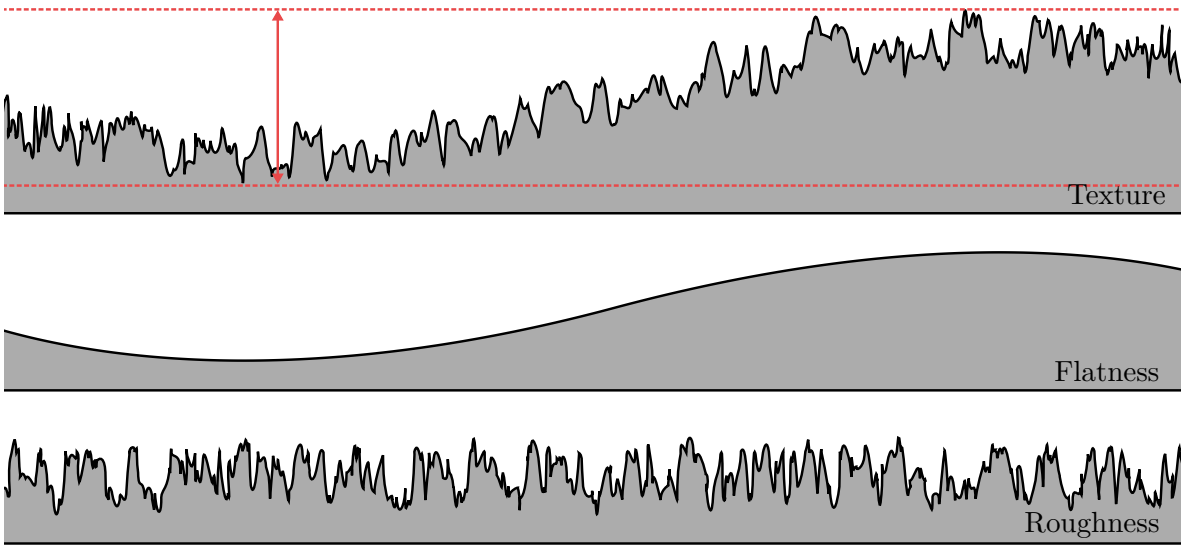

Figure 6-1: Cross section of surface profile and decomposition in low and high spatial frequency components. Surface flatness is drawn in red.

Surface flatness is the measure of how closely two parallel planes can be drawn such that the entire surface lies between these planes. It is often mistaken for surface roughness, so to clarify these terms the cross section of a surface and its spatial frequency decompositions are drawn in Figure 6-1.

The low frequency content, called the waviness, is drawn in the middle. The roughness, containing the high frequency content, is drawn on the bottom. If summed, the actual surface profile is produced, often called the texture. The surface flatness is drawn in red.

The influence of high frequency content on bearing characteristics is assumed negligible for low average roughness values. The effect of low frequency content can not neglected [27]. Therefore, to achieve the best agreement with the model, reducing peaks in roughness is subservient to reducing the waviness.

Manufacturing techniques, as available in the work shop, have been tested to determine the most suitable technique for manufacturing of air bearings. The resulting surfaces were measured using a Veeco - Bruker ContourGT-K1 white light interferometer as available in the optics lab at Delft UT. Two optics have been used: IXL2.5 and IX20 with a 2.5 and 20 times magnification. Surfaces larger than the viewing area of 2.5X lens have been analysed using the stitch function, stitching multiple images together.

Surface analyses have been done with vision64 software that comes with the interferometer and with Gwyddion, an open source height map analysis tool.

All tests on manufacturing techniques were either done by or under the supervision of an employee of the workshop, to ensure proper usage of tools and optimal process settings. They also have been consulted on options to reduce waviness. The results per manufacturing technique will be discussed next.

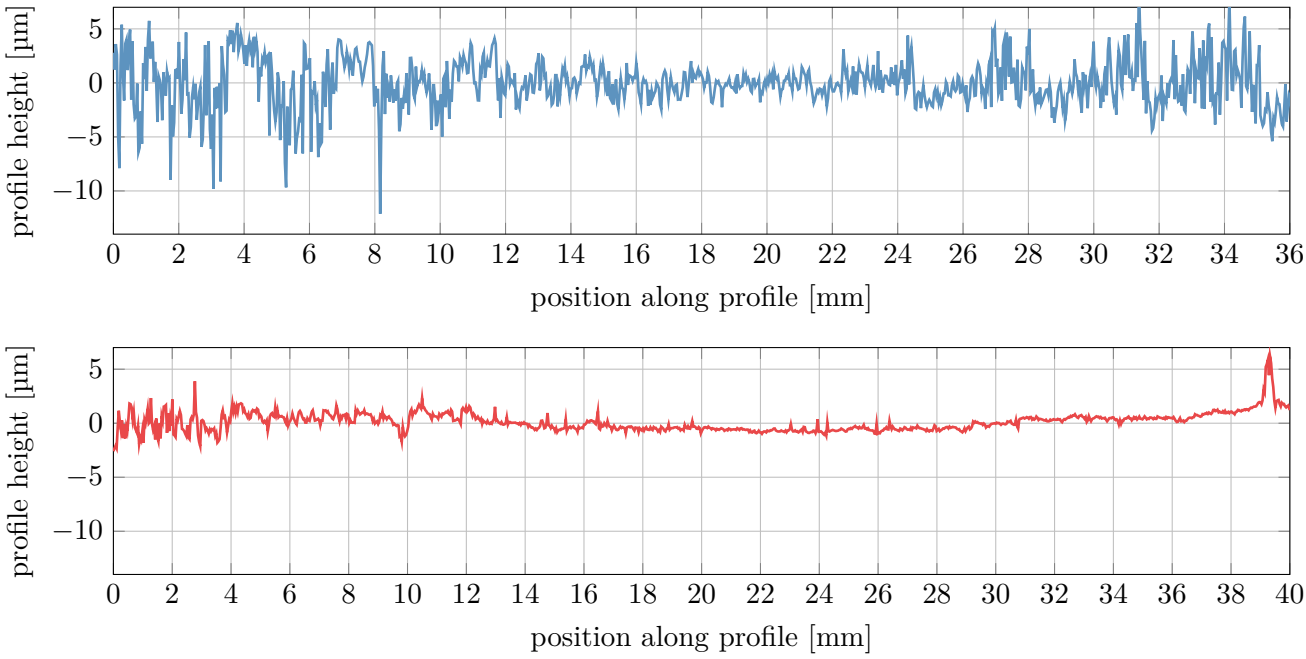

Figure 6-2: Measured surface profiles after grinding (top, blue) and lathing (bottom, red). The peak at $x = 40\,\text{mm}$ in the bottom graph is the typical peak at the rotational symmetry axis.

Milling

Bearing surfaces were milled with a face mill (Dutch: 'mantelkopfrees'). The resulting surface was concave with a waviness amplitude over 10 µm. This is likely caused by a slight tilt of the mill, resulting in an uneven removal of material. Because of the high amplitude of waviness, this method was decided ineffective.

Surface grinding

The process of surface grinding is similar to milling: a large revolving tool is moved over the work piece. Because the workpiece is held by a magnetic chuck, only steel is suitable. The waviness amplitude of the sample was acceptable, but the roughness was not. The measured profile of a steel counter surface is printed in the top axis of Figure 6-2, and has an R_a of 1.8 µm. In the figure can be seen that peaks over 5 µm are not uncommon. This roughness was assessed too large, since if both the bearing and counter surface have 5 µm peaks, there could be contact at a distance of 10 µm.

Furthermore, grinding does not allow for a height offset as is required for both designs. All grinded surfaces in one clamping operation are in the same plane.

Lathe

Waviness for lathed surfaces have been found to vary significantly depending on the machine. Newer machine in the workshop showed an almost sinusoidal pattern with an amplitude of

5 µm for radii between 5 and 15 mm. This pattern is probably caused by flaws in the linear guidance of the cutting tool, since it was observed in multiple workpieces at equal radii

The older machines had more recently been serviced and showed superior flatness. The result of lathing a stainless steel workpiece with a 40 mm radius at low feed speed and with excessive lubrication is plotted in the bottom axis of Figure 6-2. The peek at 40 mm is the typical peek for lathing at the rotational symmetry axis, where less material is cut. The average roughness is $R_a = 0.3$ µm, the waviness amplitude is acceptable at around 3 µm peak to peak.

Contrary to grinding, lathing allows for a step in surface height as required in the low stiffness designs. This will be further explored in the next section. The option for a step in surface height and because of the acceptable waviness and roughness have lead to the decision to use a lathe for bearing manufacturing.

Lapping and polishing

After lathing a bearing surface, the flatness can be further improved by precision lapping and polishing. Although high precision lapping machines are commercially available [28], [29], no such machines are available at the faculty of mechanical engineering to the knowledge of the author.

At the material science faculty, lapping and polishing machines are available where the workpiece is held by hand. These machines are used to prepare samples for microscopy by reducing roughness. Experiments showed that, although the roughness can be significantly reduced with these machines, the waviness will increase. Because the samples are hold by hand, more material is removed at the edge of the surfaces than on the inside, resulting in an umbrella shaped profile. The author did not achieve to reduce waviness of a surface that was lathed. Therefore, produced bearings have not been lapped and polished.

6-1-2 Shallow pocket manufacturing

Both low stiffness designs feature a height offset in the order of µm. Shallow pocket requires a step in height in a bearing surface, height difference requires a step in height between thrust and vacuum bearings. In this subsection, research on the production of a shallow pocket is discussed. The conclusion for this research also apply to the manufacturing of a height difference between bearings.

The goal of this research is to find a repeatable method for producing a shallow pocket. Figure 6-3 illustrates the scale of a 2 µm pocket on a 20 mm diameter bearing. The bearing is drawn at a scale of 7:1. To see the edge of the pocket, the figure is enlarged twice: first a 10x zoom and second a 5x zoom. The nominal fly height of 10 µm is drawn with a dashed line.

Figure 6-3 illustrates the significant difference in length scales between bearing radius and pocket depth. The radius is four orders of magnitude larger than the height. The scale difference poses a challenge for manufacturing.

Three methods have been investigated to produce a 1 µm pocket: laser engraving, electrochemical etching and lathing. These methods will be discussed subsequently.

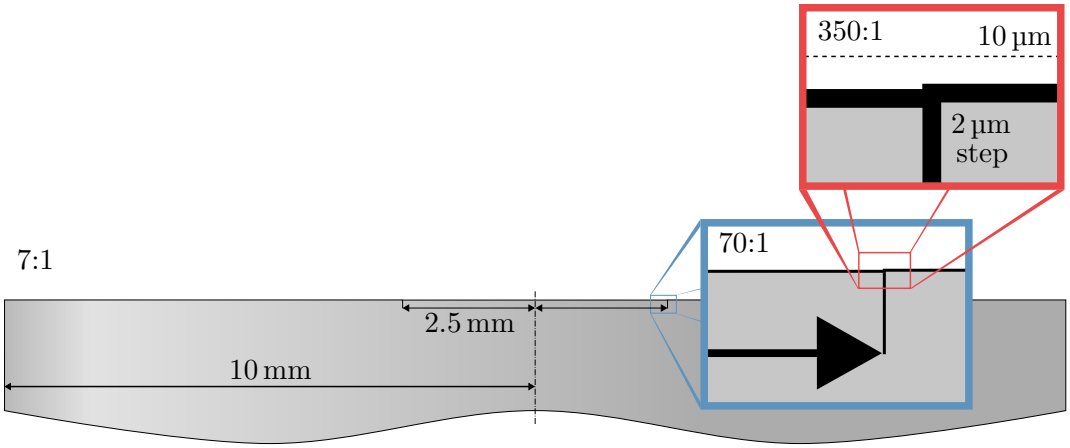

Figure 6-3: 2 µm pocket height on a 20 mm diameter surface. The main drawing is scaled 7:1, the blue box is zoomed at 70:1 and the red box at 350:1. The step, visible in the red box, is the edge of the pocket. The dashed line represents the nominal fly height at 10 µm.

Laser engraving

A CNC laser cut machine for cutting through plastics up to 10 mm thick is available in the workshop. This machine can also be used to engrave metals, by burning away a small layer of material. The machine has two software settings for controlling the path the laser follows, called cut and engrave.

Initial tests with engrave have showed infeasible results. The user draws a surface and the software automatically decides which lines are needed and how closely the lines are spaced to fill that surface. The laser makes a wide scanning motion over the surface and switches the laser on and off at the edge of surface. Analysis of the results has showed that switching the laser causes an undesired profile, with uneven material removal at the surface edge.

By setting the software to cut, the laser path can be imposed. By drawing a spiral with decreasing radius, a circular pocket can be engraved without starting and stopping the laser. Intensity and speed settings have been chosen such that the least amount of material was removed.

The results are drawn in Figure 6-4 showing a pocket with an average depth of 40 µm. The surface is rough, but this does not cause a problem for a deep pocket, since its pneumatic resistance is negligible. Some edges show burrs that have to be removed before this surface can be used as an air bearing.

This method is promising for the manufacturing of deeper pockets, where the depth is not controlled with µm precision. Because the laser is CNC controlled, different pocket shapes can be engraved. However, for shallow pockets with µm depth, production on this machine is not feasible. The most shallow pocket produced has a depth of 40 µm.

Electrochemical etching

Alternatively to laser engraving, electrochemical etching has been investigated as a shallow pocket manufacturing technique. Electrochemical etching is a process in which a current is

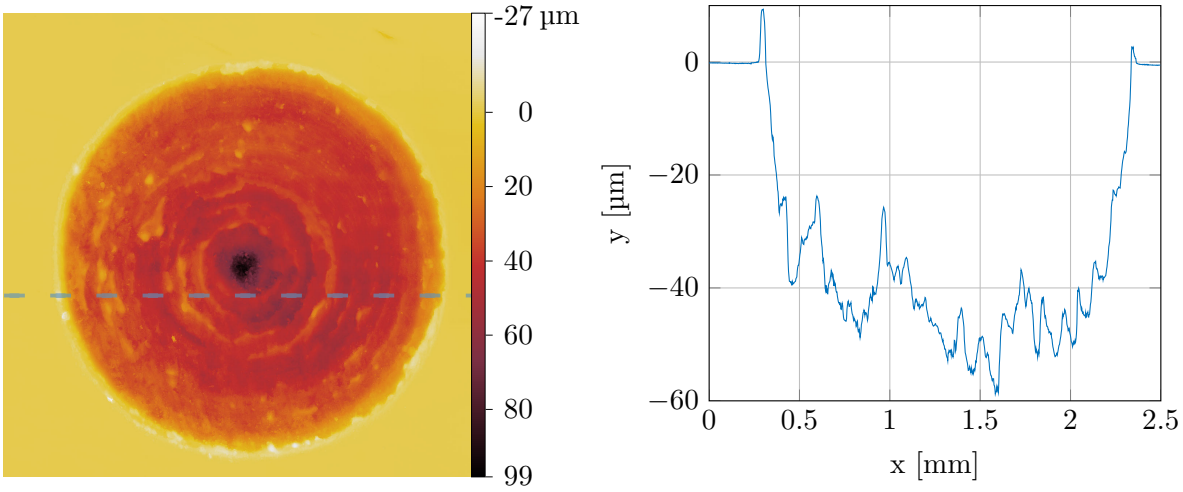

Figure 6-4: 2D surface and cross section plot of a laser engraved pocket. The blue dashed line in the left graph indicates the location at which the cross section is made. Surface size is 2.5 mm by 2.5 mm.

run through the workpiece while a solution of electrolytes is flushed over the surface, etching material. The size and shape of the etched surface is determined by a mask. An electrochemical etching machine is available at the material science lab, where it is used to treat microscopy samples.

Experimentation has showed this method to not produce suitable results. After 30 seconds of etching, a few microns of material have been removed, leaving a rough surface. The shape of the etched region did not mimic the shape of the mask. The round mask has given both round and oval shaped etched surface. Furthermore, lining up the workpiece with the mask proved difficult. The conclusion has been drawn that this manufacturing technique is not suitable for the fabrication of micrometer pockets with well defined radii and depths.

Lathing

The lathe that produced surfaces with a low waviness amplitude, as described in the last subsection, measures z displacement with a resolution of 5 µm. This is insufficient to make a 1 µm step. However, the resolution can be improved with a measurement gauge, as depicted in Figure 6-5.

The gauge is able to measure displacements with a resolution smaller than a µm. One complete revolution on the gauge is equal to 200 µm movement of the tip, the minor ticks depict micrometers. The gauge is mounted on the coarse z stage, and measures the difference between the fine and coarse z stage. The fine stage is put on under a 45° angle to amplify the measured displacement with a factor $2/\sqrt{2} = 1.4$.

With the gauge set up, pockets can be lathed into the bearing surface by cutting the path as drawn in Figure 6-7. This process is described step by step:

0. Before lathing, the fine z stage is moved some small amount in positive direction, to ensure there is no backlash in both fine stage and gauge. The gauge is set to zero.

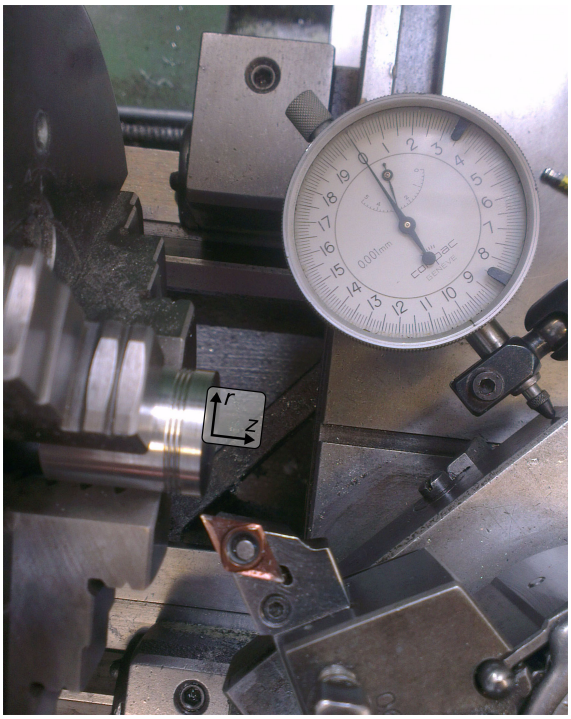

Figure 6-5: Measurement gauge with micrometer resolution fixed on lathe to measure fine z stage displacement

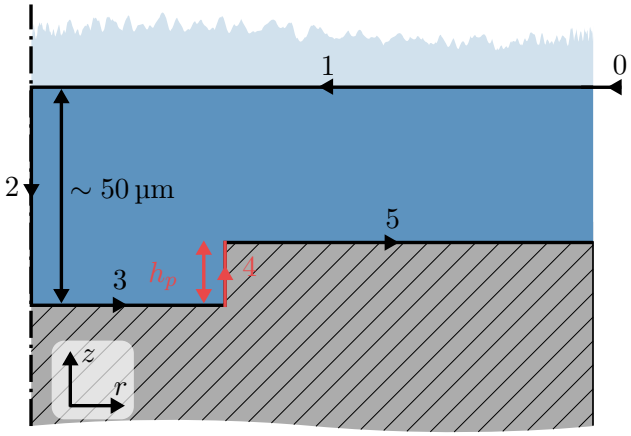

Figure 6-6: Cutting path for shallow pocket. Red line is controlled with fine stage.

1. The surface is flattened to ensure there are no scratches deeper than the intended bearing surface.

2. A $\sim 50\,\mu m$ step is made into the surface with the coarse z stage. Some margin on this depth is allowed, but a small step ensures small chips in the next cutting step and improves surface quality of the final bearing surface.

3. Before the final bearing surface is cut, the coarse z stage is fixed and the current value on the gauge checked. Thereafter, the surface is cut up to the pocket radius.

4. The fine stage is moved *very* delicately to the desired pocket depth. By tapping the fine stage handle, tiny steps can be made. If the intended pocket depth is overshot, the process is started again at step 0. Experiments have shown that moving the fine stage in opposite direction to correct the overshoot does not give reliable results, presumable caused by backlash in the fine stage and gauge.

5. The surface is finished by continuing the cut in r direction.

With this technique, pockets with a depth of $1\,\mu m$ have been produced, as can be seen in Figure 6-7. Because the depth in step 4 is difficult to control, some variance in produced pocket depth is to be expected. A white light interferometry measurement to determine the actual pocket depth is advised when using this method.

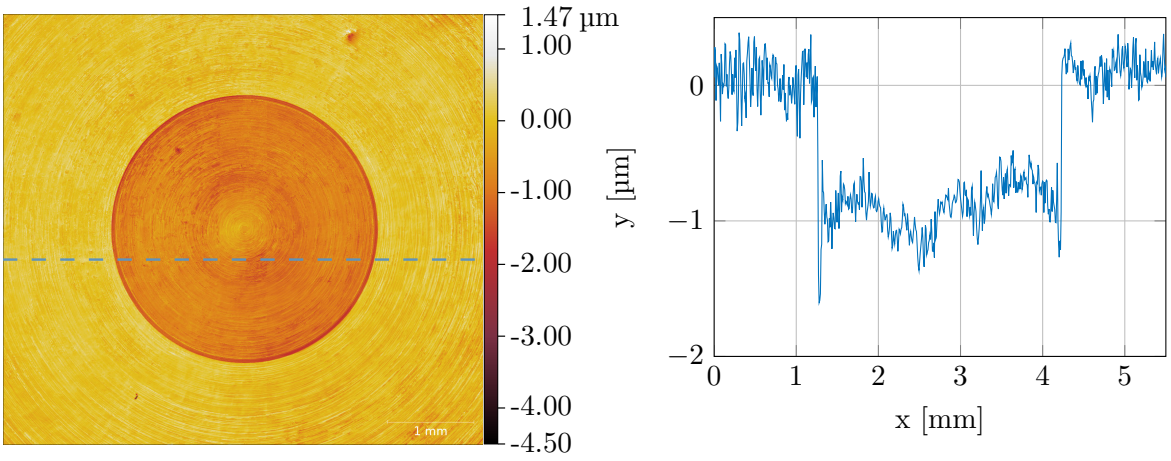

Figure 6-7: 2D surface and cross section plot of a 1 µm lathed pocket. The blue dashed line in the left graph indicates the location at which the cross section is made. Surface size is 5.5 mm by 5 mm.

Because this technique uses a lathe, only axisymmetric designs can be produced with this method. Therefore, it is not suitable for production of all three shallow pocket bearings as drawn in Figure 5-20 in a single clamping operation, since the pockets in this design are not axisymmetric around the middle axisymmetry line. The three thrust bearings could be produced separately and assembled, but this introduces the challenge of controlling the flatness between three thrust bearings. This will be discussed in detail in section 7-2.

The developed technique for a step in the bearing surface can also be used to create a height offset between bearings. By moving step 4 to a radius between the vacuum and thrust bearings, the height offset can be controlled. This enables this technique for the production of concept one, but requires the surface features in this final production step to be axisymmetric.

6-2 Restrictor integration

With the production of a bearing surface treated, this section will deal with restrictors. The choice for pneumatic tubes will be discussed and these tubes will be integrated into the design such that the chance of pneumatic instability is minimized. An experiment to determine the restrictor properties will be set up, which will lead to conclusions on the validity of the restrictor model.

6-2-1 Pneumatic tubes

A typical restrictor for an air bearing with 10 mm outer radius has a conductance value of $G_r = 1 \times 10^{-16}\,\mathrm{m^2 s^3/kg}$. A small restrictor diameter is needed to achieve this conductivity: for example, a diameter of 0.5 mm would require a length of over 5 m. However, since the conductivity scales with d^4/l, the restrictor length becomes approximately 10 cm for a diameter of 0.2 mm.

The combination of small diameter and high length over diameter ratio makes conventional techniques like drilling difficult. Drills with a diameter of 0.1 mm are available, but have

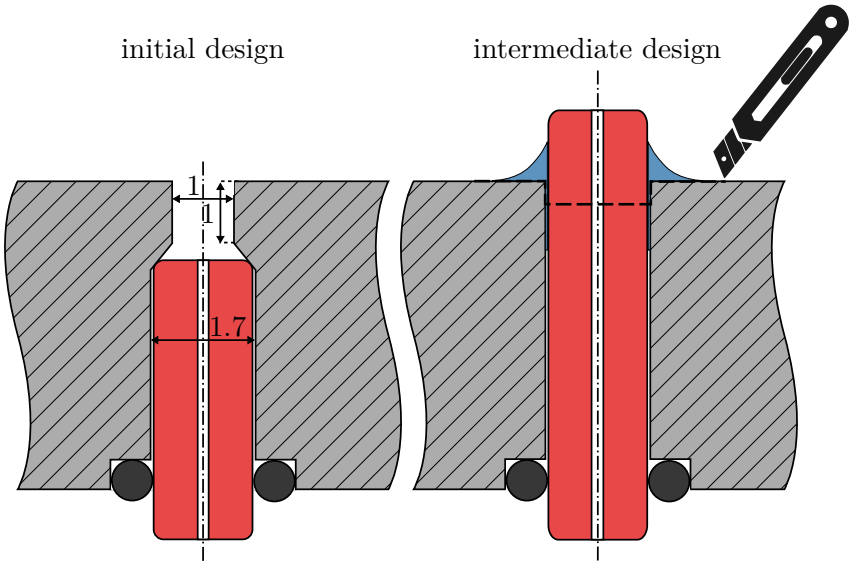

Figure 6-8: Initial and intermediate design to fix restrictor in bearing. Dimensions are in mm, the scale is 8:1. Downstream volume of initial design makes the bearing dynamically unstable. This is solved in the intermediate design, but bearing surface and restrictor are damaged by the cutting.

a length of only 2 mm, not reaching the required restrictor length. Alternatively, electrical discharge machining could be used to create small holes with the required depth, but this technique is not available in the mechanical engineering workshop at the TU Delft.

Therefore, a different approach is taken. Pneumatic tubes with diameters in the required range are available. The two smallest available tubes have a diameter of 0.18 mm and 0.13 mm, which give a length of 85 mm and 23 mm respectively. These are reasonable lengths, considering a bearing with a diameter of 20 mm. Therefore, these tubes provide a valid option for use as capillary restrictors. This increases the design complexity, since these tubes have to be integrated into the design. However, if these tubes are not permanently fixed, an additional advantage is that the restrictor can be switched to change bearing characteristics.

Minimizing thin film volume

To reduce the chance of pneumatic hammer, the volume downstream of the restrictor should be minimized [30]. Due to the compressibility of air, volumes in the thin film provide the possibility of storing energy in the lubricant film and releasing it in phase with the motion of the bearing system [24], leading to negative damping. This causes a self-excited instability known as pneumatic hammer.

In initial tests with manufactured air bearings, with the tube fixing design copied from the flower bed project, pneumatic hammer has been observed. The design used a narrowing to fix the pneumatic tube, as sketched in Figure 6-8. The volume upstream of the restrictor reduced the damping such that pneumatic hammer occurred.

The obvious solution of reduction of height of the narrow could not be produced. The depth of the 1.7 mm hole is difficult to control precisely, some safety margin is required. If too much

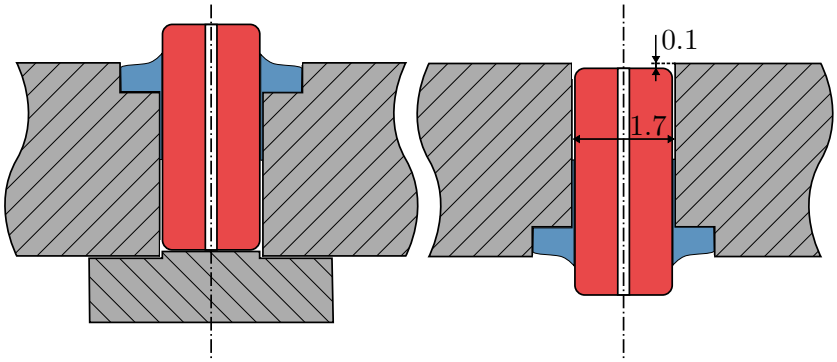

Figure 6-9: Final design of restrictor in bearing, dimensions in mm. The pneumatic tube is fixed by glue. The volume downstream of the restrictor is minimized, solving the pneumatic instability that occurred in the initial design.

material is removed and the 1.7 mm hole is cut all the way through to the surface, the bearing can be thrown away.

An alternative method for fixing the restrictor has been tested, labelled as intermediate design and drawn to the right of the initial design. The narrow has been removed, and the pneumatic tube has been extended from the bearing surface. Glue is applied such that the restrictor hole is not blocked by glue. After the glue has cured, the top of the restrictor and the glue are cut off, minimizing downstream volume. However, the cutting resulted in damage to the bearing surface and to the restrictor. Because the results varied significantly, this method was decided to be unreliable.

Another method for fixing the restrictors into the design has been developed. This method consists of two steps, as drawn in Figure 6-9.

In the first step, as drawn on the right, a removable inset is inserted into the restrictor hole. This inset has a step height of 0.1 mm to ensure the pneumatic tube is slightly sunk into the bearing surface. Next, the tube is inserted, pressed against the inset, and glued on the other side with cyanoacrylate glue. This glue has low viscosity and thus creeps into te space between the tube and the hole.

When the glue has cured, the inset is removed. In the drawing, the bearing is rotated 180° to allow comparison with Figure 6-8. This method proved to solve the pneumatic instability encountered in the initial design, and proved to give reliable and repeatable results.

6-2-2 Restrictor properties

To ensure that the restrictor conductivity of a bearing is as designed, a test set up has been developed to measure conductivity as function of pressure drop over the restrictor. In this subsection, the measurement set-up and results of the measurements will be discussed.

Measurement set up

A schematic of the conductivity measurement set-up has been drawn in Figure 6-10. Two versions of this measurement have been conducted, which is displayed by the switch on the

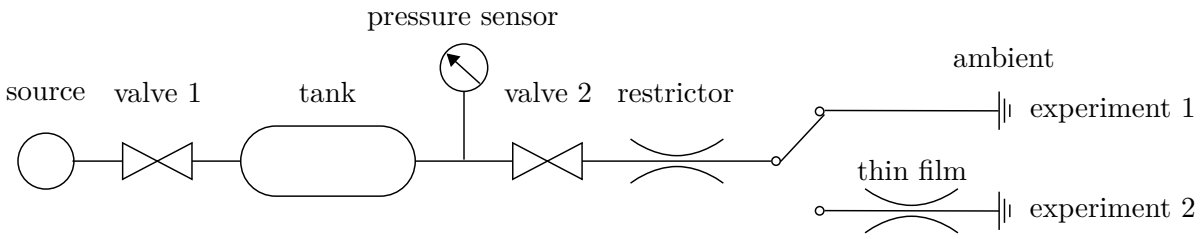

Figure 6-10: Schematic representation of restrictor conductivity measurement set up. Two versions of the experiments have been conducted by optionally adding a second resistance in series with the restrictor.

right of the scheme.

The set up contains 7 components. The source delivers air flow at an adjustable pressure. Valve 1 and 2 are Festo solenoid valves, which can be opened or closed. The tank is a Festo CRVZS-2 tank, with 2 l capacity. The sensor is a NXP MPX 5700DP differential pressure sensor with a range of 7 bar.

In experiment one, the restrictor as integrated in the bearing is the last component in the pneumatic circuit. It is vented to ambient pressure. In experiment two, a counter surface floats on top of the bearing, adding an extra resistance in the pneumatic circuit since a thin film forms between bearing and counter surface.

The measurement procedure for both experiments is the same. First, the tank is filled with air by opening valve 1 and closing valve 2. If the pressure in the tank is at the same level as the source, valve 1 is closed. A few seconds later, valve 2 is opened and air flows out of the tank through the resistor(s). The pressure is measured and logged until the pressure in the tank is equal to ambient pressure.

Conductivity from measured pressure

With pressure versus time measured, the mass of air inside the system at any time can be determined with the ideal gas law:

$$m = \rho V = \frac{p V}{R_s T} \tag{6-1}$$

where V is the pressurized volume, in this case the tank and connecting tubes. Assuming constant volume and temperature, the mass flow out of the tank can be found with:

$$\dot{m} = -\frac{\partial p}{\partial t}\frac{V}{R_s T} \tag{6-2}$$

Finally, G_r can be found by rewriting (3-4):

$$G_r = \frac{\partial p}{\partial t}\frac{V}{R_s T}\frac{1}{p^2 - P_r^2} \tag{6-3}$$

where P_r depends on which experiment is conducted. For experiment 1, P_r is the ambient pressure P_a.

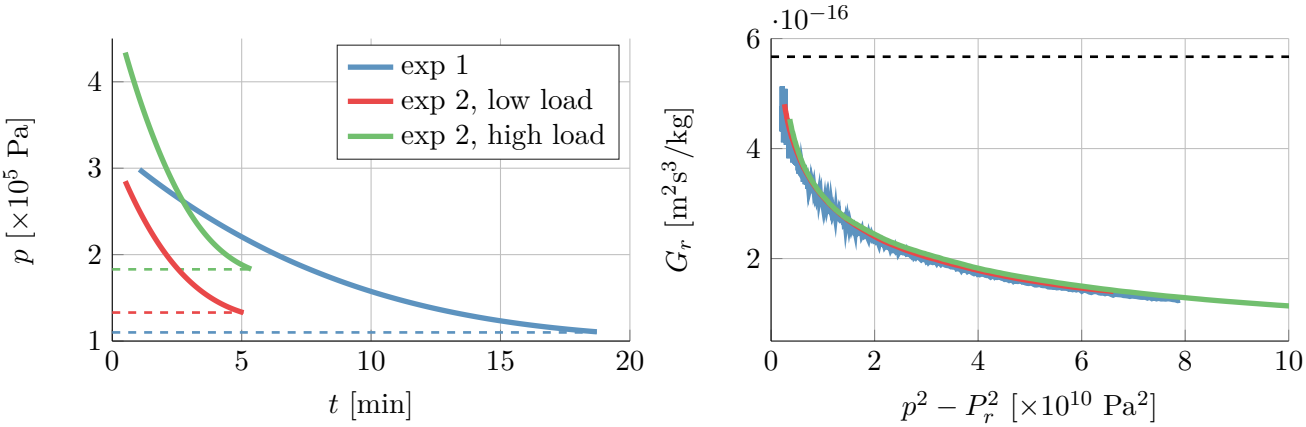

Figure 6-11: Measured pressure versus time and derived conductivity versus quadratic pressure difference. The dashed black line in the right axis is the theoretical conductivity.

Determining P_r for experiment 2 is more complicated, since the pressure directly downstream of the restrictor is not measurable. However, if the load capacity remains constant during the experiment, the integral of the pressure distribution in the thin film must also remain constant since it determines the load capacity. For a parallel film, the pressure distribution is determined by the restrictor pressure only, assuming ambient pressure at outflow and constant geometry, see (3-12). Thus, the restrictor pressure is constant during the experiment and can be determined with the bearing geometry and load capacity.

Alternatively, it can be determined experimentally by measuring the pressure at which bearing and counter surface make contact. This will be treated in chapter 7.

The result of experiment 2 depends on a pressure that is not directly measurable, and is therefore more prone to errors. It also requires more time to set up, since the counter surface has to be aligned with the bearings. This will be treated in more detail in chapter 7.

Still, experiment two is conducted because it more closely resembles the actual operating circumstances of a restrictor in an air bearing. Also, it creates the possibility to investigate if a pressure drop with the same quadratic pressure difference at a different linear pressure difference gives the same conductivity. In other words, does $P_s = 1.5 \times 10^5$ Pa to $P_r = 1 \times 10^5$ Pa give the same conductivity as $P_s = 2 \times 10^5$ Pa to $P_r = 1.66 \times 10^5$ Pa, which have the same quadratic pressure difference? If so, the more accurate, more simple and faster experiment one can be used instead of experiment two.

Measurement results

The results of three measurements are shown in Figure 6-11. On the left, tank pressure versus time is plotted. The calculated conductivity versus the quadratic pressure difference is plotted on the right.

As can be seen in the left graph, experiment 1 has taken significantly more time than experiment 2: 18 minutes for experiment 1 versus 5 minutes for both version of experiment 2. To increase tip and tilt stiffness, experiment 2 has been conducted with three bearings, and thus with three

restrictors in parallel. This has increased flow with a factor three, explaining the difference in experiment time. This has been taken into account for the calculation of G_r.

All three experiment have been stopped at $P_s = P_r + 0.1 \times 10^5$ Pa. These values have been drawn with dashed lines. For experiment 1, P_r is the ambient pressure. For experiment 2, P_r has been determined experimentally at 1.23×10^5 Pa and 1.73×10^5 Pa. As expected, P_r increases with bearing load.

With P_r set, the quadratic pressure difference in (6-3) can be calculated. The time derivative of pressure can also be determined from the measurement. This leads to the measured conductivity, as plotted in the right graph. The theoretical conductivity, as determined by (3-4), is plotted with a black dashed line.

Two conclusions can be drawn from this experiment. First, the three experiments show similarity for the conductivity. To find the conductivity of a system, the more simple experiment one is sufficient, since the results are similar to the results of experiment two.

Second, the measured conductivity is significantly lower than the model introduced in section 3-2 predicts. For low pressure differences, the measured conductivity approaches the theoretical conductivity. However, at very low pressure differences the conductivity is lost in measurement noise and is left out of the graph, so if the theoretical value has been reached can not be determined with this set up.

The measured conductivity is not constant and drops sharply with an increasing pressure difference, increasing the mismatch between model and measurement up to a factor 6 for the measured range. The proposed model highly overestimates the conductivity and does not capture the measured restrictor behaviour.

By calculating the Reynolds number of the flow through the restrictor, some insight in validity of the proposed model can be created. For (linear) pressure difference greater than 0.3×10^5 Pa, the Reynolds number exceeds 10^3, which is stated as the maximum valid Reynolds number for the restrictor model [10]. Therefore, the set up has been operated outside the valid range of the current model, and a new model should be proposed.

The current model does not take compressibility and friction losses into account. A more suitable model would be that of *Fanno flow*, which is a Moody-type pipe friction problem but with large changes in pressure in the flow [22, sec 9.7]. The development of a Fanno flow model to describe restrictor mass flow is left as a recommendation.

6-3 Conclusions and outlook

In this chapter, two aspects in the production of bearing surfaces have been treated: surface texture properties and manufacturing of a height offset in the order of µm. Methods available for MSc students have been investigated.

Surface roughness is determined to be of less importance than waviness. Milling and grinding do not produce surfaces with the required waviness, lathing does. Precision lapping could improve both waviness and roughness, but the available lapping and polishing machines have proved unsuitable.

Pockets and height offsets in the order of µm can be produced with a lathe and micrometer gauge. Laser engraving could be used for deeper surface features, electrochemical polishing has not produced suitable results.

Because lathed products are axisymmetric, the shallow pocket design with three thrust bearings can not be produced in a single clamping operation. The height difference design can be produced in a single clamping operation.

The integration of restrictors into the design has also been treated in this chapter. Small restrictor diameters with large length over diameter ratios have been achieved with pneumatic tubes. Allowing volumes of air in the thin film when integrating pneumatic tubes can lead to instability. By using an inset, the tubes have been glued at a small offset from the surface, solving the instability and successfully integrating the tubes in the design.

Two experiments to measure restrictor properties have been introduced. Experiment one, where a pressurized tank is emptied through a restrictor, has proven to give similar results to the more complicated experiment two.

The measured conductivity does not agree with the theoretical conductivity. Only for small pressure differences, some agreement is found. For larger pressure differences, as will be used in the next chapter, a more complicated model that takes compressibility into account is required. Compressible duct flow with friction, known as Fanno flow, is recommended.

In the next chapter, design of test set ups will treated, taken the conclusions of this chapter into account. Experimental results will be discussed and compared to the models.

7

Experimental validation

With techniques for manufacturing bearing surfaces and integrating restrictors discussed, measurement set-ups can be build to validate the proposed model. In this chapter, measurement set-up one is introduced, which provided understanding in the behaviour of a single air bearing.

This has led to conceivable set-up improvements. Implementation of these improvements have resulted in the set-up two, which will be discussed subsequently. With this improved set-up, extensive measurements on both static and dynamic bearing behaviour have been conducted.

7-1 Measurement set-up one

Set-up one has been developed to measure fly height of a single air bearing for a certain load capacity. In this section, set-up design and experimental results will be covered.

7-1-1 Set-up design

Set-up one consists of an air bearing and a counter surface, called the target, as pictured in Figure 7-1. The target is suspended by two wires, fixing its x and y position. It is supported in z direction by the air bearing.

To align the bearing with the target in x and y, the bearing is put on two hand controlled micrometer stages. This allows fine tuning of the bearing's position relative to the target. The bearing is put under a slight angle by a tip-tilt stage to ensure tension in the wires. The angle in Figure 7-1 is exaggerated to be visible in the photograph. When conducting a measurement, the angle is reduced to a minimum.

With the bearing and target aligned, the air supply can be switched on. A thin film of air forms between the surfaces on which the target floats. To measure film height, tip and tilt, three sensors have been used. They are positioned on a concentric circle to the bearing.

With this set-up, the air gap height is measured indirectly, by taking the difference between height at contact and height with a thin film. Instead of integrating sensors into the target to measure the fly height directly, this method has been chosen because it requires no connection of sensor cables to the target, minimizing unaccounted forces on the target.

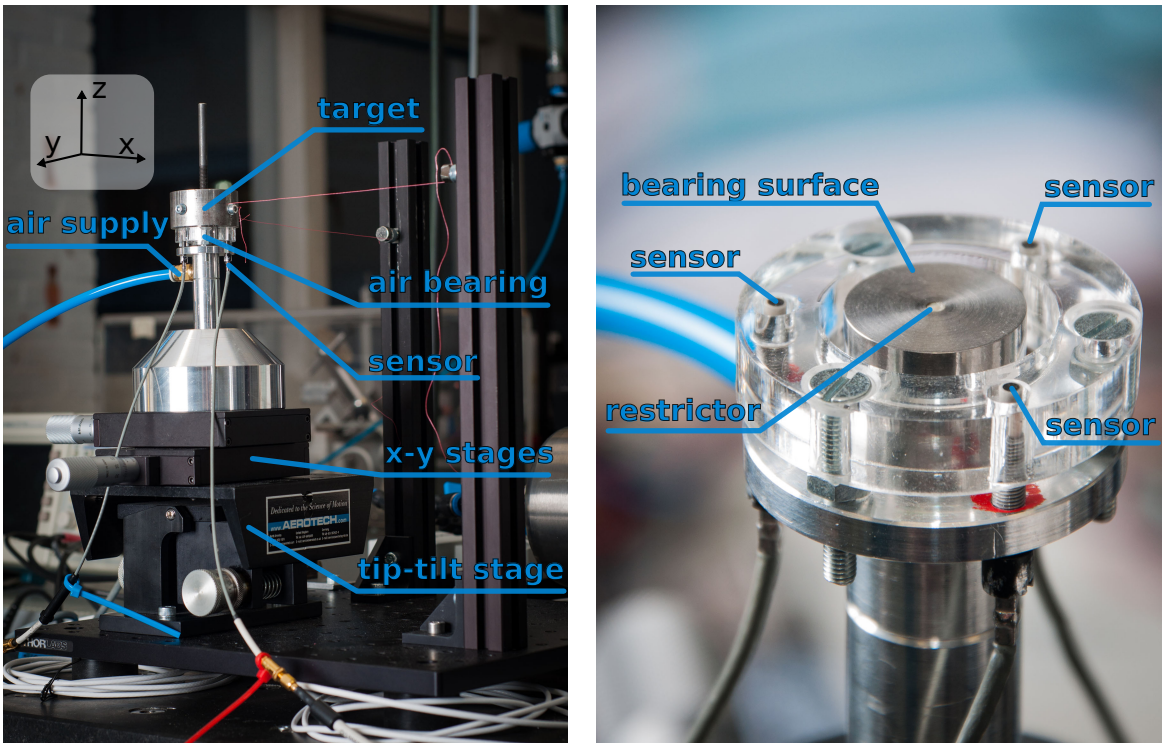

(a) Full set-up **(b)** Detail of bearing and sensors

Figure 7-1: Set-up up for measurement of characteristics of single bearing

Multiple load capacities can be measured by adding weights on top of the target. The weights are centred with a bolt, protruding from the top of the target.

Sensors

Three eddy current sensors are fixed around the bearing surface as can be seen in Figure 7-1b. The sensors are Micro-Epsilon U05(09) eddy current sensor with a range of 0.5 mm and a resolution of 0.025 µm [31].

The sensors are controlled by Micro-Epsilon DT3010-M controllers, which are specifically tuned for ferromagnetic target material. The controllers have been calibrated for the target, as described in the manual.

The sensors and controllers have been selected on basis of availability in the lab. Although the measurement range, 10 times the required range of 50 µm, could be smaller in return for an improved resolution, these sensors were the most suitable available and their resolution sufficient.

The controller type (DT3010-M or DT3010-A) determines if the target material should be ferromagnetic (steel) or non-ferromagnetic (aluminium, stainless steel). Since only ferromagnetic controllers were available, target material is steel, although stainless steel would be preferable.

Both the controller power supplies and sensor signal filters are integrated into a rack mount

case, which has been inherited from the previous set up in which the sensors have been used. The filter schematics, which retrieval was an effort, show a third order type II Chebyshev low pass filter with a cut off frequency of 10 kHz.

The filter circuit also comprises features for adding a DC offset and amplification to the output signal. By moving jumpers and adjusting trim pots on the PCB, offset and amplification can be controlled. Circuit schematics, jumper lay-out and trim pot functions can be found in Appendix D.

The sensor sensitivity and linearity have been determined with a calibration set-up. The distance between target and sensor was varied with a micrometer stage. Output voltages have been measured as a function of relative displacement. Although the results of this calibration can not be directly re-used in a different set-up since it depends on trim pot settings in the controllers, it is included in Appendix D to give some insight in sensor sensitivity and linearity.

Data acquisition

Data is acquired with a National Instruments NI USB-6211 DAQ which samples at 250 ksamples/s divided over the number of channels that are measured. By oversampling the measured heights, resolution is improved with a low pass filter.

Pneumatics

The pneumatics of measurement set-up one are equal to experiment two of Figure 6-10. It consists of a source, tank, pressure sensor, two valves and an air bearing.

Measurement procedure

With the target supported by the bearing and sensors calibrated, fly heights can be measured for given load capacities. To match the modelled air gap geometry, the target should be parallel to the bearing surface.

If the target's centre of mass is not aligned with the bearing centre, the air gap will not be parallel. The distance in x and y between the weight vector pointing down and the bearing force pointing up causes a torque around x and y. This torque is balanced by tip and tilt in the film. In the lower part of the tilted air film, pressure will be increased compared to the higher part. This cause a torque, countering the torque due to load vector mismatch.

By moving the bearing in x and y direction underneath the target, the load capacity vector and weight vector mismatch is reduced. When properly aligned, the air gap is parallel and at a maximum height.

To measure the fly height, a reference position at contact has to be determined. With valve 2 closed, the target rests on top of the bearing. This position is used as reference. By turning on valve 2, pressure builds and a thin film of air forms between bearing and target. The fly height, tip and tilt can now be determined by multiplying the difference from the current sensor voltage and the zero fly height sensor voltage with the calibrated sensitivity.

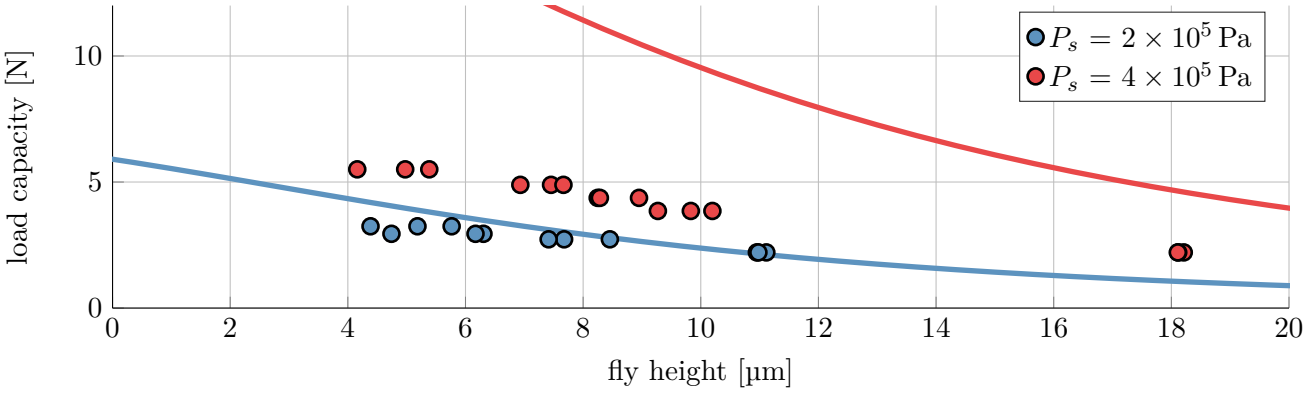

Figure 7-2: Measured and modelled load capacities for a single bearing for different feed pressures. Measurement tick marks correspond to model with the same colour.

By moving the bearing, measured tip and tilt can be minimized. If valve 2 is closed in a changed position and the target again rests on top of the bearing, the expected fly height is zero since it was defined as reference. However, it has been found not to return to zero. Changes in height up to 5 µm have been measured. Therefore, the reference zero height position and thus measured fly height are dependent on the position of bearing relative to the target.

If a new zero height reference is measured in the position which previously showed no tip and tilt, some tip and tilt reappears, caused by a change in reference height. To ensure a parallel film, a position is sought in which, after measuring the reference height in that location, the film shows to be parallel.

Thus, the bearing is moved slightly until tip and tilt appear to be zero again. In this new position, the pressure is switched off, a reference voltage is measured and the pressure is turned on again. If the tip and tilt in this position are within acceptable bounds, the fly height for that load capacity can be determined. If not, the process of moving, measuring a new reference and then determining fly height, tip and tilt is repeated.

This procedure has proven to be time consuming. For every measurement of fly height at a load capacity, the bearing has been moved multiple times before a parallel film was measured.

By adding a weight to the target, the x and y position of the centre of mass changes. Because of the low tip - tilt stiffness of a single bearing, this slight centre of mass change results in significant tip and tilt. Correction requires large changes in position, slowing the measurement process.

Even with the care taken in ensuring a parallel film, measured results show significant deviation, as will be discussed in the next subsection.

7-1-2 Experimental results

Measured fly heights for given load capacities are plotted in Figure 7-2. Four load capacities have been measured at 2×10^5 Pa feed pressure, drawn in blue and five load capacities have been measured at 4×10^5 Pa feed pressure, drawn in red. All measurements have been repeated

three times, resulting in three marks per load capacity. For every new measurement, the weights have been removed and placed back on top of the target, and the bearing has been realigned until parallel.

The deviation on fly height is significant, except for the values at 2.2 N. This is the weight of the target, without added mass. Although the extra mass is centred on the target, by taking it off and placing it back the centre of mass does not return exactly to the previous position. The lack of tip and tilt stiffness of a single bearing results in a required change in the position to form a parallel film. This causes the uncertainty in the measured fly heights.

Modelled results are also drawn in Figure 7-2 as solid lines. The modelled restrictor conductivity has been assumed constant and fitted to match the measured data for $P_s = 2 \times 10^5$ Pa. The modelled fly height was also lowered 9 µm. These setting have also been used for the $P_s = 4 \times 10^5$ Pa model.

Similarity between measurements and model are low. To match both stiffness and fly height, a significant height offset is required. Maximum modelled load capacity is significantly higher than measured load capacities, causing a large mismatch that cannot be fully explained by inaccuracy of the restrictor conductance. Clearly, the model does not fully capture the measured behaviour.

To decrease uncertainty in measured fly heights, decrease time required to set up an experiment and increase model and measurement similarity, a set up with three bearings has been developed. This set-up also resembles the design of Figure 5-20 more closely, and can therefore generate valuable insight towards a design with a vacuum bearing. Set-up design, results and comparison with modelled behaviour will be discussed in the next section.

7-2 Measurement set-up two

Set-up two has been developed to increase tip-tilt stiffness and reduce uncertainties in measured fly heights. It features three identical bearings fixed on a plate. Both static measurements, as carried out in the previous section as well as dynamic measurements, where the thin film is excited in z direction, will be treated in this section. First, set-up design is discussed.

7-2-1 Set-up design

Set-up two, pictured in Figure 7-3, consists of identical parts as set-up one, except for the bearings and target. The base is moved with a tip-tilt stage and two micrometer stages. Three supply lines feed the bearings with air. The target, a 160 mm diameter stainless steel cylinder, rests on top of the bearings and supports the extra mass, 1.8 kg in the picture. Fly height sensors and a contact sensor are integrated in the base.

In Figure 7-3b, the bearings and sensors can be seen more clearly. The bearings have a radius of 10 mm and are located on a circle, separated 120°, at an inside radius of 9 mm.

Bearing surface

Since a parallel film is to be measured and the target has a flat surface, the surfaces of all three bearings must be in the same plane. To ensure this, flattening the surface has been the

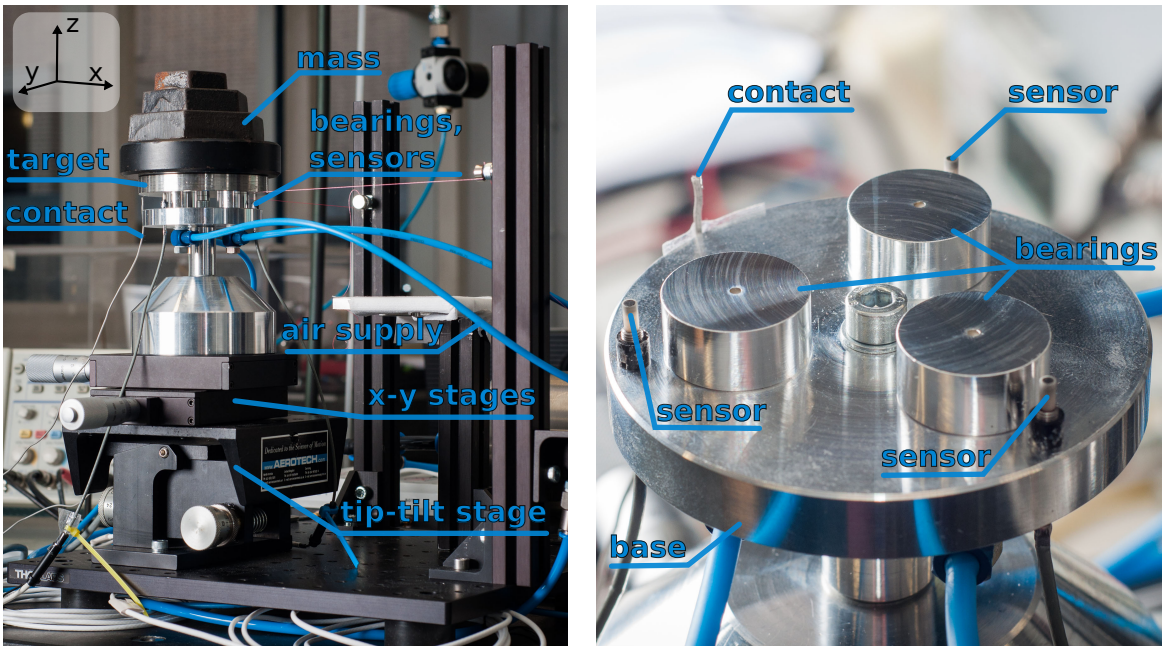

(a) Full set-up **(b)** Detail of bearings and sensors

Figure 7-3: Set-up up for measurement of characteristics of three identical bearings

final step in manufacturing of this set-up. The bearings, with restrictors integrated, are tightly fixed to the base by three bolts each. The base is clamped in the lathe and a small amount of material is removed from the top of the bearings. This ensures that all three bearings are in the same plane.

This is verified with white light measurements similar to those in section 6-1, but now over multiple surfaces. The results can be seen in Figure 7-4, where measured surfaces have been drawn in the top figure. In order to relate the heights of separate bearings to each other and make a successful stitch, a piece of aluminium foil is spanned across the surfaces.

Cross-section heights of the blue and red lines on the bearing surface are drawn on the bottom of Figure 7-4. The triangles mark the start of height map. The third bearing would be above the two measured bearings, so the triangles are at the inside radius of the set-up.

The cross-sections show two things. First, both bearing surfaces are in the same plane, as expected. Second, both bearings show poor flatness for low radii. The surface declines in a linear fashion up to a radius of 10 mm.

This profile is likely to be caused by a temperature change induced by cutting on the lathe. The surfaces are at room temperature when cutting starts and heat up by friction. The bearings expand, causing more material to be removed later in the cutting process. When the bearing is back at room temperature, the part of the surface that was cut at a an increased temperature now is lower than the part cut at room temperature.

Aluminium has a thermal expansion coefficient of around 22×10^{-6} 1/K. Assuming uniform heating of the bearings with a height of 10 mm, a 4 µm expansion could be caused by a temperature increase of only 20 K, which is not unlikely in machining.

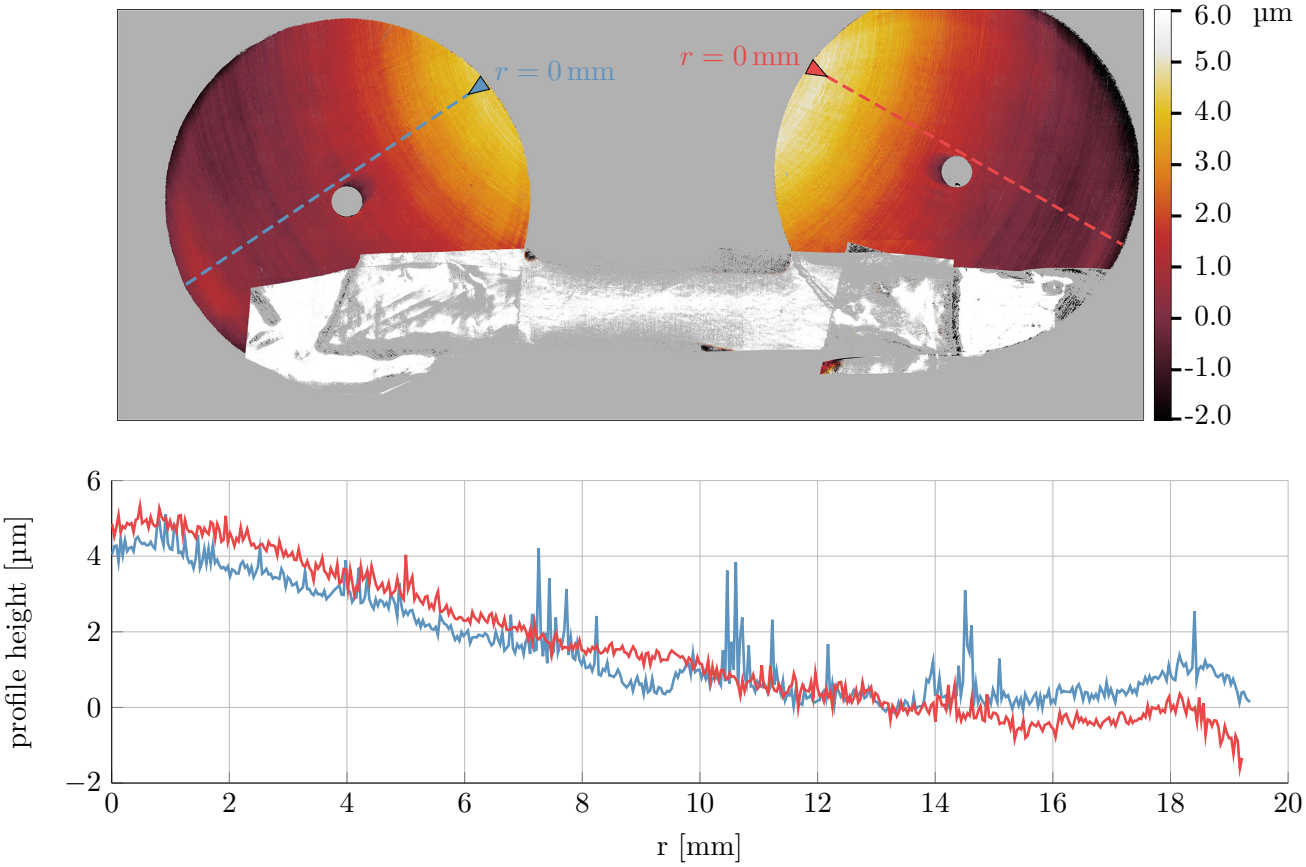

Figure 7-4: White light measurement of two bearings. A piece of aluminium foil is spanned between the bearings to allow stitching as can be seen in the bottom of the 2D graph. Surface size is 55 mm by 22 mm.

The non constant temperature could be solved by manufacturing a cylinder with the diameter of the base and height of the bearings. If holes are drilled at the locations of the bearings, this cylinder can be put on top of the base, adding material where now there is none. This would heat the bearings more evenly when flattening, since material would be cut before the cutting tool reaches the bearings. The aluminium foil in Figure 7-4 would also no longer be needed, since this cylinder could be used for stitching white light images. Manufacturing of this part is left as a recommendation.

The 2D model to which experiments will be compared, which will be discussed in more detail in the next subsection, takes this curved surface into account. A line has been fitted through the measured surface profile and has been added to the fly height.

Two other white light interferometer measurements, similar to that in Figure 7-4, have been conducted with both of the depicted bearings and the third bearing that is not in the image. The results are comparable to Figure 7-4.

Similar experiments have also been conducted on the target. The result of this measurement can be found in Figure D-4 in Appendix D. Target flatness is 2 µm. The surface profile is also fitted and added to the 2D model.

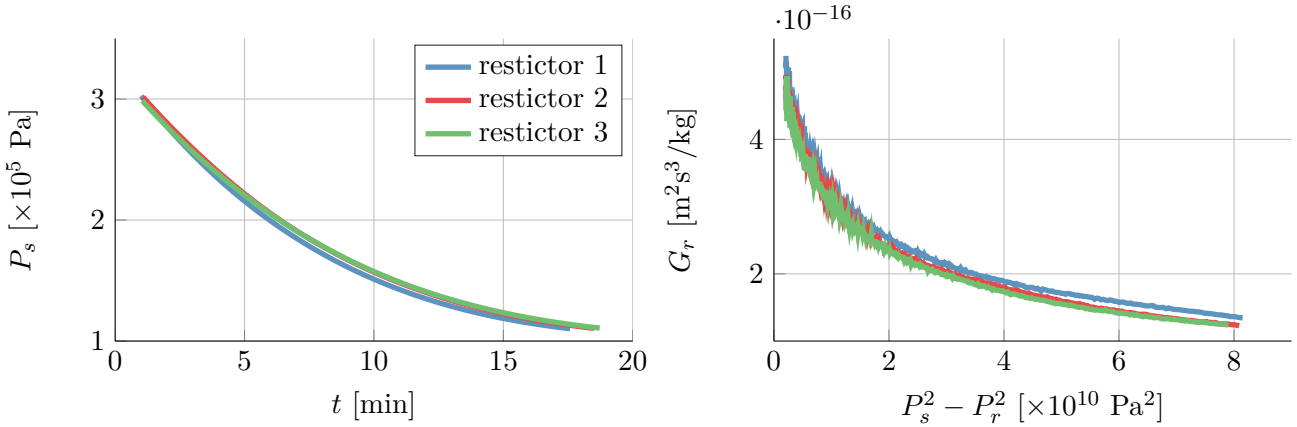

Figure 7-5: Measured pressure versus time and derived conductivity versus quadratic pressure difference for the restrictors in set-up two

Pneumatic system

The pneumatics of set-up two are similar to that of set-up one, only restrictor and thin film parts are different. For set-up two, the air supply is divided over three bearings, so the restrictor and thin film part of the pneumatic circuit in Figure 6-10 consists of three restrictors plus thin film resistances in parallel.

The restrictor conductivities have been determined with the method described in subsection 6-2-2. The results are plotted in Figure 7-5. The restrictors show very similar conductivity, which is a satisfactory result and shows that the method used for fixing the restrictors gives a repeatable result. Restrictor one only has a slightly higher conductivity.

The measured conductivities are averaged and a look up table has been created as a function of the quadratic pressure difference. This table has been used in the 2D model, which is described in the next section.

Sensors

The Eddy current sensors from set-up one are transferred to set-up two. Since the target material for set-up two is stainless steel, the controllers have been recalibrated. According to the manual, the controllers are not suitable for non-ferromagnetic targets, but by experimenting with controller settings, a linear voltage - displacement curve for a range of 0.1 mm has been measured. The measured sensitivity can be found in Figure D-3 in Appendix D.

The pressure sensor has been used in set-up two to measure pressure in the tank. This allows the determination of air flow.

Also, a contact sensor has been added. This relatively simple, self developed sensor consists of a wire to the base and a wire touching the target which is pictured in Figure 7-6. If the target is in contact with the bearings a small current can flow, caused by a voltage potential difference between the target and base. This current is amplified with a transistor and can be measured by the DAQ.

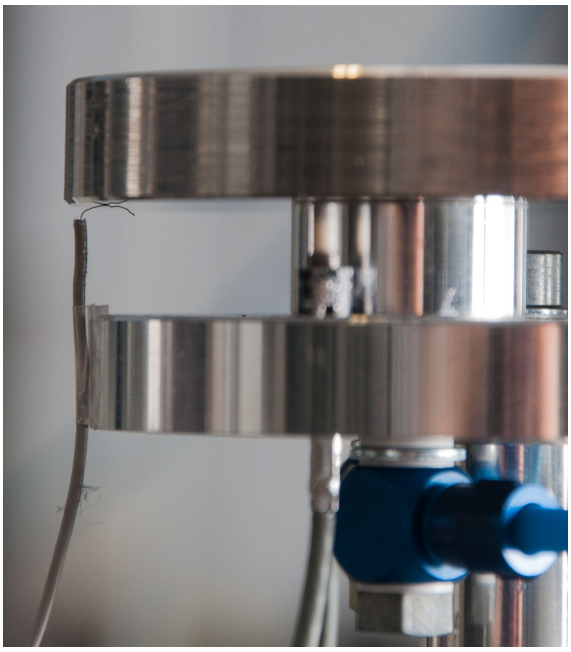

Figure 7-6: Contact sensor. A voltage potential between base and target will cause a measurable current flow if the target is in contact with the bearings.

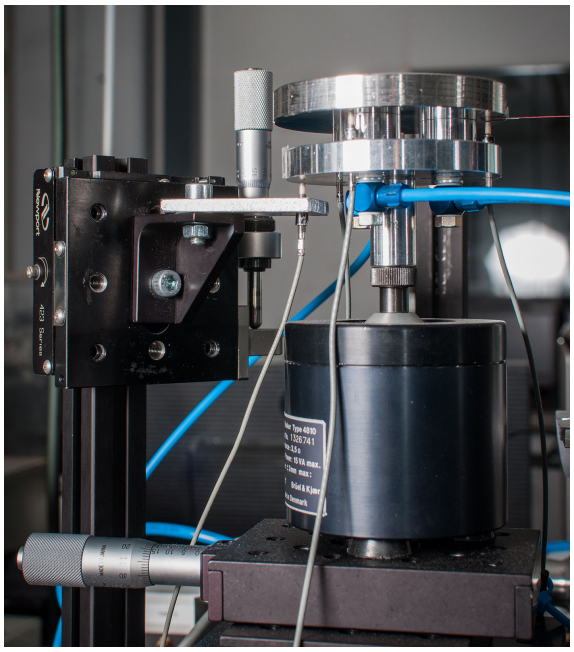

Figure 7-7: Set-up two with shaker and extra Eddy current sensor to measure transmissibility

Shaker for dynamic measurements

For dynamic measurements, a Brüel & Kjær Mini Shaker Type 4810 has been used to excite the bearings. The shaker replaces the large aluminium block that rests on the $x-y$ stages, as can be seen in Figure 7-7 .

Sinusoidal signals to vibrate the shaker have been generated with the analog output on the DAQ. This low power signal is amplified by a current amplifier. The shaker amplitude is controlled with the amplitude of the DAQ output signal.

To measure the sinusoidal displacement, a fourth Eddy current sensor of the same type as before has been used. It measures the displacement of the base and is fixed to the granite block on which the breadboard with the set-up rests.

With set-up two discussed in detail, the measured results can be reviewed and compared with the 2D model which will also be discussed. Two types of measurements, static and dynamic, will be treated subsequently.

7-2-2 Static measurements

In this subsection, the static measurements will be discussed. Although not at steady state, these experiments are called static because the bearings are not exited by the shaker. Before treating the results, the measurement procedure and updated model will be discussed.

Measurement procedure

To create more insight in bearing behaviour and have more data to compare the model to, not only the W- h curve will be determined, but also air flow and the effect of different source pressures will be measured.

An approach similar to experiment two of subsection 6-2-2 has been taken: a tank is filled with air and deflated through the bearing which supports the target. During this experiment, pressure, fly height and contact state are logged.

The procedure consists of two steps. First, the bearings are aligned at constant pressure such that a parallel film is formed, as described in section 7-1. Because of the significant increase in tip-tilt stiffness, aligning the bearings for a parallel film is notably more easy compared to set-up one.

Second, the actual measurement takes places. While logging fly height and pressure, the tank is deflated until contact is measured continuously for 1 minute. This experiment is performed multiple times per load capacity, realigning the bearings each time, to show repeatability. In total eight different load capacities have been measured, from only the target mass of 0.42 kg up to an additional mass of 1 kg.

From this data, mass flow and fly height at different load capacities and supply pressures can be determined and compared to the updated 2D model. This model will be discussed next.

2D model

As shown in subsection 7-2-1, the bearing surfaces and resulting thin film can not be correctly represented axisymmetrically. By using a 2D space, modelling the thin film as a circle instead of an axisymmetric line, the measured surface profile can be imposed. The developed model is similar to the model used in section 3-4, but now uses Reynolds equation in Cartesian coordinates as derived in Appendix A. The resulting model has been compared and verified with the axisymmetric model before adding the measured surface profile.

One of three bearings is modelled, the other two are assumed identical. Both bearing and target surface profiles have been taken into account by fitting a line through the measured surfaces and adding that to the fly height. All three restrictor conductivities have been measured. The average conductivity per pressure difference is computed from the data of the three restrictors and used as a lookup table in the model.

To simulate the full experiment of deflating a tank, two extra ODEs are added. In the model, the fly height is a parameter and the load capacity is dependent on the pressure profile, but in experiments it is the other way around. The first ODE sets the fly height such that the load capacity is at a given value.

The second ODE controls the pressure in the modelled tank:

$$\frac{\partial P_s}{\partial t} - \frac{3\,\dot{m}\,R_s\,T}{V} = 0 \tag{7-1}$$

where the mass flow $\dot{m}$ can be determined by integrating the Lagrange multiplier over the edge of the bearing. Factor three is to account for three bearings. The starting pressure $P_s\,(t = 0)$ is set in the ODE.

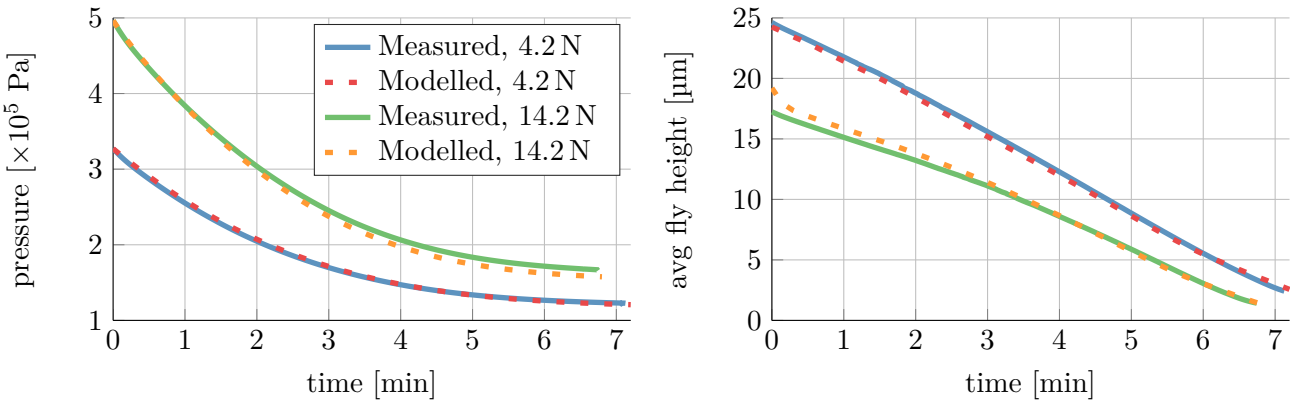

Figure 7-8: Measured and modelled pressure and fly height versus time for 4.2 N and 14.2 N load capacity. Model and measurement show excellent agreement.

The model can now be solved in three steps. First, an initial solution for a given fly height and source pressure is found. Next, the first ODE is added to find the fly height and pressure distribution for a given load capacity. Finally, the time dependent second ODE is enabled and the previous solution is used as the initial condition. The simulation stops at a given end time.

With both the measurement procedure and updated model discussed, the results can be compared.

Static results

Two static experimental results will be discussed and compared to the modelled results. First, the experiments where fly height and pressure are measured while deflating a tank are treated. From multiple of these experiments, a $W - h$ curve can be formed, which is discussed subsequently.

The results from two deflating tank experiments are drawn in Figure 7-8. The first measurement, in blue, has been conducted with a load capacity of 4.2 N, which is the target without extra mass and therefore the lowest measurable load capacity. In little over 7 minutes, the pressure decreases from 3.3×10^5 Pa to 1.2×10^5 Pa, at which contact has been measured. The average fly height at the moment of contact is not zero, but 2.4 µm. Because one of the restrictor conductivities is slightly higher, the fly height decreases faster over the other two. Therefore, one of these bearings is in contact before the average is at zero.

The second measurement, in green, has been conducted at maximum measured load capacity of 14.2 N. For this measurement, the average fly height also does not fully measure zero. All other measured experiments range between the two plotted experiments.

The 2D model is run with equal load capacities and starting pressures as measured in the experiments. The model results are plotted in dashed red and yellow. A systematic error in fly height of 2 µm has been observed. This error is probably caused by a mismatch in reference height and actual air gap height because of non perfect flatness. Subtracting this error improves the results for both measurements, and for all further measurements, as will be seen.

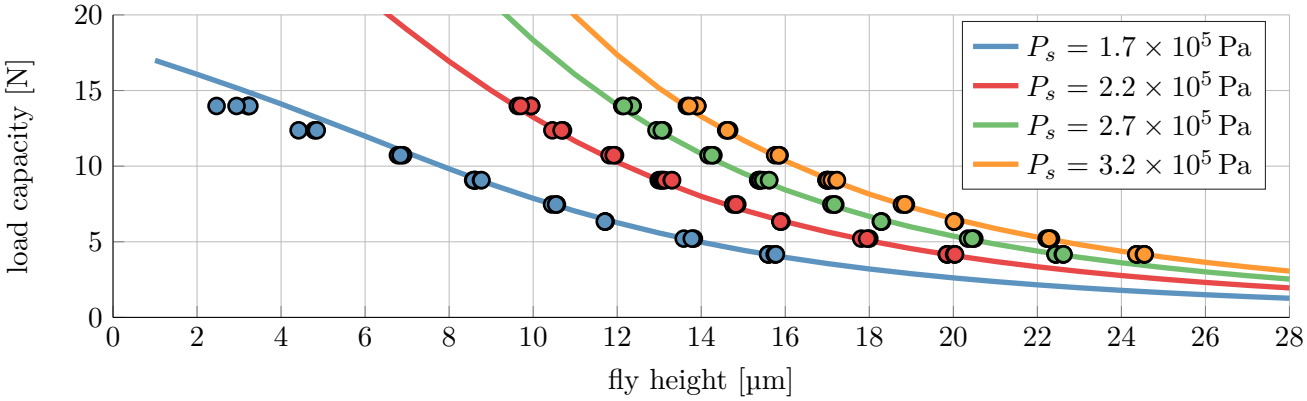

Figure 7-9: Load capacity versus fly height for different source pressures. Solid lines are modelled, points are measured. 2 µm has been subtracted from the modelled fly heights, shifting the model to the left.

With the systematic error removed, both measured and modelled experiments show excellent agreement. The pressure decrease and therefore the air flow is correctly captured by the model, as can be seen in the left graph. The 2D model computes the average fly height and does not take the difference in resistor conductance and resulting tilt into account. This assumption is sufficient to capture the actual behaviour, as can be seen by the agreement between both modelled and measured experiments.

The deflating tank experiment has been conducted 35 times in total, for 8 different load capacities from 4.2 N to 14.2 N. All loads have been measured at least three times, positions were reset each time. By looking up the fly height at the time the tank was at a certain pressure, a point on the $W - h$ curve is found for that particular supply pressure and load.

This has been done for four supply pressures in all experimental data, resulting in Figure 7-9. The dots represent the measured $W - h$ curve, where points with equal colour are taken at equal supply pressure but different load capacities.

Because of the increased tip-tilt stiffness, the uncertainty in measured fly height has been significantly decreased when compared to Figure 7-2. The deflating tank method has proven a fast an dependable method for measuring $W - h$ curves at varying supply pressures.

The results from the 2D model are included in Figure 7-9 as lines. The supply pressure used in the model corresponds to the supply pressure of the measured results with the same colour. 2 µm is subtracted from all modelled fly heights, as discussed in previous results.

Modelled and measured results show excellent agreement. By taking the measured surface properties and restrictor conductivities into account, the model can correctly predict load capacity at a certain fly height and source pressure. This validates the static model.

7-2-3 Dynamic results

In this subsection, the results from modelling and measuring the dynamic response from set-up two will be treated. By exciting the thin film with a shaker, the transmissibility as a function of the frequency can be determined.

First, the measurement procedure will be treated. Next, three 2D models will be discussed to which the dynamic results will be compared.

Measurement procedure

The transmissibility between two parts is defined as the ratio of displacements, as discussed in section 5-1. As can be seen in Figure 7-7, the absolute displacement of the base and the relative displacement of the target with respect to the base have been measured. The transmissibility can therefore be found by:

$$T = \frac{x_t + x_b}{x_b} \tag{7-2}$$

where x_t is the relative target displacement and x_b is the absolute base displacement.

The start of the measurement procedure is similar to the start of previous experiments. The bearing is aligned with the target to form a parallel film and a reference voltage is measured with the air supply switched off. When the air supply is switched on, the actual measurement can start.

The shaker movement is controlled by the power supply, which receives a sinusoidal signal from the analogue output of the DAQ. A constant amplitude input signal at different frequencies does not result in a constant amplitude movement of the base. Since bearing stiffness is dependent on the fly height, a small and constant amplitude base displacement is required for all measured frequencies to assume negligible change in bearing stiffness by change in fly height.

To control the amplitude of the measurement, a simple proportional feedback loop has been used. After one second of acquiring a time signal, an FFT is performed on the data with a flat top window applied. The amplitude at the excited frequency is compared to the required amplitude. If the measured amplitude is not within set bounds, another measurement at the same frequency is started. The input amplitude for this measurement is scaled proportional to the quotient of the target amplitude over the measured amplitude. This loop is repeated until the required amplitude is measured. That data is stored and the final input amplitude is used for the next frequency.

Dynamic models

Three models have been developed for verification and insight in the measured data. First, the static 2D model (without ODEs) has been expanded with linear perturbation, as discussed in chapter 4. With this model, the stiffness and damping as function of the frequency can be calculated, taking the measured restrictor conductance and surface profile into account.

Resulting stiffness and damping for two feed pressures have been drawn in Figure 7-10. Both have been evaluated at a load capacity of 4.2 N. The stiffness and damping are essentially constant up to 1 kHz. Above this frequency, stiffness increases and damping decreases.

This frequency dependent stiffness and damping have been used in the second dynamic model, which calculates transmissibility as function of frequency based on (5-1). Stiffness and damping,

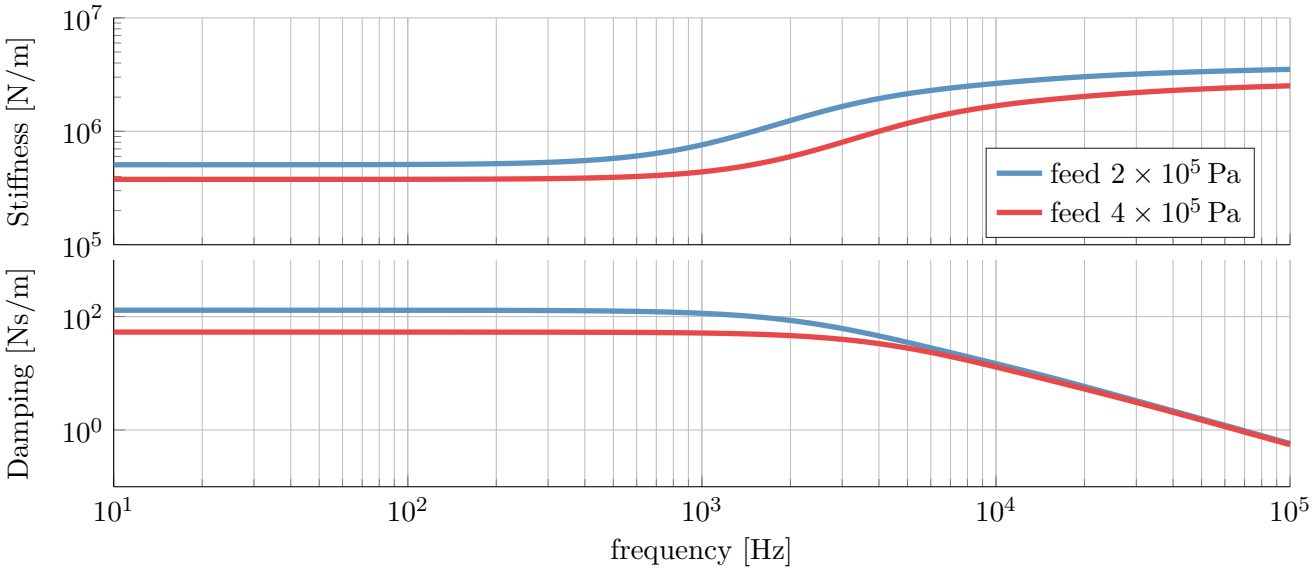

Figure 7-10: Stiffness and damping versus frequency for set-up two at different feed pressures. Models have been evaluated at $4.2\,\mathrm{N}$ load capacity, and show significant change in stiffness from $1\,\mathrm{kHz}$ and up.

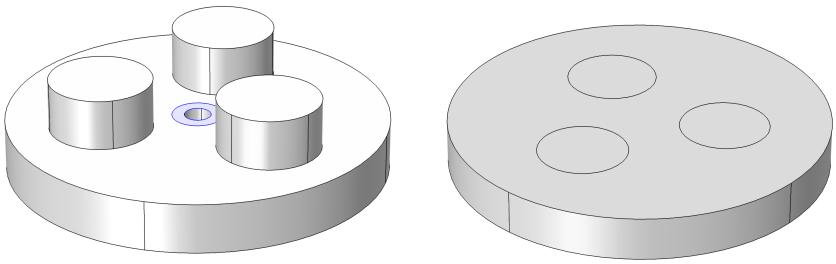

(a) Base and bearings **(b)** Target

Figure 7-11: Geometry models for eigenfrequency study of set-up two. Base and target are coupled with frequency dependent stiffness and damping, as drawn in Figure 7-10.

as found in Figure 7-10, has been used as a lookup table as function of frequency. The results will be discussed and compared to measurements in the next subsection.

Third, a mechanical finite element model has been developed to find the resonance frequencies of the base and target coupled by a thin film of air. The geometries of both base plus bearings and target are pictured in Figure 7-11. The blue highlighted surface on the base and a similar surface on the back side are fixed, modelling the clamping by a bolt. The bearings and target are coupled by boundary loads, where the forces on both surfaces are generated by displacements, coupled by stiffness, and velocities, coupled by damping. Both stiffness and damping are frequency dependent and taken from dynamic model one. The target is only allowed to move in z direction.

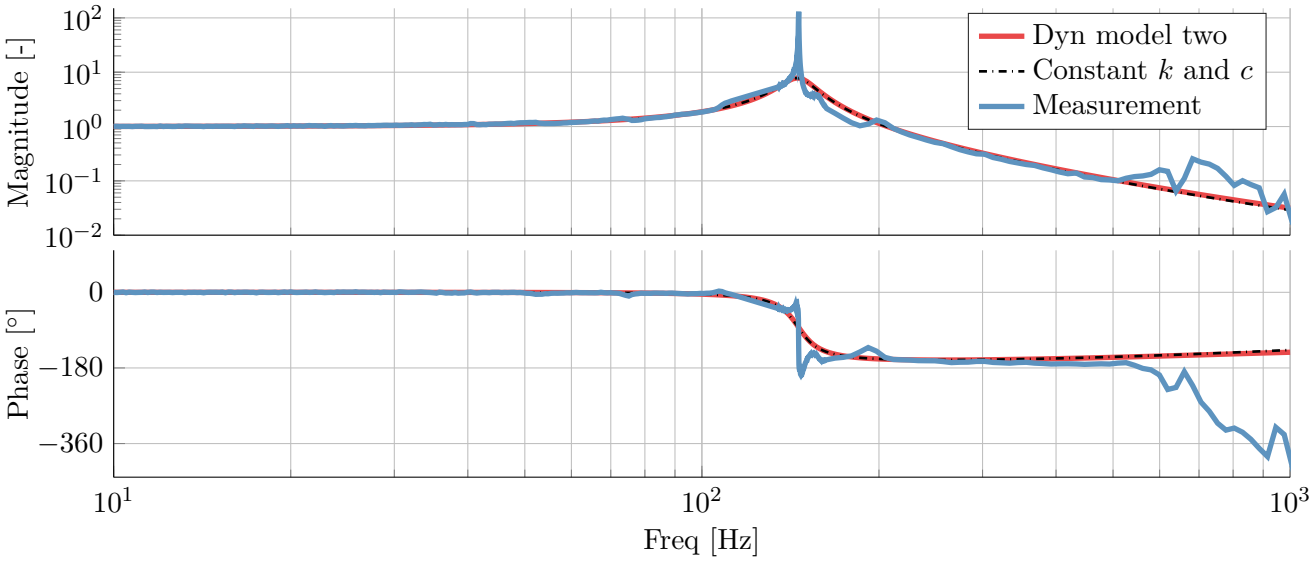

Figure 7-12: Modelled and measured transmissibility Bode plot at a source pressure of 4×10^5 Pa and a load capacity of 4.2 N. Since mass and stiffness are accurately know, measured and modelled first eigenfrequency match. Measured behaviour is as expected up to 5×10^2 Hz, above this frequency decoupling occurs.

Dynamic results

The transmissibility results calculated with dynamic model two can be found in Figure 7-12. Results drawn are for a source pressure of 4×10^5 Pa.

Up to 500 Hz, model and measurement show excellent agreement. Because the transmissibility curve is dependent on mass, stiffness and damping and these properties are accurately determined, model and measurement match.

For frequencies over 500 Hz, other phenomena, not taken into account in the simple transmissibility model, are measured. Eigenfrequencies found with dynamic model three can help to explain these phenomena. The first computed eigenfrequency and mode is the up and down motion of the target on the bearings, at 146.2 Hz, matching exactly with the measured response.

The second mode is torsion around the z axis at 3.2 kHz, beyond the maximum measured frequency. The measured effects are therefore not caused by eigenmodes of the bearings, base and target. Because the sensors are not fixed to the base with very high stiffness, sensor movement could cause the measured effects at 500 Hz and up. Finite sensor connection stiffness is not taken into account in dynamic model three.

To validate frequency dependent stiffness and damping, measuring the change in these properties would be insightful. However, increase in stiffness for the measured experiment is marginal, as can be seen in Figure 7-10. The increase in stiffness between 10 Hz and 500 Hz for a feed pressure of 4×10^5 Pa is only 5%.

This insignificance can also be seen in Figure 7-12, where the results of running the transmissibility model with constant stiffness and damping has been plotted in black dashdotted

lines. The difference between dynamic model 2 and a constant stiffness and damping model is smaller than the uncertainty on the measured transmissibility and therefore the change in stiffness and damping can not be seen in the measured data.

To increase the change in stiffness between 10 Hz and 500 Hz, dynamic model one has been evaluated at varying source pressures and load capacities. The highest change in stiffness between 10 Hz and 500 Hz has been found to be at 2×10^5 Pa and 4.2 N. The resulting k and c have been plotted in blue in Figure 7-10. The change in stiffness for this combination is 14%, which is improved but still too small to be measured. Therefore, the resulting transmissibility bode plot has been omitted, as it is very similar to Figure 7-12.

To increase stiffness and damping change, larger bearings could be used. Change in stiffness and damping has been measured in literature for bearings with a radius of 30 mm [32]. A similar model to the one used in this thesis has been verified with these measurements [24, 6.5.3]. However, repeating the experiments with larger bearings to verify the model used in this thesis is left as a recommendation.

To summarize: measured and modelled bearing behaviour show a good match up to 500 Hz. The measured stiffness is practically constant up to that frequency, as expected. The increase in stiffness and decrease in damping have not been measured, since the set-up does not give reliable results for the frequencies at which that effect becomes significant.

7-3 Conclusions and outlook

In this chapter, experimental set-ups, measured results and comparison with models have been discussed.

First, set-up one has been treated in detail. It consists of a single bearing, positioned underneath a target by two micrometer stages and put under a slight angle with a tip-tilt stage. The target is suspended by wires and supported by the bearing. Three eddy current sensors are used to measure film height, tip and tilt. Because of uncertainties in the measured reference position, the measurement procedure consists of alternating tip-tilt minimization by positioning the bearing and remeasuring of a reference zero fly height position.

Even though great care has been taken in making the measurements repeatable, the spread on measured fly heights is significant. Because of the low tip-tilt stiffness, the bearing is repositioned for every change in load capacity. This introduces uncertainty in measured fly heights. The similarity between measurements and model is low. To increase tip-tilt stiffness and reduce this uncertainty, set-up two has been designed and build.

Set-up two consists of three bearings with the same manipulation of $x - y$ position and tip-tilt as set-up one. The bearing surfaces show a non-flat surface profile, likely caused by temperatures changes in the material during manufacturing. The measured surface profile is taken into account in the model. Pneumatically, set-up two is similar to set-up one. Measured conductivities have been included in the model.

The Eddy current sensors have been reused. With a voltage potential between base and target, contact between bearing and target has been measured. For dynamic measurements, the aluminium bottom is replaced with a shaker and base movements are measured with a fourth sensor.

To also measure air flow and the effect of different source pressures, a tank filled with air is deflated through restrictors and thin films while pressure, fly height and contact state are logged. A 2D model has been developed to predict the deflation of a tank through a restrictor and thin film, including measured surface profile and restrictor conductivity.

Measured and modelled results for the deflating tank experiment show excellent agreement. From multiple deflating tank experiments, a load capacity versus fly height curve can be derived. Comparison of these measured curves with modelled results also show excellent agreement, validating the static model.

By exciting the base with a shaker, dynamic response is measured. Resulting transmissibility is compared with modelled results and show agreement up to 500 Hz. Above this frequency, the set-up decouples. Change in stiffness and damping at higher excitation frequencies have not been measured, their effect is not significant for the measurable frequency range.

With the models experimentally verified, the last part of this research is to drawn final conclusions and give recommendations for further research, which is done in the next chapter.

8

Conclusions and recommendations

In this final chapter, conclusions on this research are drawn in the first section. Next, recommendations will be discussed.

8-1 Conclusions

The goal of this research is to design a stable, low stiffness aerostatic thrust bearing system consisting of thrust and vacuum pads. To achieve this goal, both static and dynamic behaviour has been modelled. Bearings have been manufactured and tested to validate the model. In this section, the conclusions that can be drawn from this research will be discussed.

Different modelling approaches have been explored. With both static and dynamic behaviour of interest, the finite volume method model developed in this thesis has proven a fast and reliable approach. It enabled a user interface that in real time updates relevant bearing properties as function of design variables. This interface allows to quickly assess static and dynamic behaviour of a combination of bearings with different geometries, restrictor conductivities and feed pressures.

With the help of this interface, two conceptually different designs for low stiffness air bearings have been conceived. Concept one is based on a height difference between pads, concept two uses a shallow pocket. Both designs are optimized for high range of low stiffness region.

For the purpose of model validation, air bearings have been manufactured. Realisation of a simple bearing with a flat surface fed through a capillary restrictor, as often discussed in literature, has been shown to be not trivial. Important observations on manufacturing of both components have been made.

First, by minimizing downstream volume, restrictors have been integrated such that dynamic instability does not occur. Measurements of restrictor conductance have proven the in literature proposed model to be invalid for realistic pressure drops. The conductance is strongly non-linear, disproving the assumption that it is constant. Without taking the measured restrictor behaviour into account, model and measurement will not match.

Second, assuring flatness of both bearing and running surface has also proven to not be trivial. Controlling surfaces flatness is essential for predictable bearing behaviour. The performance

of available production methods has been thoroughly researched. Best results have been achieved using a lathe, but a check after production remains crucial. Model and measurement correspondence can only be achieved by taking surface properties into account.

Finally, the low tip-tilt stiffness of a single air bearing has been found to negatively effect measurements on film height. By using three bearings, tip-tilt stiffness has been significantly increased. This reduces measurement uncertainty.

By taking these findings into account, excellent agreement between measurements and model has been achieved. Static fly height versus load capacity and air flow are accurately captured. Measured dynamic transmissibility agrees with the model up to 500 Hz. The difficulty in finding agreement between measurement and model shows that manufacturing and testing of air bearings is not as simple as often considered.

With these results, the research goals has been achieved. The lessons learned in this research enable the design, development and testing of a low stiffness prototype. Recommendations concerning this design are shared in the next section.

8-2 Recommendations

Follow up research should be aimed at building and testing a prototype with combined thrust and vacuum bearings with a low stiffness operating point. First, recommendations on modelling will be discussed. Manufacturing will be treated next.

The first part of prototype development should be an update in the restrictor model. Experiments in section 6-2 have shown the proposed model to be insufficient. A more suitable model might be based on Fanno flow [22, chap 9], which described pipe flow with friction for compressible fluids. It is capable of dealing with larger pressure drops than the literature model used in this thesis. Verifying this model with the described restrictor conductivity experiments before using it as a design tool is recommended.

With restrictor non-linearity taken into account, the low stiffness concepts should be optimized. Not too much change is to be expected, since measured restrictor conductivity do not show too much change for higher pressure differences.

Another minor recommendation on modelling is an extra potential speed-up in the dynamic model. The perturbed finite volume method requires a static solution, that so far has been calculated with the static finite volume model. However, this could be replaced with a solution using the analytical model, reducing computational cost which is beneficial for a possible optimization.

Taking lessons learned from chapter 6 and chapter 7 on production of bearing surfaces into account, a tip-tilt stable, axisymmetric design as drawn in Figure 8-1 should be considered. Here, the thrust bearing is located concentrically around the vacuum bearing with an optional ambient pressure part in between. To ensure tip-tilt stability, the pressure feed should consist of three point feeds, as drawn. The advantage of this lay-out is that height steps can be made with a lathe, both in the bearing surface or between surfaces, allowing both developed design concepts to be manufactured.

A second consideration is the method of applying a height offset. Instead of manufacturing offsets, the vacuum and thrust parts could be connected with a flexure. This way, the height

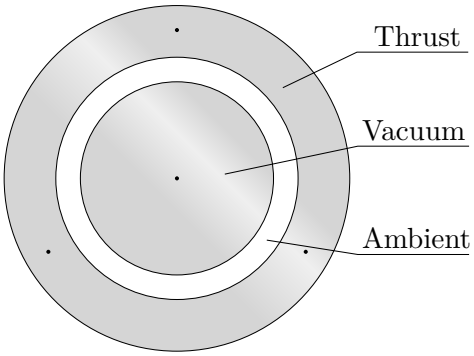

Figure 8-1: Alternative design for combined thrust and vacuum bearing, with optional ambient pressure in between. Because this design is fully axisymmetric, surface finishing is less complicated.

offset and alignment of the pads can be changed after production, allowing multiple offsets to be tested. This would also enable flattening and polishing of both surfaces in the same plane, applying the offset afterwards.

With these recommendations, developing a working low stiffness prototype could be a challenging and rewarding MSc thesis project.

A

Derivation of Reynolds equation

In this appendix the Reynolds equation is derived, in a similar way as can be found in literature.

A-1 Cartesian coordinates

First, the derivation in Cartesian coordinates is discussed. Referenced assumptions can be found in subsection 2-1-1.

A-1-1 Equilibrium of pressure and shear forces on an element

Assume a control volume, as drawn in Figure A-1. Two surfaces at distance h are separated by a thin film. The x and y axis are defined along the bottom surface, the z axis is the normal direction of the surface, in the direction of the film height. In this film, a control volume in equilibrium with sides dx, dy and dz is defined. The film pressure p in z direction is assumed constant, as described in assumption 2. The pressure thus only differs in x and y direction.

For simplicity, only the forces in x direction are drawn in Figure A-1. The derivation will only be worked out in x direction, as the equations in y direction are similar. Because the element is in equilibrium, and flow is laminar (assumption 5) forces must balance. This gives:

$$p\,dy\,dz + \left(\tau_x + \frac{\partial \tau_x}{\partial z}dz\right)dx\,dy = \left(p + \frac{\partial p}{\partial x}dx\right)dy\,dz + \tau_x\,dx\,dz \tag{A-1}$$

where p is the pressure and τ_x the shear stress in x direction. Assuming that $dx\,dy\,dz \neq 0$, meaning that the control volume's volume is not zero, this can be simplified to:

$$\frac{\partial \tau_x}{\partial z} = \frac{\partial p}{\partial x} \tag{A-2}$$

Since the film pressure in z direction is assumed constant, the gradient is zero:

$$\frac{\partial p}{\partial z} = 0 \tag{A-3}$$

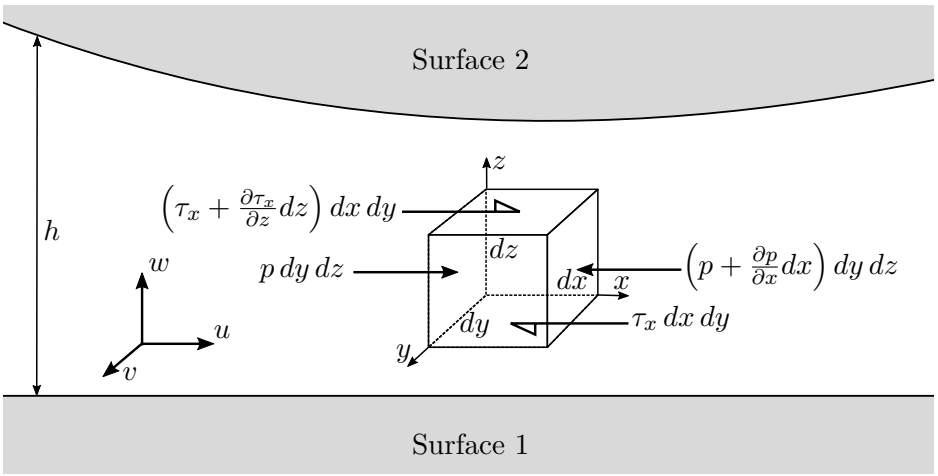

Figure A-1: Equilibrium of forces in x direction of a thin film fluid element in between two surfaces. For clarity, only forces in x direction are showm. p is the film pressure, τ is the shear stress. u, v and w are velocities.

Newton's law of viscous flow relates shear stress to change in velocity, under the assumption that the fluid is Newtonian (assumption 4):

$$\tau_x = \eta \frac{\partial u}{\partial z} \tag{A-4}$$

Substituting (A-4) into (A-2) gives:

$$\frac{\partial p}{\partial x} = \frac{\partial}{\partial z}\left(\eta \frac{\partial u}{\partial z}\right) \tag{A-5}$$

This equation can now be integrated. Assume constant viscosity as in assumption 8, (A-5) becomes:

$$\frac{\partial p}{\partial x} = \eta \frac{\partial^2 u}{\partial z^2} \tag{A-6}$$

Integrating in z:

$$\frac{\partial p}{\partial x} z = \eta \frac{\partial u}{\partial z} + c_1 \tag{A-7}$$

Integrating once more in z:

$$\frac{\partial p}{\partial x} \frac{z^2}{2} = \eta\, u + c_1\, z + c_2 \tag{A-8}$$

The integration constants can be found by assuming there is no slip (assumption 3) between the surface and the fluid. Stating that the velocity at the bottom surface ($z = 0$) is u_1 gives:

$$\eta\, u_1 + c_2 = 0 \quad \rightarrow \quad c_2 = -\eta\, u_1 \tag{A-9}$$

With the velocity at the top ($z = h$) as u_2:

$$\frac{\partial p}{\partial x} \frac{h^2}{2} = \eta\, u_2 + c_1\, h - \eta\, u_1 \quad \rightarrow \quad c_1 = \frac{\partial p}{\partial x} \frac{h}{2} - \frac{\eta}{h}(u_2 - u_1) \tag{A-10}$$

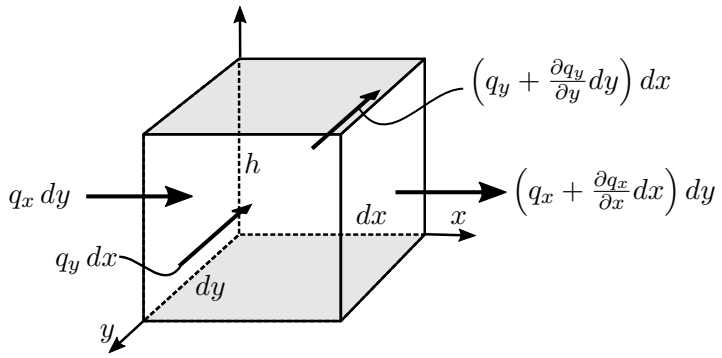

Figure A-2: Continuity of flow in an element with height h enclosed between two surfaces. Flow in and out must equal the change in volume and density.

Substituting (A-9) and (A-10) into (A-8) gives:

$$\frac{\partial p}{\partial x}\frac{z^2}{2} - \frac{\partial p}{\partial x}\frac{h\,z}{2} + \frac{\eta\,z}{h}(u_2 - u_1) + \eta\,u_1 = \eta\,u \tag{A-11}$$

Rewriting, the velocity becomes:

$$u = \left(\frac{z^2 - z\,h}{2\eta}\right)\frac{\partial p}{\partial x} + (u_2 - u_1)\,\frac{z}{h} + u_1 \tag{A-12}$$

The volume flow per unit length is now found by integrating the velocity over the film height:

$$q_x = \int_0^h u(z)\,dz = -\frac{h^3}{12\eta}\frac{\partial p}{\partial x} + \frac{h}{2}(u_1 + u_2) \tag{A-13}$$

In similar fashion, the velocity in y direction can be written as:

$$v = \left(\frac{z^2 - z\,h}{2\eta}\right)\frac{\partial p}{\partial y} + (v_2 - v_1)\,\frac{z}{h} + v_1 \tag{A-14}$$

and the volume flow per unit length in y direction:

$$q_y = \int_0^h v(z)\,dz = -\frac{h^3}{12\eta}\frac{\partial p}{\partial y} + \frac{h}{2}(v_1 + v_2) \tag{A-15}$$

A-1-2 Continuity of flow in an element

Consider the element af shown in Figure A-2. Lubricant flows into the element at rates q_x and q_y and out at $q_x + \frac{\partial q_x}{\partial x}dx$ and $q_y + \frac{\partial q_y}{\partial y}dy$ per unit length and width. The element has a height of h, and the lubricant has density ρ. The mass of lubricant inside the element at any instant is $\rho\,h\,dx\,dy$. Mass conservation demands that the rate of change of the mass inside the element is equal to the difference in inflow and outflow of mass. Therefore:

$$\rho\,q_x\,dy - \left(\rho\,q_x + \frac{\partial\,(\rho\,q_x)}{\partial x}dx\right)dy + \rho\,q_y\,dx - \left(\rho\,q_y + \frac{\partial\,(\rho\,q_y)}{\partial y}dy\right)dx = \frac{\partial}{\partial t}(\rho\,t)\,dx\,dy \tag{A-16}$$

Simplifying this equation gives:

$$-\frac{\partial\left(\rho\, q_x\right)}{\partial x}-\frac{\partial\left(\rho\, q_y\right)}{\partial y}=\frac{\partial}{\partial t}\left(\rho\, t\right) \tag{A-17}$$

However, due to the product rule:

$$\frac{\partial}{\partial t}\left(\rho\, h\right)=\rho\frac{\partial h}{\partial t}+h\frac{\partial \rho}{\partial t} \tag{A-18}$$

By examining Figure A-1, the change in height $\frac{\partial h}{\partial t}$ can be attributed to two factors:

$$\frac{\partial h}{\partial t}=w_2-w_1-u_2\frac{\partial h}{\partial x}-v_2\frac{\partial h}{\partial y} \tag{A-19}$$

The first factor, $w_2 - w_1$, is the direct up and down movement of the surfaces. The second factor is caused by the sideways sideways movement u, v of the surfaces while not parallel, given by $\frac{\partial h}{\partial x}, \frac{\partial h}{\partial y}$. Since for surface 1 in Figure A-1 $\frac{\partial h}{\partial x}=0$ and $\frac{\partial h}{\partial y}=0$, these are omitted from (A-19).

Now plugging (A-13), (A-15) and (A-19) in (A-17) gives:

$$\begin{aligned}\frac{\partial}{\partial x}\left(\frac{\rho\, h^3}{12\,\eta}\frac{\partial p}{\partial x}\right)+\frac{\partial}{\partial y}\left(\frac{\rho\, h^3}{12\,\eta}\frac{\partial p}{\partial y}\right)-\frac{\partial}{\partial x}\left(\frac{\rho\, h\left(u_1+u_2\right)}{2}\right)-\frac{\partial}{\partial y}\left(\frac{\rho\, h\left(v_1+v_2\right)}{2}\right)\\ =\rho\left(w_2-w_1\right)-\rho\, u_2\frac{\partial h}{\partial x}-\rho\, v_2\frac{\partial h}{\partial y}+h\frac{\partial p}{\partial t}\end{aligned} \tag{A-20}$$

This equation is known as the Reynolds equation.

A-2 Polar coordinates

In the previous section, the Reynolds equation is derived in Cartesian coordinate system. However, when modelling circular bearings, a polar coordinate system is more suitable. Therefore, the polar Reynolds equation will be derived in this section in a similar fashion as in section 2-1. Because the steps taken are so similar, this section contains only the most important derivations. Equations in this section are derived from [23].

The assumptions as stated in section 2-1 also apply here. Furthermore, an extra assumptions is added. The system is assumed axisymmetric, meaning there is no flow in the θ direction.

A result of the combination of coordinate system and axisymmetry is that the linear sliding of surfaces cannot be described. A surface velocity in θ means the surfaces are rotating compared to each other. Because of axisymmetry, a radial surface velocity difference would mean that one of the surfaces is expanding out from the origin. Both velocities are not needed in the description of circular thrust bearings, so the Couette flow is left out of this derivation.

In Figure A-3a a fluid element in polar coordinates is drawn. It has sides dr, $d\theta$ and dz. The equivalent figure in Cartesian coordinates is Figure A-1. For a clearer picture of the polar coordinates system, a top view of this element is drawn in Figure A-3b. Here, also the flows are drawn, equivalent to Figure A-2.

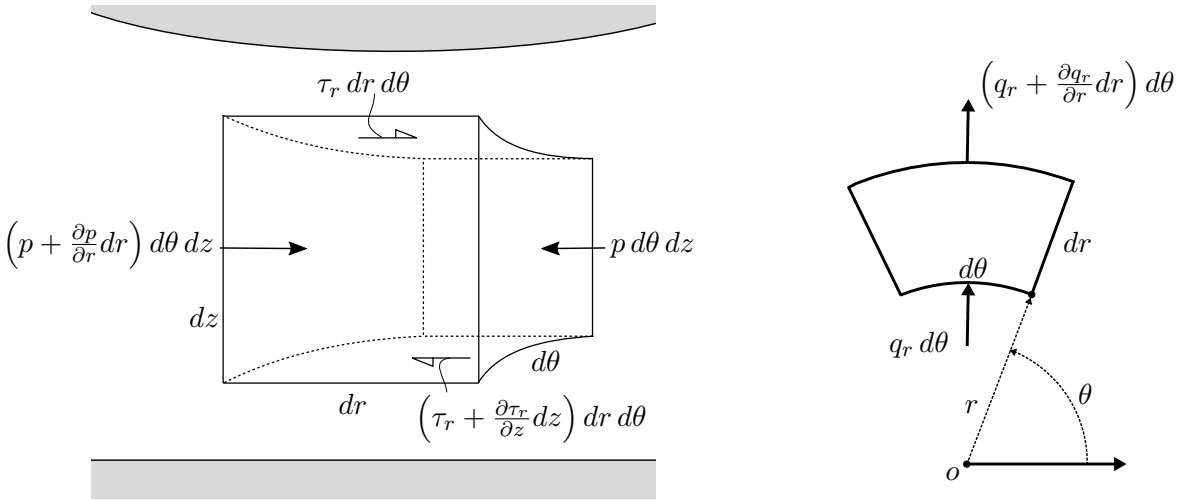

(a) Equilibrium of forces in r direction. Polar coordinate equivalent of Figure A-1.

(b) Top view of fluid element. Out of plane height is h. Polar coordinate equivalent of Figure A-2.

Figure A-3: Thin film fluid element in polar coordinates

Stating the element is in equilibrium, the fluid is Newtonian and the viscosity is constant gives [23, (2.136)]:

$$\frac{\partial p}{\partial r} = \eta \frac{\partial^2 u_r}{\partial z^2} \tag{A-21}$$

Also note that the pressure is constant in the height and axisymmetric:

$$\frac{\partial p}{\partial z} = 0; \quad \frac{\partial p}{\partial \theta} = 0 \tag{A-22}$$

The volume flow per unit length is [23, (2.137)]:

$$q_r = -\frac{h^3}{12\,\eta} \frac{\partial p}{\partial r} \tag{A-23}$$

Continuity, as in Figure A-3b, states:

$$-\frac{1}{r} \frac{\partial}{\partial r} (r\, \rho\, q_r) = \frac{\partial}{\partial t} (\rho\, h) \tag{A-24}$$

Plugging the volume flow per unit length into the continuity equations gives:

$$\frac{1}{r} \frac{\partial}{\partial r} \left(\frac{r\, \rho\, h^3}{12\, \eta} \frac{\partial p}{\partial r} \right) = \frac{\partial}{\partial t} (\rho\, h) \tag{A-25}$$

Converting the density to the pressure with the ideal gas law, as in (2-5), gives the axisymmetric compressible Reynolds equation:

$$\frac{1}{r} \frac{\partial}{\partial r} \left(\frac{r\, p\, h^3}{12\, \eta\, R_s\, T} \frac{\partial p}{\partial r} \right) = \frac{\partial}{\partial t} \left(\frac{p\, h}{R_s\, T} \right) \tag{A-26}$$

B

Finite volume method

This appendix contains all derivations and equations that are needed develop the finite volume method model. Since the perturbed solution requires a static solution, this is developed first.

B-1 Static

In this section, the Reynolds equation, (2-8), is put into dimensionless form and solved using the finite volume method.

Dimensionless numbers

As described in subsection 3-4-3, by defining dimensionless parameters:

$$\begin{aligned} r\ [\mathrm{m}] &= \bar{r}\ [-]\ R\ [\mathrm{m}] \\ p\ [\mathrm{Pa}] &= \bar{p}\ [-]\ P\ [\mathrm{Pa}] \\ h\ [\mathrm{m}] &= \bar{h}\ [-]\ H\ [\mathrm{m}] \end{aligned} \tag{B-1}$$

equation (2-8) can be written as:

$$\frac{H^3\,P^2}{R}\frac{\partial}{\partial \bar{r}}\left(\bar{r}\,\bar{h}^3\,\bar{p}\frac{\partial \bar{p}}{\partial \bar{r}}\right) = 0 \tag{B-2}$$

Discretization

To solve (B-2) for p, the continuous film is now divided into volumes. The volumes have midpoints, numbered i and edges, numbered $i \pm \frac{1}{2}$ as drawn in Figure B-1. Notice that:

$$p\frac{\partial p}{\partial r} = \frac{1}{2}\frac{\partial p^2}{\partial r} \tag{B-3}$$

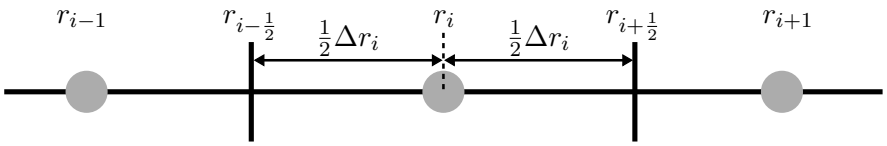

Figure B-1: Definition of 1D mesh for finite volume method

Substitution and integration over volume i gives:

$$\int_{\bar{r}_{i-\frac{1}{2}}}^{\bar{r}_{i+\frac{1}{2}}} \frac{\partial}{\partial \bar{r}} \left(\bar{r}\, \bar{h}^3 \frac{\partial \bar{p}^2}{\partial \bar{r}} \right) d\bar{r} = \bar{r}\, h^3 \frac{\partial \bar{p}^2}{\partial \bar{r}} \bigg|_{\bar{r}_{i+\frac{1}{2}}} - \bar{r}\, h^3 \frac{\partial \bar{p}^2}{\partial \bar{r}} \bigg|_{\bar{r}_{i-\frac{1}{2}}} \tag{B-4}$$

The derivative can be approximated by finite difference:

$$\frac{\partial \bar{p}^2_{i+\frac{1}{2}}}{\partial \bar{r}} \approx \frac{\bar{p}^2_{i+1} - \bar{p}^2_i}{\frac{1}{2}\Delta \bar{r}_{i+1} + \frac{1}{2}\Delta \bar{r}_i} \tag{B-5}$$

Substituting into (B-4) gives:

$$\left(\bar{r}\bar{h}^3\right)_{i+\frac{1}{2}} \frac{\bar{p}^2_{i+1} - \bar{p}^2_i}{\frac{1}{2}\Delta \bar{r}_{i+1} + \frac{1}{2}\Delta \bar{r}_i} - \left(\bar{r}\bar{h}^3\right)_{i-\frac{1}{2}} \frac{\bar{p}^2_i - \bar{p}^2_{i-1}}{\frac{1}{2}\Delta \bar{r}_i + \frac{1}{2}\Delta \bar{r}_{i-1}} = 0 \tag{B-6}$$

This equation describes how $\bar{p}_i$ is dependent on $\bar{p}_{i+1}$ and $\bar{p}_{i-1}$, and thus how the pressure changes through the volumes as function of the neighbouring pressures. To find a solution for the model as drawn in Figure 3-5, in the next section the feed and boundary conditions are added.

Feed

The mass flow of a restrictor with conductivity G_r is given by (3-4). To equate this point source feed to the axisymmetric Reynolds equation, it needs to be divided over an area A. This gives:

$$-\frac{1}{r}\frac{\partial}{\partial r}\left(\frac{r\, h^3}{24\, \eta\, R_s\, T} \frac{\partial p^2}{\partial r} \right) = \frac{\pi\, d^4}{256\, l} \frac{1}{\eta\, R_s\, T} \frac{1}{A} \left(P_s^2 - P_r^2 \right) \tag{B-7}$$

which can be written in a dimensionless form and simplified to:

$$-\frac{\partial}{\partial \bar{r}}\left(\bar{r}\, \bar{h}^3 \frac{\partial \bar{p}^2}{\partial \bar{r}} \right) = \frac{24\, \pi\, d^4}{256\, l} \frac{\bar{r}}{\bar{A}} \frac{1}{H^3} \left(\bar{P}_s^2 - \bar{P}_r^2 \right) \tag{B-8}$$

To discretize this equation, both sides are integrated over the volume at which the source is located. The area over which the point source is spread is changed into the circumference of the mid point of the volume multiplied with the length of the volume: $\bar{A} = 2\, \pi\, \bar{r}_i\, \Delta \bar{r}_i$. The integral of the left side of the equation is already dealt with in (B-4). The right side becomes:

$$\int_{\bar{r}_{i-\frac{1}{2}}}^{\bar{r}_{i+\frac{1}{2}}} \frac{24\, \pi\, d^4}{256\, l} \frac{\bar{r}_i}{2\, \pi\, \bar{r}_i\, \Delta \bar{r}_i} \frac{1}{H^3} \left(\bar{P}_s^2 - \bar{p}_i^2 \right) d\bar{r} = \frac{12\, d^4}{256\, l} \frac{1}{H^3} \left(\bar{P}_s^2 - \bar{p}_i^2 \right) \tag{B-9}$$

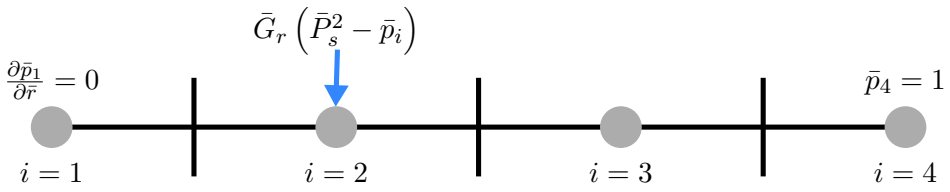

Figure B-2: Example of a meshed thin film domain with 4 volumes, boundary conditions and a feed

since $r_{i+\frac{1}{2}} - r_{i-\frac{1}{2}} = \Delta \bar{r}_i$ and all terms in the equation are constant with $\bar{r}$. Defining the dimensionless conductivity $\bar{G}_r$ as:

$$\bar{G}_r = \frac{12\, d^4}{256\, l} \frac{1}{H^3} \tag{B-10}$$

the following conversion factor is found to compare the dimensionless finite volume method conductivity with the multiple resistance conductivity as described in the previous section:

$$G_r = \frac{\pi\, H^3}{12\, \eta\, R_s\, T} \bar{G}_r \tag{B-11}$$

Boundary conditions

Two boundary conditions are applied to model the air bearing. Firstly, symmetry dictates the pressure at $\bar{r} = 0$ is constant. This gives:

$$\frac{\partial \bar{p}\,(\bar{r} = 0)}{\partial \bar{r}} = 0 \tag{B-12}$$

Secondly, the pressure at the outer radius is equal to the ambient pressure:

$$\bar{p}\,(\bar{r} = 1) = 1 \tag{B-13}$$

Setting up equations

With boundary conditions, air feed and discretization put together, a system of equations can be set up. A small example is used to illustrate this. In Figure B-2, a finite volume grid with 4 volumes is drawn. The feed is connected to the second volume. To simplify equations, a new constant D_i is defined as:

$$D_i = \frac{\bar{r}_{i+\frac{1}{2}} \bar{h}^3_{i+\frac{1}{2}}}{\frac{1}{2}\Delta \bar{r}_{i+1} + \frac{1}{2}\Delta \bar{r}_i} \tag{B-14}$$

By factorizing (B-6) for $\bar{p}_i$ and substituting D_i, the discretized equation for element i is found:

$$D_i\, \bar{p}^2_{i+1} - (D_i + D_{i-1})\, \bar{p}^2_i + D_{i-1} \bar{p}^2_{i-1} = 0 \tag{B-15}$$

Now, setting up the equations for every element in Figure B-2, taking boundary conditions and feed into account, gives:

$$\begin{bmatrix} -D_1 & D_1 & 0 \\ D_1 & -D_2 - D_1 - G_r & D_2 \\ 0 & D_2 & -D_3 - D_2 \end{bmatrix} \begin{bmatrix} \bar{p}_1^2 \\ \bar{p}_2^2 \\ \bar{p}_3^2 \end{bmatrix} = \begin{bmatrix} 0 \\ -\bar{G}_r \, \bar{P}_s^2 \\ -D_3 \end{bmatrix} \tag{B-16}$$

This set of equations can be solved to give the pressures in the thin film.

Load capacity

The load capacity of the bearing can now be determined by integration of the pressures in the volumes. Because the pressure is constant inside the volumes and can only change on the boundaries, the load capacity is the sum over all volumes of the pressure multiplied with the area of that element minus the ambient pressure. Since the dimensionless radius is one, the total ambient pressure on the bearing is $\pi \, 1^2 = \pi$. For a model with N volumes:

$$\bar{W} + \pi = \sum_{1}^{N} \pi \left(\bar{r}_{i+\frac{1}{2}}^2 - \bar{r}_{i-\frac{1}{2}}^2 \right) \bar{p}_i \tag{B-17}$$

As can be seen in (3-12), the pressure drop is a continuous. To better approach this continuous line with constant pressure volumes, more volumes should be used.

The dimensionless load capacity can be converted to a load capacity in Newtons by multiplying the dimensionless variables with their conversion factors:

$$W \text{ [N]} = \bar{W} \text{ [}-\text{]} \; P \text{ [Pa]} \; R^2 \left[\text{m}^2\right] \tag{B-18}$$

B-2 Dynamic

In this section, the perturbed Reynolds equation is written into a dimensionless form and solved using the finite volume method.

Dimensionless equations

By defining one extra dimensionless number:

$$\omega \text{ [1/s]} = \bar{\omega} \text{ [}-\text{]} \; \Omega \text{ [1/s]} = \bar{\omega} \text{ [}-\text{]} \; \frac{P \, H^2}{12 \, \eta \, R^2} \text{ [1/s]} \tag{B-19}$$

the perturbed Reynolds equation, (4-7), can be written as:

$$-\frac{\partial}{\partial \bar{r}} \left(\bar{r} \, \bar{h}_0^3 \, \bar{p}_0 \, \frac{\partial \tilde{\bar{p}}}{\partial \bar{r}} + r \, \bar{h}_0^3 \, \tilde{\bar{p}} \, \frac{\partial \bar{p}_0}{\partial \bar{r}} + 3 \, \bar{h}_0^2 \, \tilde{\bar{h}} \, \bar{p}_0 \frac{\partial \bar{p}_0}{\partial \bar{r}} \right) + \bar{r} \, j \, \bar{\omega} \left(\bar{p}_0 \, \tilde{\bar{h}} + \bar{h}_0 \, \tilde{\bar{p}} \right) = 0 \tag{B-20}$$

Discretization

The definitions of radii used in this section are equal to the definitions used in Figure B-1. Starting by integrating one volume of (4-9), which for convienience is copied in (B-20):

$$\int_{\bar{r}_{i-\frac{1}{2}}}^{\bar{r}_{i+\frac{1}{2}}} \frac{\partial}{\partial \bar{r}} \left(\bar{r}\, \bar{h}_0^3\, \bar{p}_0\, \frac{\partial \tilde{\bar{p}}}{\partial \bar{r}} + \bar{r}\, \bar{h}_0^3\, \tilde{\bar{p}}\, \frac{\partial \bar{p}_0}{\partial \bar{r}} + 3\, \bar{h}_0^2\, \tilde{\bar{h}}\, \bar{p}_0 \frac{\partial \bar{p}_0}{\partial \bar{r}} \right) d\bar{r} = \int_{\bar{r}_{i-\frac{1}{2}}}^{\bar{r}_{i+\frac{1}{2}}} \bar{r}\, j\, \bar{\omega}\, \left(\bar{p}_0\, \tilde{\bar{h}} + \bar{h}_0\, \tilde{\bar{p}} \right) d\bar{r} \quad \text{(B-21)}$$

The partial derivatives of $\bar{p}_0$ and $\tilde{\bar{p}}$ to $\bar{r}$ will be approximated with finite difference. By defining the following constants:

$$k_{i+\frac{1}{2}} = \frac{\bar{r}_{i+\frac{1}{2}}\, \bar{h}^3_{0,i+\frac{1}{2}}}{\frac{1}{2}\Delta r_i + \frac{1}{2}\Delta \bar{r}_{i+1}}, \quad l_{i+\frac{1}{2}} = \frac{3\, \bar{r}_{i+\frac{1}{2}}\, \bar{h}_{0,i+\frac{1}{2}}\, \tilde{\bar{h}}}{\frac{1}{2}\Delta \bar{r}_i + \frac{1}{2}\Delta \bar{r}_{i+1}}, \quad m_i = \bar{\omega} \left(\bar{r}^2_{i+\frac{1}{2}} - \bar{r}^2_{i-\frac{1}{2}} \right) \quad \text{(B-22)}$$

equation (B-21) can be written as:

$$\begin{aligned} &\left[k_{i+\frac{1}{2}}\, \bar{p}_{0,i+\frac{1}{2}}\, (\tilde{\bar{p}}_{i+1} - \tilde{\bar{p}}_i) + k_{i+\frac{1}{2}}\, \tilde{\bar{p}}_{i+\frac{1}{2}}\, (\bar{p}_{0,i+1} - \bar{p}_{0,i}) + l_{i+\frac{1}{2}}\, \bar{p}_{0,i+\frac{1}{2}}\, (\bar{p}_{0,i+1} - \bar{p}_{0,i}) \right] - \\ &\left[k_{i-\frac{1}{2}}\, \bar{p}_{0,i-\frac{1}{2}}\, (\tilde{\bar{p}}_i - \tilde{\bar{p}}_{i-1}) + k_{i-\frac{1}{2}}\, \tilde{\bar{p}}_{i-\frac{1}{2}}\, (\bar{p}_{0,i} - \bar{p}_{0,i-1}) + l_{i-\frac{1}{2}}\, \bar{p}_{0,i-\frac{1}{2}}\, (\bar{p}_{0,i} - \bar{p}_{0,i-1}) \right] = \\ &\qquad \frac{1}{2}\, j\, m_i \left(\bar{p}_{0,i}\, \tilde{\bar{h}}_i + \bar{h}_{0,i}\, \tilde{\bar{p}}_i \right) \end{aligned} \quad \text{(B-23)}$$

The values for $\bar{p}_{0,i+\frac{1}{2}}$ are not defined in the static finite volume model and will be approximated by taking the average of the neighbouring pressures. For $\tilde{\bar{p}}_{i+\frac{1}{2}}$ the same approach is taken:

$$\bar{p}_{0,i+\frac{1}{2}} = \frac{1}{2} \left(\bar{p}_{0,i} + \bar{p}_{0,i+1} \right), \quad \tilde{\bar{p}}_{i+\frac{1}{2}} = \frac{1}{2} \left(\tilde{\bar{p}}_i + \tilde{\bar{p}}_{i+1} \right) \quad \text{(B-24)}$$

Substitution into (B-23) gives:

$$\begin{aligned} &\left[k_{i+\frac{1}{2}}\, (\bar{p}_{0,i} + \bar{p}_{0,i+1})\, (\tilde{\bar{p}}_{i+1} - \tilde{\bar{p}}_i) + k_{i+\frac{1}{2}}\, (\tilde{\bar{p}}_i + \tilde{\bar{p}}_{i+1})\, (\bar{p}_{0,i+1} - \bar{p}_{0,i}) + l_{i+\frac{1}{2}} \left(\bar{p}^2_{0,i+1} - \bar{p}^2_{0,i} \right) \right] - \\ &\left[k_{i-\frac{1}{2}}\, (\bar{p}_{0,i-1} + \bar{p}_{0,i})\, (\tilde{\bar{p}}_i - \tilde{\bar{p}}_{i-1}) + k_{i-\frac{1}{2}}\, (\tilde{\bar{p}}_{i-1} + \tilde{\bar{p}}_i)\, (\bar{p}_{0,i} - \bar{p}_{0,i-1}) + l_{i-\frac{1}{2}} \left(\bar{p}^2_{0,i} - \bar{p}^2_{0,i-1} \right) \right] = \\ &\qquad j\, m_i \left(\bar{p}_{0,i}\, \tilde{\bar{h}}_i + \bar{h}_{0,i}\, \tilde{\bar{p}}_i \right) \end{aligned} \quad \text{(B-25)}$$

This equation is the discretized version of (4-7), using only the pressures at the volume's midpoints. Factorized for $\tilde{p}$ and including feed and boundary conditions, it can be written into a linear system of equations and solved.

Feed

Substituting the perturbed pressure (4-1) into the equation for mass flow through a restrictor (3-4) gives:

$$\dot{m} = G_r \left[Ps^2 - \left(p_0^2 + 2\, p_0\, \tilde{p}\, e^{i\,\omega\, t} + \tilde{p}^2\, e^{2\, i\, \omega\, t} \right) \right] \quad \text{(B-26)}$$

Because $\tilde{p}^2$ can be neglected and $P_s^2 - p_0^2$ is solved in the static equation, the dynamic mass flow is reduced to:

$$\dot{m} = -2\, G_r\, p_0\, \tilde{p}\, e^{i\,\omega\, t} \tag{B-27}$$

Since the feed is divided over an area $\bar{A}$, the mass flow per area can be equated to (4-9):

$$-\frac{\partial}{\partial \bar{r}}\left(\bar{r}\,\bar{h}_0^3\,\bar{p}_0\,\frac{\partial \tilde{\bar{p}}}{\partial \bar{r}} + ...\right) + \frac{12\,\eta\,R^2\,\Omega}{P\,H^2}\,\bar{r}\,j\,\bar{\omega}\left(\bar{p}_0\,\tilde{\bar{h}} + \bar{h}_0\,\tilde{\bar{p}}\right) = -\frac{12\,\eta\,R_s\,T}{H^3}\,\frac{\bar{r}}{\bar{A}}2\,G_r\,\bar{p}_0\,\tilde{p} \tag{B-28}$$

Integrating over the volume with the feed, the feed area becomes $\bar{A} = 2\,\pi\bar{r}_i\,\Delta\bar{r}_i$. The right side of the equation becomes:

$$\int_{\bar{r}_{i-\frac{1}{2}}}^{\bar{r}_{i+\frac{1}{2}}} -\frac{12\,\eta\,R_s\,T}{H^3}\,\frac{\bar{r}_i}{2\,\pi\,\bar{r}_i\,\Delta\bar{r}_i}2\,G_r\,\bar{p}_0\,\tilde{p}\,d\bar{r} = -\bar{G}_r\,\bar{p}_0\,\tilde{p} \tag{B-29}$$

where $\bar{G}_r$ is given by (B-11). Because (B-25) is multiplied with 2 compared to (B-23), this multiplication should also be done for the feed in the finite volume model.

Boundary conditions

The boundary condition are:

$$\frac{\partial \tilde{p}(r=0)}{\partial r} = 0, \quad \tilde{p}(r=r_o) = 0 \tag{B-30}$$

Factorization for pressure

Factorizing (B-25) for $\tilde{\bar{p}}$:

$$D_i\,\tilde{\bar{p}}_{i+1} - (E_i + D_{i-1} + j\,A_i)\,\tilde{\bar{p}}_i + E_{i-1}\,\tilde{\bar{p}}_{i-1} = -C_i + C_{i-1} + j\,B_i \tag{B-31}$$

where:

$$\begin{aligned} A_i = m_i\,\bar{h}_{0,i}, \quad B_i = m_i\,\bar{p}_{0,i}\,\tilde{\bar{h}}, \quad C_i = l_{i+\frac{1}{2}}\left(\bar{p}_{0,i+1}^2 - \bar{p}_{0,i}^2\right), \\ D_i = 2\,k_{i+\frac{1}{2}}\,\bar{p}_{0,i+1}, \quad E_i = 2\,k_{i+\frac{1}{2}}\,\bar{p}_{0,i} \end{aligned} \tag{B-32}$$

Separation of real imaginary parts

The pressure $\tilde{p}_i$ can be split up into its real and imaginary part: $\tilde{p}_i = \tilde{p}_{r,i} + j\,\tilde{p}_{j,i}$. Substituting this into (B-31), the imaginary and a real part can be split up into a linear system of two coupled equations:

$$\begin{aligned} D_i\,\tilde{\bar{p}}_{r,i+1} - (E_i + D_{i-1})\,\tilde{\bar{p}}_{r,i} + A_i\,\tilde{\bar{p}}_{j,i} + E_{i-1}\,\tilde{\bar{p}}_{r,i-1} = -C_i + C_{i-1} \\ D_i\,\tilde{\bar{p}}_{j,i+1} - (E_i + D_{i-1})\,\tilde{\bar{p}}_{j,i} - A_i\,\tilde{\bar{p}}_{r,i} + E_{i-1}\,\tilde{\bar{p}}_{j,i-1} = B_i \end{aligned} \tag{B-33}$$

where in the second equation all terms were multiplied with j.

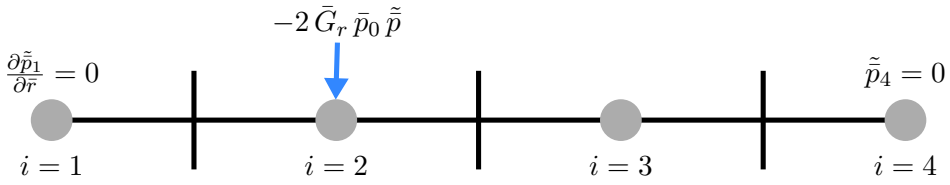

Figure B-3: Example of a meshed thin film domain with 4 volumes, boundary conditions and a feed

System of equations

With the feed, boundary conditions and the discretized equations set up, the example as sketched in Figure B-3 can be solved. Six equations are needed to find the pressures $\tilde{\bar{p}}_{r,1}$ to $\tilde{p}_{r,3}$ and $\tilde{p}_{j,1}$ to $\tilde{p}_{j,3}$:

$$\begin{bmatrix} -E_1 & D_1 & 0 & 0 & 0 & 0 \\ E_1 & -E_2 - D_1 + 2\,\bar{G}_r\,\bar{p}_{0,2} & D_2 & 0 & A_2 & 0 \\ 0 & E_2 & -E_3 - D_2 & 0 & 0 & A_3 \\ 0 & 0 & 0 & -E_1 & D_1 & 0 \\ 0 & -A_2 & 0 & E_1 & -E_2 - D_1 + 2\,\bar{G}_r\,\bar{p}_{0,2} & D_2 \\ 0 & 0 & -A_3 & 0 & E_2 & -E_3 - D_2 \end{bmatrix} \begin{bmatrix} \tilde{\bar{p}}_{r,1} \\ \tilde{\bar{p}}_{r,2} \\ \tilde{\bar{p}}_{r,3} \\ \tilde{\bar{p}}_{j,1} \\ \tilde{\bar{p}}_{j,2} \\ \tilde{\bar{p}}_{j,3} \end{bmatrix} = \begin{bmatrix} -C_1 \\ -C_2 + C_1 \\ -C_3 + C_2 \\ 0 \\ B_2 \\ B_3 \end{bmatrix} \tag{B-34}$$

Stiffness and damping

As described in subsection 4-1-1, the stiffness and damping can be found by integrating the real and imaginary part of $\tilde{\bar{p}}$, which for this finite volume model is equal to summing the pressures multiplied with the area of a volume. The normalised stiffness and damping can be found with:

$$\begin{aligned} \bar{k} &= \sum_{1}^{N} \pi \left(\bar{r}^2_{i+\frac{1}{2}} - \bar{r}^2_{i-\frac{1}{2}} \right) \tilde{\bar{p}}_{r,i} \\ \bar{d} &= \sum_{1}^{N} \pi \left(\bar{r}^2_{i+\frac{1}{2}} - \bar{r}^2_{i-\frac{1}{2}} \right) \frac{\tilde{\bar{p}}_{j,i}}{\Omega} \end{aligned} \tag{B-35}$$

The normalised stiffness and damping can be converted with:

$$\begin{aligned} k\ [\mathrm{N/m}] &= \frac{R^2\,P}{H}\,\bar{k} \\ c\ [\mathrm{N/ms}] &= \frac{R^2\,P\,\Omega}{H}\,\bar{d} \end{aligned} \tag{B-36}$$

C

User interface

With 12 parameters in a study, getting valuable insight in effects and possibilities is not a trivial task. To aid in understanding the effect of combinations of parameters, a graphical user interface is programmed. This interface allows easy experimentation and comparison of different bearing designs. A screen capture is printed in Figure C-1. The functions will be glanced over to give an idea of the functionality.

The top left half of the GUI, panel 1, represents bearing one, the top right half, panel 2, bearing two. The load capacity versus fly height is plotted in the left graph of both halves, the stiffness and damping versus frequency the right halve. Underneath each bearing, the parameters are controlled with sliders and input boxes. The relative height and radius can be set in panel 4, underneath panel 1.

The bottom right half, panel 3, is the combination of bearing 1 and two. Here the result of combining the bearings can be studied. On the bottom right, some plot options are available. Every axes contains two lines, because the plot list has two bearings selected. This allows for easy comparison of designs. The pressure versus radius plots can also be drawn, by selecting this option in the plot type box.

With the help of this user interface, combining vacuum and thrust pads is explored.

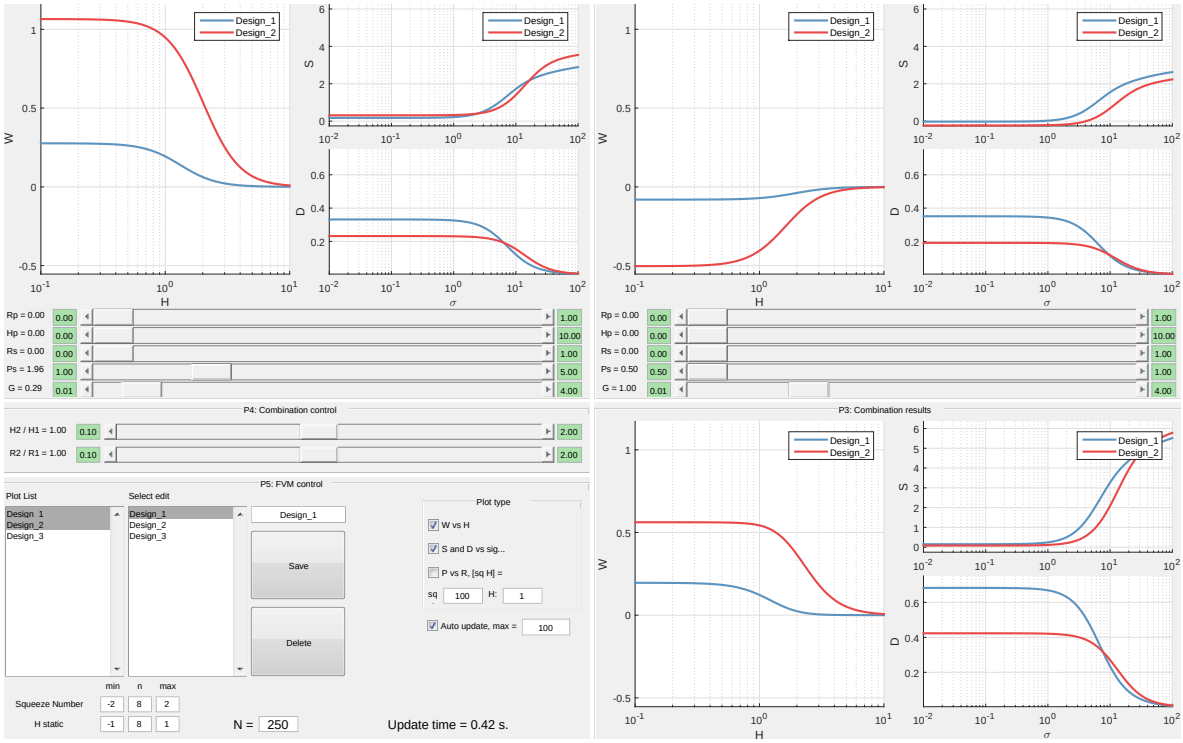

Figure C-1: Screen capture of the graphical user interface.

D

Set-up appendix

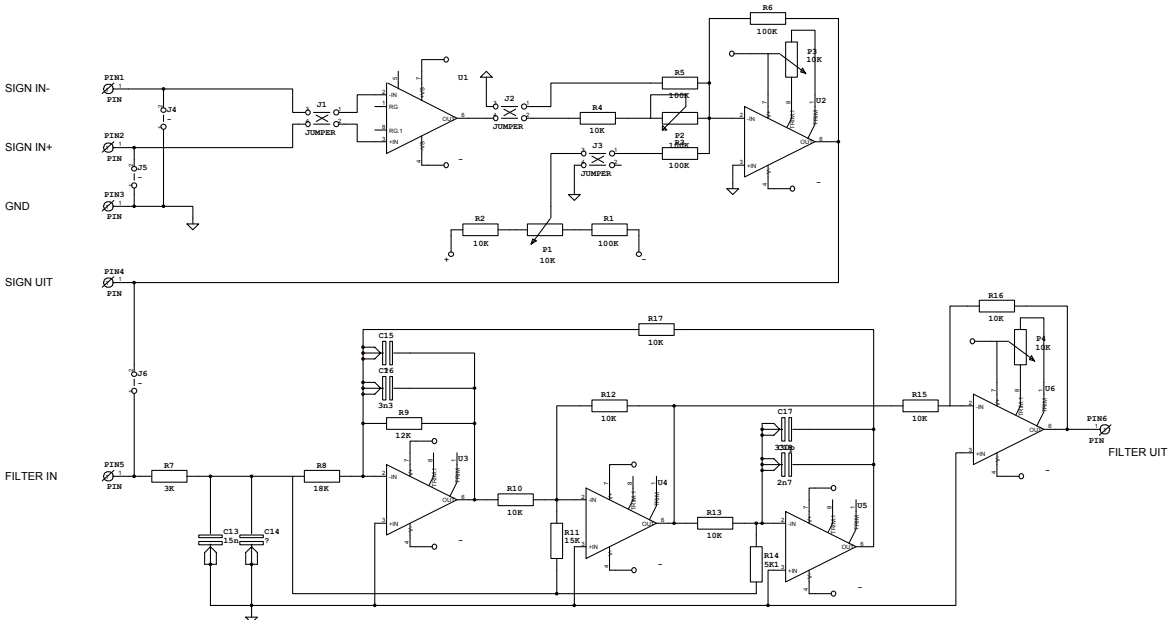

(a) Filter circuit. Courtesy of C.J. Slinkman, TU Delft.

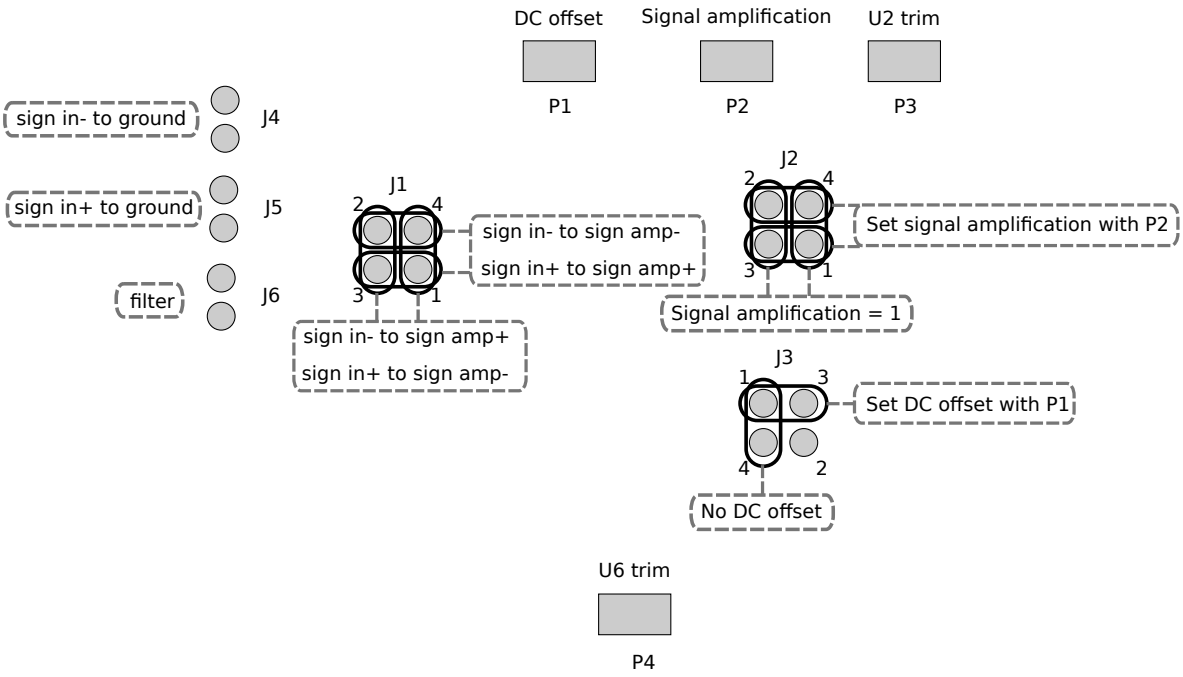

(b) Jumper configuration

Figure D-1: Eddy current sensor low pass filter schematics

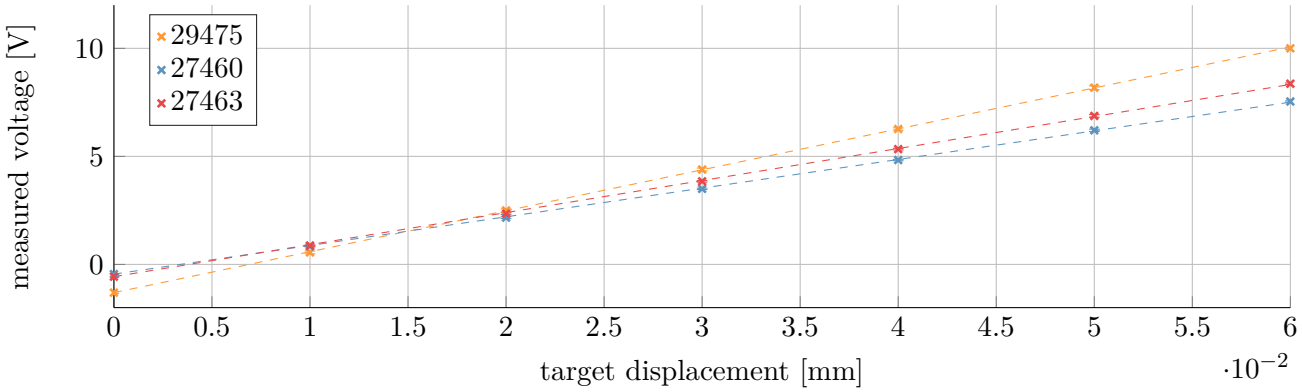

Figure D-2: Calibration result for sensors with serial numbers 29475, 27460 and 27463 on a steel target. Since the signal was amplified 10 times in the filter electronics, maximum output voltage of $10\,\mathrm{V}$ is reached at 10% of the total range of $0.5\,\mathrm{mm}$. Dashed line is the derived sensitivity. 1σ error bars have been plotted on the measured voltages.

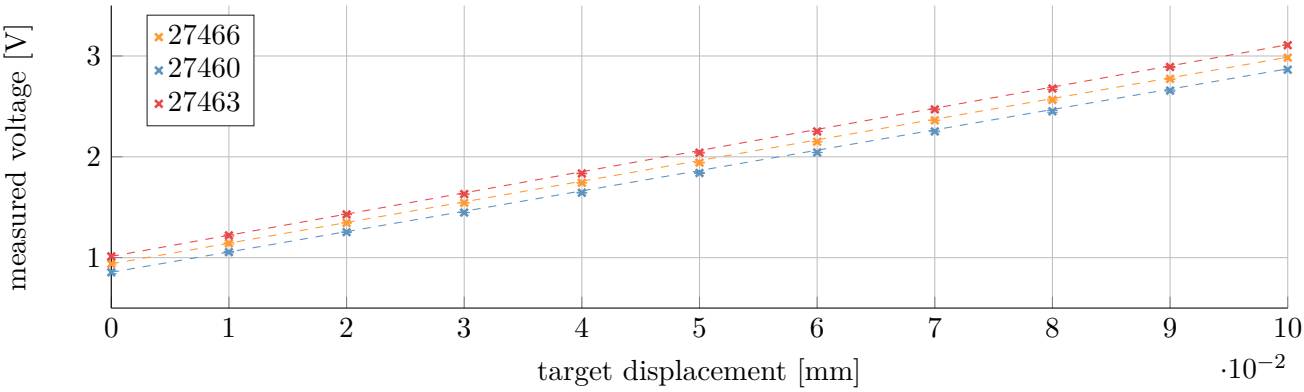

Figure D-3: Calibration result for sensors with serial numbers 27466, 27460 and 27463 on a stainless steel target. Dashed line is the derived sensitivity. 1σ error bars have been plotted on the measured voltages.

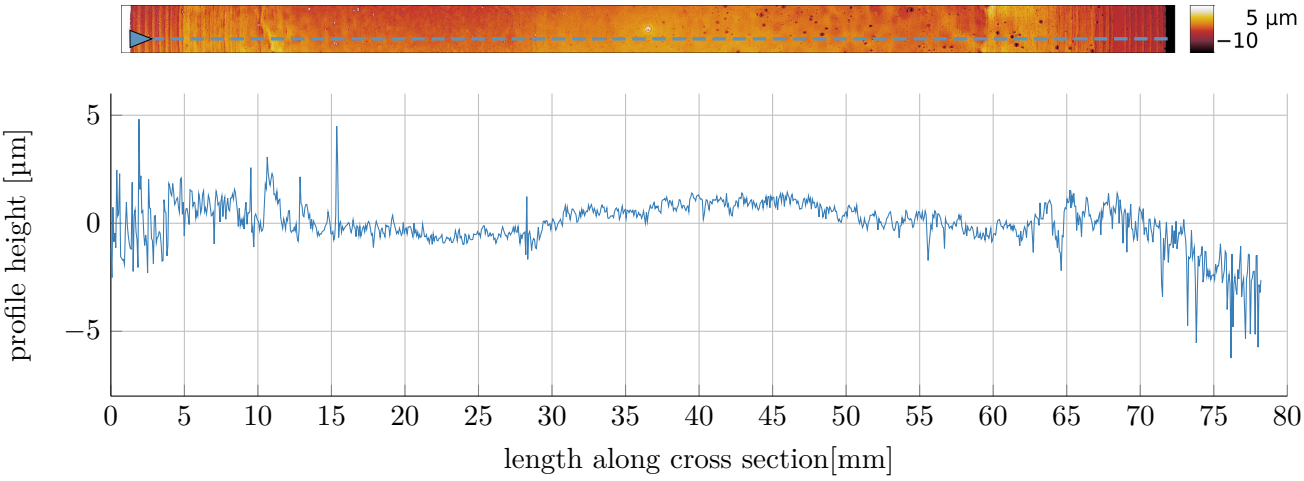

Figure D-4: White light measurement of set-up two target

Bibliography

[1] O. Reynolds, "On the Theory of Lubrication and Its Application to Mr. Beauchamp Tower's Experiments, Including an Experimental Determination of the Viscosity of Olive Oil.," *Proceedings of the Royal Society of London*, vol. 40, no. 242-245, pp. 191–203, 1886.

[2] G. K. Arora, "Floating ring bearing structure and turbocharger employing same," 1981.

[3] J. Bryan, "Design and construction of an ultraprecision 84 inch diamond turning machine," *Precision Engineering*, vol. 1, pp. 13–17, Jan. 1979.

[4] R. Wood, "Future hard disk drive systems," *Journal of Magnetism and Magnetic Materials*, vol. 321, pp. 555–561, Mar. 2009.

[5] A. H. S. David and H. R. George, "High speed dental turbines," 1966.

[6] M. Negishi, A. Deguchi, M. Ando, M. Takimoto, and N. Nakamura, "A high-precision coordinate measuring system for super-smooth polishing," *Nanotechnology*, vol. 6, pp. 139–147, Oct. 1995.

[7] S. Hosoe and T. Yoshida, "Applied measurements of multipurpose precise interferometer (AMOS-1)," *Nanotechnology*, vol. 4, pp. 206–212, Oct. 1993.

[8] H. Onda, "Development of a Unique, High Precision Linear Motor Integrated Air Slide Table, and Its Application to Laser Beam Writers," *Optical Review*, vol. 6, no. 1, pp. 88–92, 1999.

[9] H. Bleuler, R. Clavel, J.-M. Breguet, H. Langen, and E. Pernette, "Issues in precision motion control and microhandling," vol. 1, pp. 959–964, IEEE, 2000.

[10] A. v. Beek and Technische Universiteit Delft, *Advanced Engineering Design: Lifetime Performance and Reliability*. [S.l.]: TU Delft, 2006.

[11] Newway air bearings, "Air bearing application and design guide," Jan. 2006.

[12] R. Snoeys and F. Al-Bender, "Development of improved externally pressurized gas bearings," *KSME Journal*, vol. 1, no. 1, pp. 81–88, 1987.

[13] M.-F. Chen and Y.-T. Lin, "Dynamic Analysis of the X-shaped Groove Aerostatic Bearings with Disk-Spring Compensator.," *JSME International Journal Series C*, vol. 45, no. 2, pp. 492–501, 2002.

[14] M. R. Bryant, S. A. Velinsky, N. H. Beachley, and F. J. Fronczak, "A Design Methodology for Obtaining Infinite Stiffness in an Aerostatic Thrust Bearing," *Journal of Mechanisms Transmissions and Automation in Design*, vol. 108, no. 4, p. 448, 1986.

[15] G. Aguirre, F. Al-Bender, and H. Van Brussel, "A multiphysics coupled model for active aerostatic thrust bearings," pp. 710–715, IEEE, July 2008.

[16] H. Mizumoto and T. Shimizu, "An Infinite-Stiffness Aerostatic Spindle with Active Restrictors," *JOURNAL-JAPAN SOCIETY FOR PRECISION ENGINEERING*, vol. 59, pp. 607–607, 1993.

[17] H. Mizumoto, S. Arii, Y. Kami, K. Goto, T. Yamamoto, and M. Kawamoto, "Active inherent restrictor for air-bearing spindles," *Precision Engineering*, vol. 19, pp. 141–147, Oct. 1996.

[18] S. Morosi and I. F. Santos, "Active lubrication applied to radial gas journal bearings. Part 1: Modeling," *Tribology International*, vol. 44, pp. 1949–1958, Nov. 2011.

[19] E. I. Rivin, "Vibration isolation of precision equipment," *Precision Engineering*, vol. 17, pp. 41–56, Jan. 1995.

[20] G. W. Stachowiak and A. W. Batchelor, *Engineering tribology*. No. 24 in Tribology series, Amsterdam ; New York: Elsevier, 1993.

[21] B. J. Hamrock, *Fundamentals of Fluid Film Lubrication*. No. 1255 in NASA Reference Publication, NASA, 1991.

[22] F. M. White, *Fluid mechanics*. McGraw-Hill series in mechanical engineering, Boston: McGraw-Hill, 6. ed., international ed ed., 2008.

[23] V. N. Constantinescu and R. L. Wehe, *Gas lubrication*. 1969.

[24] F. Al-Bender, *Contributions to the design theory of circular centrally fed aerostatic bearings*. PhD thesis, Katholieke Universiteit Leuven, Faculteit der Toegepaste Wetenschappen, Departement Werktuigkunde Afdeling Produktietechnieken, Machinebouw en Automatisering, Leuven (Heverlee), Belgium, 1992.

[25] R. M. Schmidt, G. Schitter, and J. v. Eijk, *The design of high performance mechatronics: high-tech functionality by multidisciplinary system integration*. Amsterdam: Delft University Press, 2011.

[26] J. S. Jacob, John J. Yu, Donald E. Bently, and Paul Goldman, "Air-Hammer Instability of Externally Pressurized Compressible- Fluid Bearings," *Proc. ISCORMA*, Aug. 2001.

[27] Y. Mitsuya and S. Fukui, "Stokes Roughness Effects on Hydrodynamic Lubrication. Part 1 - Comparison Between Incompressible and Compressible Lubricating Films," *Journal of Tribology*, vol. 108, no. 2, p. 151, 1986.

[28] "Kemet - Precision Lapping Machines, Polishing Machines." http://www.kemet.co.uk/products/flatlapping. Accessed: 2016-03-31.

[29] "LapMaster - Lapping Polishing Machinery." http://www.lapmaster.com/lapping-polishing-machinery.html. Accessed: 2016-03-31.

[30] L. Licht and H. Elrod, "A Study of the Stability of Externally Pressurized Gas Bearings," *Journal of Applied Mechanics*, vol. 27, no. 2, p. 250, 1960.

[31] MICRO-EPSILON MESSTECHNIK, "eddyNCDT3010 Instruction Manual."

[32] P. Holster, J. Jacobs, and J. Roblee, "The Measurement and Finite Element Analysis of the Dynamic Stiffness of Nonuniform Clearance, Gas, Thrust Bearings," *Journal of Tribology*, vol. 113, no. 4, p. 768, 1991.